MICROSTRUCTURAL AND GEOMETRIC EFFECTS ON THE PIEZOELECTRIC PERFORMANCE OF PZT MEMS

BY

MICHELLE CHRISTINA ROBINSON

A dissertation submitted in partial fulfillment of

the requirements for the degree of

DOCTOR OF PHILOSOPHY OF MATERIAL SCIENCE

WASHINGTON STATE UNIVERSITY

Department of Materials and Mechanical Engineering

DECEMBER 2007

To the Faculty of Washington State University:

The members of the Committee appointed to examine the dissertation of MICHELLE CHRISTINA ROBINSON find it satisfactory and recommend that it be accepted.

_____

Chair

_____

_____

_____

ACKNOWLEDGMENTS

First, I would like to thank my husband Dirk for all of his support and encouragement through all of the ups and downs during the years it took to achieve this goal. To my advisor, Dr. Bahr, thank you for all of the discussions and guidance throughout my time in the Material Science department; your motivational and respectful attitude allowed me to learn and grow in countless ways. To my committee members: Dr. R. Richards, Dr. C. Richards, and Dr. Field thank you so much for your encouragement and helpful hints throughout this research. Your abilities to instill confidence forced me to face challenges that I could not have overcome before joining this department. Finally, to all of my friends and family that have been there when the days and weeks got long, thank you for holding my up with your blessings and love.

MICROSTRUCTURAL AND GEOMETRIC EFFECTS ON THE PIEZOELECTRIC PERFORMANCE OF PZT MEMS

Abstract

by Michelle Christina Robinson, Ph.D.

Washington State University

December 2007

Chair: David F. Bahr

The performance of a piezoelectric membrane in MEMS was evaluated for use in power generation. An investigation was conducted to examine geometric and material properties that influence the ability to strain a piezoelectric membrane. The amount of strain and electrical energy produced by mechanically actuating the membrane revealed insight to improve the amount of power produced by the piezoelectric element within the membrane. The amount of deflection was the key influence to create biaxial strains of up to approximately 0.2%, above which membrane fracture tends to occur. This level of strain was found to limit the coupling coefficient to 3% and the amount of RMS power produced during dynamic operation to approximately 20 μW in an 8 mm membrane. In order to achieve desired amounts of power for PZT MEMS device applications, the operating conditions, piezoelectric membrane properties, and membrane geometry can be tailored. Each of these aspects are included in the developed predictive expressions for output power and the coupling coefficient, which are verified with experiment and discussed in this dissertation.

TABLE OF CONTENTS

Page

LIST OF TABLES

LIST OF FIGURES

CHAPTER ONE

INTRODUCTION

The intent of this research was to design a piezoelectric membrane for power generation applications on the micro scale through examining the geometric and material properties that influence its performance. During the design process, one of the goals was to establish a membrane that demonstrates superior electromechanical performance. Since the performance is driven by the specifications of the application, including for example microscale power generation or sensor applications, care was taken to change one aspect at a time. Many of the performance characteristics are dependent on a variety of material and geometric properties. Thus, this dissertation is broken up into chapters that focus on the geometry of the membrane, the materials within the membrane, and the performance of the membrane.

The piezoelectric material lead-zirconate-titanate (PZT) is a realizable type of piezoelectric because of its relative ease of deposition, high piezoelectric and electromechanical coupling coefficients, and the ability for its composition to be tailored. The study of piezoelectric materials for micro-scale electromechanical devices has increasingly become important in the attempt to move towards maximizing power generation for micro-scale devices. These devices need to be portable to allow for mobility and versatility in communication. With the ability to create small portable devices, the ability to manufacture smaller battery and energy storage methods becomes increasingly necessary. However, these goals have not yet been attained. It is often the case that batteries must be large in order to provide the power requirements of a small

portable device. One alternative to large battery sources is to create energy through harvesting the energy produced by a bending or stretching piezoelectric material.

Power harvesting with piezoelectric materials has been studied in various ways. Researchers have implanted a polyvinylidene fluoride (PVDF) patch onto the rib cage of a dog to harvest energy as the dog breathes [1]. There have also been attempts to utilize parasitic power harvesting in shoes [2]. Many such experiments were successful in harvesting several microwatts to milliwatts of usable power. None of these systems, however, satisfied the criteria of being lightweight, capable of high power generation and efficient in power delivery on a MEMS scale. The research described in this dissertation includes the development of analytical expressions that enable the performance of piezoelectric membranes to be predicted in terms of their micropower production capabilities. PZT was chosen for the P^3 microengine because of the ability to tailor its properties to meet a variety of electromechanical performance criteria [3]. Since power generation and efficiency are key criteria for the performance of this micro-scale device, predictability in how the piezoelectric material can be tailored is essential. The effects of geometry and the materials that compose the membrane were examined and are presented as they pertain to the membrane performance.

Specific aspects of the geometry that influence the membrane performance include the composite structure, the design of the electrodes that sandwich the piezoelectric film, and the boundary conditions. Each of the layers that create the composite membrane have material properties that must work in concert as the membrane bends and stretches. The Young's modulus, Poisson's ratio, and the stress of each layer have been integrated into the analytical expressions so that the overall structural integrity

and membrane performance involves a thickness weighted influence by the individual materials within the composite. One chapter of this dissertation is devoted to how the geometry of the composite membrane was carefully changed, in order to improve the overall performance of the membrane, by utilizing the analytical expressions.

The specific materials that are used in the membrane structure were investigated because the structure of the membrane must remain intact during operation and perform well under many different operational modes. One chapter describes in detail how the bottom electrode material was changed from platinum to gold, in order to show that overall the PZT microstructure and the material properties of the PZT remained consistent. This established that different bottom electrode materials can demonstrate good membrane performance. In addition, the analytical expressions allow for each material in the composite to change, in order to establish if the performance of the membrane will improve.

The performance of the fabricated composite membrane is the true test of how the membrane was designed. This dissertation includes a description of how the membrane performs in terms of its electromechanical coupling, micropower output, and its strain at failure. Many different characterization tools were utilized to establish the performance level of the membranes including both operational and microscopy tools. The operational tools were used to establish both static and dynamic characteristics of the membrane. Microscopy tools were utilized to examine the microstructural integrity and properties of the membranes before and after operation.

References

[1] E. Hausler, L. Stein, "*Implantable Physiological Power Supply with PVDF Film*," Ferroelectronics **60** (1984) p. 277-282.

[2] J. Kymissis, C. Kendall, J. Paradiso, N. Gershenfeld, *"Parasitic Power Harvesting in Shoes,"* Proceedings: Second IEEE International Conference on Wearable Computing, (1998) p. 132-139.

[3] S. Whalen, M. Thompson, D.F. Bahr, C.D. Richards, R.F. Richards, "*Design, fabrication and testing of the P^3 micro heat engine*," Sensors and Actuators A **104** (2003) p. 290-298.

CHAPTER TWO

LITERATURE REVIEW

Piezoelectric materials have been researched for utilization in vibration based applications including micro power generation devices and sensors for several years. Initially, AlN and ZnO films were used to create microelectromechanical systems (MEMS) [1, 2]. Standard silicon processing was capable of incorporating these films because they are relatively easy to deposit. However, it was found that a lead-zirconate-titanate (PZT) film performed better than these films by producing 100 times the acoustic power density and the PZT film was able to withstand larger forces [3]. Therefore, incorporating PZT films for use in MEMS devices became an important aspect of MEMS research. The difficulty with incorporating PZT was the high annealing temperature required to crystallize a sol-gel deposited PZT film, which induced cracking and a general breakdown in the uniformity of the film microstructure. Once the fabrication issues were resolved, it was found that the PZT-based films provided higher deflections, which directly decreased the driving voltage necessary to achieve improved performance for a thin film micromotor [4, 5].

Once it was established that PZT was a viable piezoelectric option for thin film applications, understanding the film properties and how they influence device performance was the next direction of investigation in the process of incorporating PZT into MEMS. In this dissertation, the focus is on microstructure and geometric changes that influence the piezoelectric performance of PZT MEMS. Therefore, the following discussion will include a summary of results found in literature that utilized either

microstructure or geometric changes in order to improve the performance of piezoelectric MEMS devices.

Microstructure changes that have been shown to improve piezoelectric device performance using PZT-based films include increasing the porosity of the film, increasing the percent composition of oxygen and argon during processing, increasing the modulus, and doping the PZT with Niobium or Tin. Each of these methods of improving the performance was experimentally verified.

As deposited PZT films have randomly oriented dipoles. Despite the random orientation, the film produces a small amount of charge when it is strained. MEMS devices typically require larger amounts of charge than is produced by as deposited PZT films. Several research groups have investigated different approaches to improve the amount of output charge produced by the PZT film [6, 7, 8]. Initially, the approach was to apply a field of 30 MV/m for only 2 s in the direction of the piezoelectric film thickness. However, this was not as effective as applying a smaller ac field of approximately 0.5 to 2 V, in addition to a dc bias of 2 V, parallel to the polarization of the film during operation, which provided an increase in the piezoelectric coefficient d_{33} [7]. The amount of output charge is instrumental to the electromechanical performance of the piezoelectric thin film. In research conducted by Kholkin *et al.* an interferometer was utilized to measure small field induced displacements with a variation in the poling time of 900, 300, and 60 seconds with a field of 230 kV/cm. The piezoelectric property d_{33} was measured after time passed and in each case it was found that this value decreased, as shown in figure 2.1. Projecting the decrease over two years provides a total decrease

of 25% from the initial value [9]. A d_{33} value of 40 pm/V was reported for the 2 mm diameter diaphragm [4].

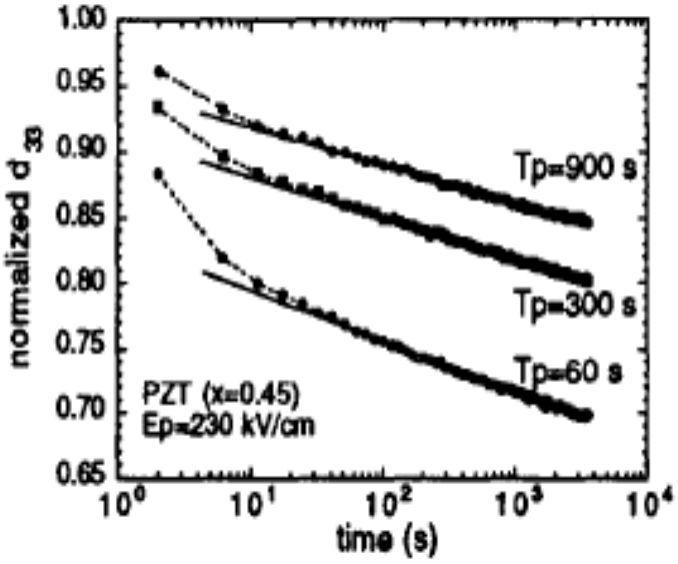

Figure 2.1: Kholkin *et al*. show how d_{33} is affected by poling time for three poling conditions [9].

Increasing the piezoelectric coefficients, d_{33} and e_{31}, will directly improve the performance of piezoelectric MEMS devices. In a report by Xu *et al.* it was estimated that 25% to 50% of the dielectric response in PZT-based piezoelectric films is due to 180 degree wall motion, which increased with both film thickness and grain size [10]. The PZT films used in this study ranged in thickness from 0.5 to 6.7 µm and were poled with an ac field of 250 kV/cm, in addition to a field of 2 kV/cm during operation. Substrates of Pt(111)/Ti/SiO_2/Si and Pt(100)/SiO_2/Si were both used in this research. Although the films had different thicknesses, grain sizes, and a preferred orientation, similar dielectric constants were found. The effective e_{31} and d_{33} properties both increase with increasing

film thickness for the piezoelectric materials PZT, ZnO, and AlN with a substrate consisting of Pt/Ti/SiO_2/Si. Figure 2.2 shows that as the PZT thickness increases, d_{33} increases.

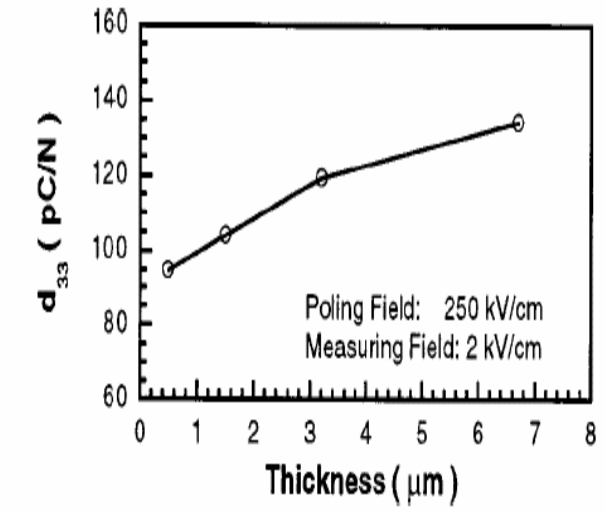

Figure 2.2: As the PZT thickness increases, d_{33} increases [10].

Their reasoning for this suggests that as the film becomes thicker there is a combination of increased porosity leading to a reduced clamping effect and interfacial phenomena such as built in fields, stain gradients, and compositional variation. These results have been experimentally verified and presented by Muralt *et al.* [3].

Changing the PZT composition is another method to changing the microstructure of the PZT. This has been shown for other piezoelectric materials. Vergara *et al*. utilized doping with oxygen and argon impurities in the crystal structure of the piezoelectric film AlN during growth [11].

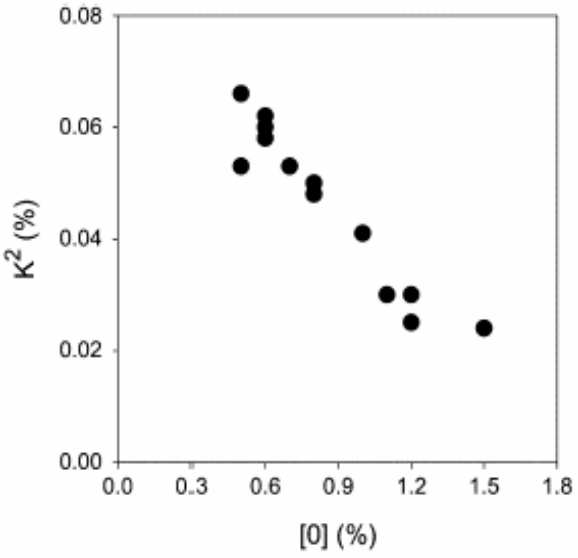

Figure 2.3: Vergara *et al.* show that the percent composition of oxygen in the AlN film affects the coupling coefficient [11].

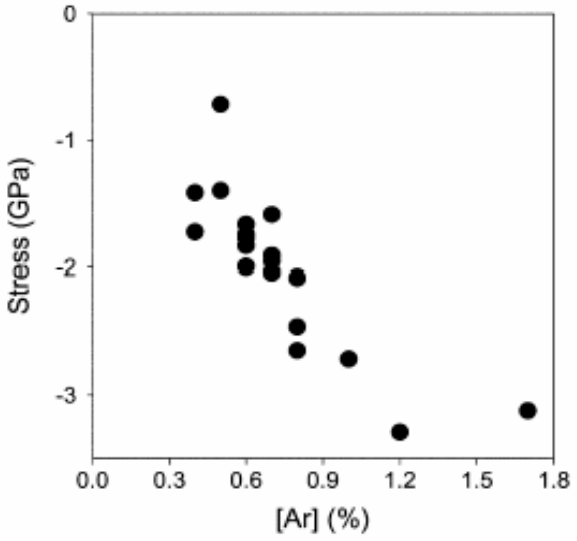

Figure 2.4: Vergara *et al.* show that the percent composition of Ar present in the AlN film directly affects the stress [11].

It was found for AlN films, which were intended for surface acoustic applications, that the coupling coefficient is dependent on the percent of oxygen impurity, as shown in figure 2.3, and that the residual stress decreases with percent argon impurity, as shown in figure 2.4. Figures 2.3 and 2.4 directly reveal that the performance is improved by limiting the oxygen percent present and increasing the argon percent present during processing. The coupling coefficient is a performance property of piezoelectric MEMS devices that should be optimized, in order to achieve high performance. The amount residual stress in a PZT film is typically detrimental to a MEMS device because it inhibits the performance.

Muralt *et al*. suggests several methods for improving the electromechanical behavior of piezoelectric membranes [12]. The method that is related to changing the microstructure of the PZT film is to dope the PZT with Niobium or Tin. This change would effectively change the structure of the film in such a way to reduce the residual stress and thereby improve the overall performance of the device. Recent research conducted by Martinez provides insight into how doping the PZT film with Nb affects the piezoelectric coefficients and the residual stress [13]. It was found that for a PZT film with a composition that is near the morphotropic phase boundary and doped with 1-2% Nb, the piezoelectric coefficient e_{31} increases by over 50% compared to tetragonal PZT films doped with the same Zr:Ti ratio. The piezoelectric coefficient d_{31} did not change by doping the PZT film with Nb. It was also determined that for both the tetragonal and rhombohedral films, a decrease in the residual stress was seen with Nb additions of 2.8 mol%. Therefore, changing the composition of the PZT film by doping it with Nb

provides an increase in e_{31} and a decrease in the residual stress, which both contribute to improved piezoelectric MEMS performance.

In contrast and addition to microstructure changes, geometric changes can also provide an improvement in piezoelectric MEMS device performance. Several research groups have focused on this avenue for improving the PZT-based piezoelectric film for different types of applications. A few of the types of geometric changes that have been investigated include examining the effect of substrate and PZT film thickness, altering the shape and boundary conditions of the membranes, trenching around the membrane, adding material layers that have a compressive stress, and altering the electrode coverage in several different patterns. Each of these geometric changes improves the PZT film performance to varying degrees.

For vibration based devices several research groups examined how geometric changes to a composite membrane structure affect the resonant frequency. Muralt *et al.* experimentally varied the substrate thickness from zero to 30 μm with an electrode covering half of the diaphragm [14]. Figure 2.5 shows that for a PZT thickness of 0.6 μm, the resonant frequency increases as the silicon thickness increases. The difference in the curves shown in figure 2.5 is that the resonant frequency significantly shifts to the upper curve when a dc bias field of 2 kV/cm is applied. The increase in resonant frequency as the membrane thickness increases was also found by Trolier-McKinstry *et al.*, in order to create optimal performance from an accelerometer [15]. Figure 2.6 shows experimentally measured data and a bending stiffness model that is based on predicted resonant frequencies plotted against varying membrane thickness.

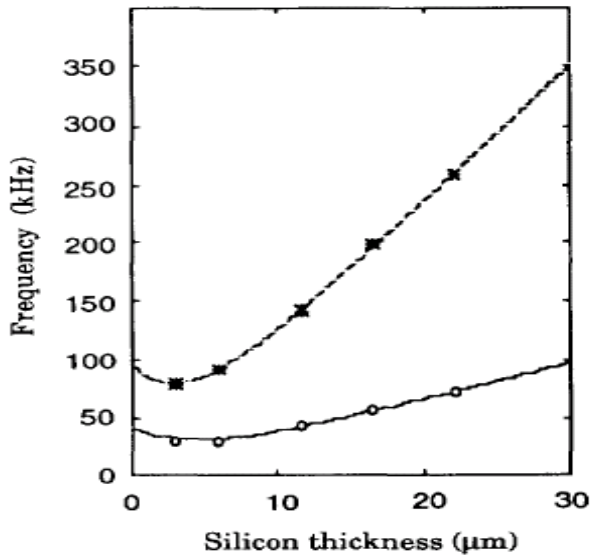

Figure 2.5: Muralt *et al.* examined the relationship between the support layer of silicon thickness and the resonant frequency of a 2 mm diameter circular PZT diaphragm [7].

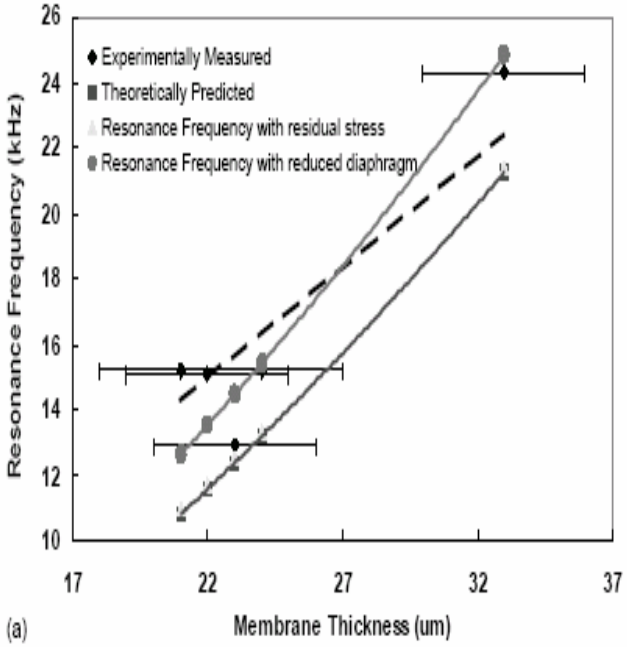

Figure 2.6: Trolier-McKinstry *et al*. show that as the membrane thickness increases, the trends found by their experiments agree with theory [15].

Muralt *et al*. also provides a report that shows the relationship between the coupling coefficient, resonant frequency, and silicon thickness for three PZT thicknesses, which is based on a simulation that does not incorporate stresses [16]. Figure 2.7 shows that as the silicon thickness increases the resonant frequency increases and the coupling coefficient decreases. Therefore, depending on the type of application, a thin silicon substrate will provide the best overall coupling coefficient, which is a key factor that is examined for defining piezoelectric membrane performance. However, there is a trade off, if there is a specific resonant frequency required that exceeds the lower range shown in figure 2.7.

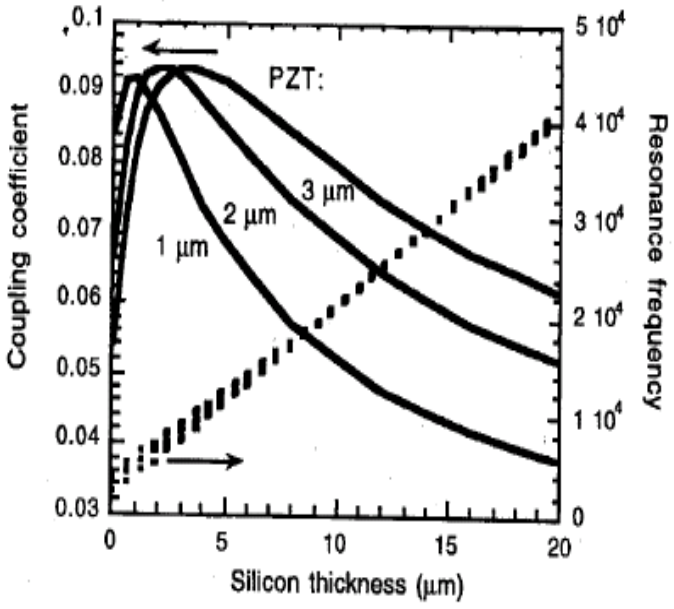

Figure 2.7: Muralt *et al.* simulated how the coupling coefficient and the resonant frequency change as the silicon thickness changes [16].

In comparison with this modeling result, Al-Hattamleh showed with finite element modeling, which incorporated residual stress, that for silicon thicknesses between 1 to 3 μm, the coupling coefficient will be at a maximum [17]. The highest coupling coefficient is provided when the neutral axis is located within the bottom electrode, which occurs when the Si/PZT thickness ratio approaches 4. In addition, this finite element modeling determined that when the Si thickness decreases, the coupling coefficient increases.

Ma *et al*. utilized a finite element method to determine how geometric changes in boundary conditions affect the resonant frequency compared to experiment [18]. Experiments were performed that changed the boundary conditions from clamped to simply supported. The resonant frequency of 1.0 kHz for a clamped boundary condition was found to decrease to 0.5 kHz when the boundary condition was changed to simply supported. This agrees with the finite element predictions and can also be seen with a simple spring mass system because as the stiffness of the system decreases with less clamping, the resonant frequency decreases as well. Similarly, Irie *et al.* utilized the Ritz method to examine the effect of changing boundary conditions on the resonant frequency. In addition to square membranes, this research investigated circular and square plates with rounded corner geometries [19]. In the simply supported case the circular geometry consistently had a higher resonant frequency than the other geometries and the square with rounded corner geometry had a higher resonant frequency than the square geometry. A similar trend was found for the clamped boundary condition. In direct correlation to results presented by Ma *et al*., Irie *et al*. found that the clamped boundary condition revealed a higher resonant frequency in each geometrical case when compared with the simply supported results. Optimizing the performance of the membranes with these types

of geometry is dependent on the application. However, understanding how each effects the resonant frequency is an important step in establishing good performance.

The residual stress in a composite membrane is clearly influenced by geometric changes in the membrane structure. The coupling coefficient is a key property often used to describe the performance of a piezoelectric system. It is defined as the electrical energy converted divided by the mechanical energy used to deform the structure. Analytical modeling has been conducted by Cho *et al.* to determine the relation between the coupling coefficient and the residual stress for a membrane [20]. Figure 2.8 shows that for a membrane with high residual stress the coupling coefficient is low and in order to increase this property, the residual stress should be reduced. This model is based on first principles of oscillatory motion and energy conversion and thus provides critical direction for further research.

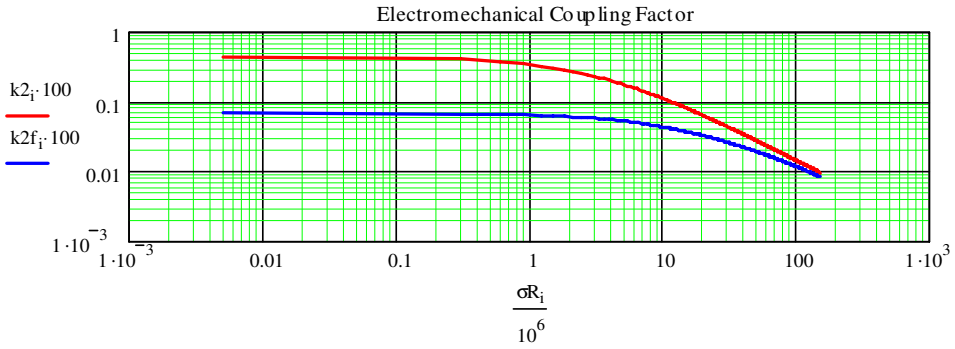

Figure 2.8: Model of electromechanical coupling conversion compared with residual stress for simply supported (top curve) and clamped (bottom curve) boundary conditions [20].

Since the residual stress is a significant factor that inhibits the performance of piezoelectric membrane systems, extensive research has been conducted to determine how to reduce the amount of residual stress that accumulates during processing. Muralt *et al*. suggests two geometric changes for reducing the residual stress, in order to improve the electromechanical performance of piezoelectric membranes [12]. One method is to add a compressive SiO_2 layer to the structure that serves to compliment the tensile stresses that build as the PZT is deposited and crystallized. A second method of reducing the residual stress in the structure is to create trenches around the membrane so that the blanket layers of material are essentially patterned. This enables the membrane to be more compliant because some of the stresses at the edges of the membrane are released. The affect on performance by each of these particular geometric changes is discussed in Chapter 4.

Adding material layers, in order to reduce the amount of residual stress, has been investigated by a few research groups. Johnson *et al.* reduced the residual stress by adding an additional layer of material [21]. Thermal barrier coatings of yttria-stablized zirconia with thicknesses of between 125 and 250 μm were added to a substrate of Ni-based superalloy plates, in order to increase the elastic modulus and therein change the residual stress, as shown in figure 2.9. Reducing the residual stress, in order to increase the performance of a composite piezoelectric membrane was also shown by Kennedy *et al.,* by adding a compressive W layer to the structure [22]. It was found that the additional W layer resulted in a reduced residual stress, which increased the compliance by 7% and reduced the resonant frequency by 5 kHz.

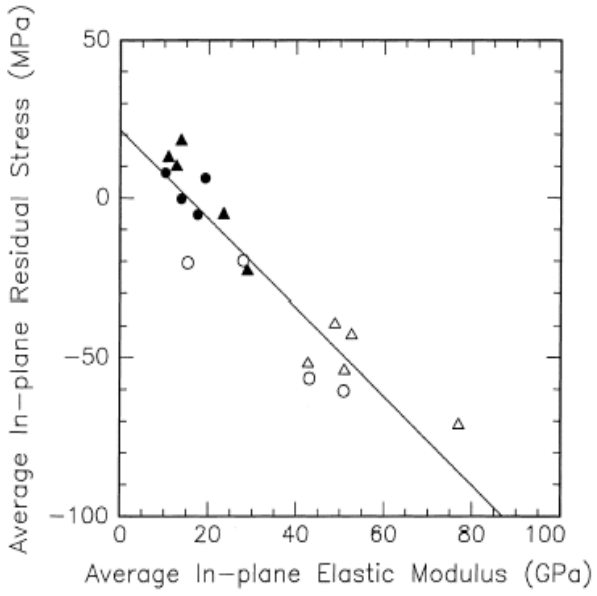

Figure 2.9: Johnson *et al.* show that the average in-plane residual stress decreases with an increase in the average in-plane elastic modulus for a) filled circle measurements are normal to the growth rotation axis and b) filled triangle measurements are parallel to the growth rotation axis [21].

It is clear that geometric changes to the membrane structure influence the performance of piezoelectric membranes. Typically, the piezoelectric material is sandwiched between electrodes in the fashion of a capacitor, in order to collect the charge that is output during use. The geometry of the electrodes has been configured in many ways, in order to understand an electrode design that collects the most output from the piezoelectric layer. Trolier-McKinstry *et al*., in order to create optimal performance from an accelerometer, utilized an interdigitated electrode pattern [15]. The sensitivity of their piezoelectric accelerometer ranged from 1.3 to 7.86 mV/g with corresponding resonant frequencies of 23 to 12 kHz. These sensitivities are approximately 10 times higher than that found with through thickness poling. Since the accelerometer in this case is much

like a simple spring mass system, the spring constant is effectively utilized as a stiffness coefficient that is dependent on the radii of the interdigitated annular electrodes on a circular membrane.

With several ideas for improving the performance of a vibrating piezoelectric membrane, it is imperative to create models that integrate several of these factors, in order to predict and verify experiment results. For instance, fundamental expressions were utilized to derive an analytical expression for the total mechanical stress, σ_1, that incorporates the piezoelectric constants, e_{31} and d_{31}, the compliance terms, s_{11} and s_{12}, and the modulus, E_3, for a circular membrane geometry, as given in [14] by

$$\sigma_1 = \frac{-d_{31}E_3}{s_{11}^E + s_{12}^E} = -\tilde{e}_{31}E_3 \qquad (1)$$

The subscripts *1* and *3* indicate directions where *1* is in the plane of the membrane and *3* is in the direction orthogonal to the membrane. The effective piezoelectric constant, $\tilde{e}_{31}$, is larger than e_{31} that is defined for full clamping. It should also be noted that the compliance term s_{12}^E is always negative because of its placement in the inverted stiffness coefficient matrix. In the analytical calculations non-linear effects were neglected, clamping was assumed to be perfect, and the membranes were assumed to be perfectly circular. This group proposed in a separate paper a method of controlling the damping of the piezoelectric layers [23]. Experimentally a polymer was sandwiched between two piezoelectric layers and was then mechanically excited. Charge was drawn off by a charge-sensitive preamplifier. Properties of this configuration were examined and many useful expressions for relating resonance and capacitance were derived.

In addition to this model and the others utilized by the several research groups discussed here, a parametric study was conducted that determined how active stiffening influences the dynamic behavior of piezo-hygro-thermo-elastic laminates [24]. A nine-node field consistent Lagrangian element was utilized to model both plates and shells. They found that the efficiency decreases with an increase in the curvature of a membrane. It was also found that the stiffening was highly affected by the boundary conditions for both clamped and simply supported cases. Similarly Timoshenko *et al*. provides a thorough description of derived analytical methods of characterizing piezoelectric plates and shells [25].

References

[1] A.M. Flynn, L.S. Tarvrow, S.F. Bart, R.A. Brooks, D.J. Ehrlich, K.R. Udayakumar, L.E. Cross, "*Piezoelectric micromotors for microrobots*," Journal of Microelectromechanical Systems **1** (1992) p. 44.

[2] P. Muralt, "*PZT thin films for microsensors and actuators: where do we stand?*" IEEE Trans. Ultrason. Ferroelectr. Freq. Contr. **47** (2000) p. 903.

[3] P. Muralt, *"Piezoelectric thin films for MEMS,"* Integrated Ferroelectrics **17** (1997) p. 297-307.

[4] P. Muralt, M. Kohli, T. Maeder, A. Kholkin, K. Brooks, N. Setter, R. Luthier, *"Fabrication and characterization of PZT thin-film vibrators for micromotors,"* Sensors and Actuators A **48** (1995) p. 157-165.

[5] G.-A. Racine, R. Luthier, N.F. deRooij, Proceedings of the IEEE-MEMS **93** (Ft. Lauderdale, USA, 1993) p. 128.

[6] E.L. Colla, A.L. Kholkin, D. Taylor, A.K. Tagantsev, K.G. Brooks, N. Setter, "*Characterization of the fatigued state of ferroelectric PZT thin-film capacitors*," Microelectronic Engineering **29** (1995) p. 145.

[7] P. Muralt, A. Kholkin, M. Kohli, T. Maeder, N. Setter, *"Characterization of PZT thin films for micromotors,"* Microelectronic Engineering **29** (1995) p. 67-70.

[8] T.M. Kamel, F.X.N.M. Kools, G. deWith, "*Poling of soft piezoceramic PZT*," Journal of the European Ceramic Society **27** (2007) p. 2471.

[9] A. Kholkin, E. Colla, K. Brooks, P. Muralt, M. Kohli, T. Maeder, D. Taylor, N. Setter, "*Interferometric study of piezoelectric degradation in ferroelectric thin films*," Microelectronic Engineering **29** (1995) p. 261.

[10] F. Xu, S. Trolier-McKinstry, W. Ren, B. Xu, Z-L. Xie, K. Hemker, *"Domain wall motion and its contribution to the dielectric and piezoelectric properties of lead zirconate titanate films,"* Journal of Applied Physics **89** 2 (2001) p. 1336-1348.

[11] L. Vergara, M. Clement, E. Iborra, A. Sanz-Hervas, J. Gacia Lopez, Y. Morilla, J. Sangrador, M. Respaldiza, *"Influence of oxygen and argon on the crystal quality and piezoelectric response of AlN sputtered thin films,"* Diamond and Related Materials **13** 4-8 (2003) p. 839-842.

[12] P. Muralt, Tutorial Notes: Materials Research Society Fall 2003.

[13] J.V. Martinez, "*Fabrication, Materials, and Characterization for Efficient MEMS Power Generation*," Masters Thesis, Washington State University (2004).

[14] P. Muralt, A. Kholkin, M. Kohli, T. Meader, *"Piezoelectric actuation of PZT thin film diaphragms at static and resonant conditions,"* Sensors and Actuators A **53** (1996) p. 398-404.

[15] H. Yu, L. Zou, K. Deng, R. Wolf, S. Tadigadapa, S. Trolier-McKinstry, *"Lead zirconate titanate MEMS accelerometer using interdigitated electrodes,"* Sensors and Actuators A **107** (2003) p. 26-35.

[16] M. Dubois, P. Muralt, "*PZT Thin Film Actuated Elastic Fin Micromotor,*" IEEE Transactions on Ultrasonics, Ferroelectrics, and Frequency Control **45** (1998) p. 1169-1177.

[17] O. Al-Hattamleh, J. Cho, R. Richards, D. Bahr, C. Richards, "*The effect of design and process parameters on electromechanical coupling for a thin-film PZT membrane*," Journal of Microelectromechanical Systems **15** (2006) p. 1715-1725.

[18] C-C. Ma, C-H. Huang, *"Experimental whole-field interferometry for transverse vibration of plates,"* Journal of Sound and Vibration **271** (2004) p. 493-506.

[19] T. Irie, G. Yamada, M. Sonada, *"Natural frequencies of square membrane and square plate with rounded corners,"* Journal of Sound and Vibration **86** 3 (1983) p. 442-448.

[20] J. Cho, J. Raupp, M. Anderson, R. Richards, D. Bahr, C. Richards, "*Optimization of Electromechanical Coupling for a Thin Film PZT Membrane. Part I: Modeling,*" Journal of Micromechanics and Microengineering **15** (2005) p. 1797-1803.

[21] C. Johnson, J. Ruud, R. Bruce, D. Wortman, *"Relationships between residual stress, microstructure and mechanical properties of electron beam-physical vapor deposition thermal barrier coatings,"* Surface and Coatings Technology **108-109** (1998) p. 80-85.

[22] M.S. Kennedy, A.L. Olson, J.C. Raupp, N.R. Moody, D.F. Bahr, "*Coupling Bulge Testing and Nanoindentation to Characterize Materials Properties of Bulk Micromachined Structures,*" Microsystem Technologies **11** (2005) p. 298-302.

[23] Y. Nemirovsky, A. Nemirovsky, P. Muralt, N. Setter, *"Design of a novel thin-film piezoelectric accelerometer,"* Sensors and Actuators A **56** (1996) p. 239-249.

[24] S. Raja, P.K. Sinha, G. Prathap, D. Dwarakanathan, *"Influence of active stiffening on dynamic bahaviour of piezo-hygro-thermo-elastic composite plates and shells,"* Journal of Sound and Vibration **278** 1-2 (2004) p. 257-283.

[25] S. Timoshenko, S. Woinowsky-Krieger, Theory of Plates and Shells, McGraw-Hill, New York (1959).

CHAPTER 3

CHARACTERIZATION TOOLS

The mechanical properties of thin film membranes can be characterized with different techniques including nanoindentation [1, 2] and several variations of bulge testing methods [3, 4, 5]. A few of the properties that describe piezoelectric thin film membranes for MEMS include the composite residual stress, the coupling coefficient, the amount of charge output, and the transverse piezoelectric coefficient. Techniques that are frequently used to define these properties are static and dynamic pressurization while measuring the deflection [6, 7], electrometry [8], and impedance analysis [9]. The research discussed here utilized each of these techniques, in order to determine and define a membrane's optimal behavior. Optimal behavior is dependent on the type of application that the membrane is used for, thus each description that follows in this chapter will pertain to a specified membrane application. Also included is a discussion of the methods for obtaining specific results with each technique.

3.1 Static Pressure Deflection

The ability to pressurize a membrane to a specific deflection is important in this research for determining both the residual stress in the membrane, which is accumulated during processing, and the stiffness of the membrane. Figure 3.1(a) shows a 4 mm membrane that is glued with *Crystalbond 555* to a clamped puck. Contact probes are directly above the top and bottom electrode access points. Figure 3.1(b) shows the entire setup that includes the clamped membrane with contact probes, a bellows that evenly

increases or decreases the amount of applied pressure, and a pressure gauge that is connected to a computer for recording the pressure. The pressure gauge has an accuracy of 0.25% best fit straight line (BFSL), which for example means that for 10 psi there is an accuracy of ± 0.025 psi. A laser vibrometer is typically incident on the surface of the center of the membrane. This signal is reflected back into the photodetector of the laser vibrometer and a change in the velocity of the incident to reflected signals is translated into a change of the location of the membrane surface, or deflection. The resolution of the deflection measured by the laser vibrometer is subnanometer, according to the Polytec Interferometer OFV 5000 specifications. However, after testing several membranes it was determined that the standard deviation in the deflection data at a pressure of 10 kPa was 0.75 µm.

a) 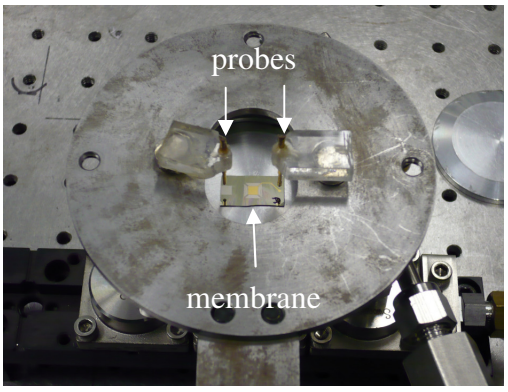

b) 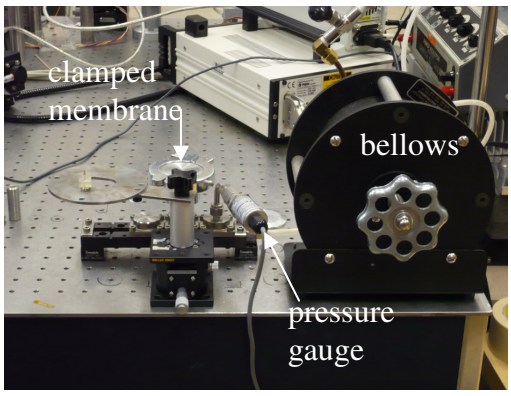

Figure 3.1: A 4 mm membrane sample is a) glued to a clamped puck with probes directly above the top and bottom electrode access points, while in b) the static bulge test setup includes a clamped membrane, contact probes, a bellows, and a pressure gauge.

During a typical experiment the laser vibrometer is initially zeroed, in order to measure incremental changes in the amount of deflection. The membrane is pressurized

with the bellows to a specified deflection, which can be either in a positive or negative direction. The positive position means that the membrane is deflected outward from the applied pressure. The negative position means that a vacuum is pulled on the membrane and the membrane deflects towards the applied pressure. While the pressure is applied to the membrane, the pressure and deflection are recorded by a LabView computer program. Typical resulting pressure vs. deflection curves are shown in figure 3.2.

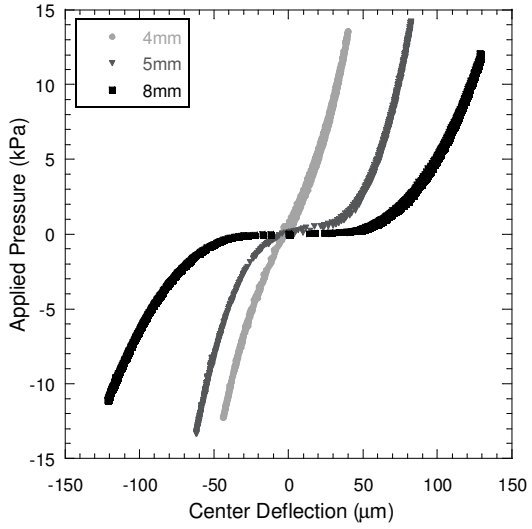

Figure 3.2: Typical static pressure vs. deflection curves for 4, 5, and 8 mm membranes.

Prior to the establishment of this characterization tool, the pressure vs. deflection curve was constructed from incremental data collection and an extension of a curve through the data points, which could have been a source of error in further calculations. The pressure gauge used in this research allows for a pressure range of -100 kPa to 100 kPa, which is large enough to encompass the extent of most membrane testing. In order to reach higher pressures, a different pressure gauge must be used. The only limitation of the bellows is

during testing 3 mm and sometimes 4 mm membranes to failure. In this case, the range of the bellows, which is approximately the same as the pressure gauge, is surpassed with pressurized argon that is connected directly through the bellows system and controlled at the argon tank. The settings in the LabView program can be changed to account for higher pressures. Similarly, the settings can be changed in the software program to account for deflections that exceed the standard setting of 16 μm/V.

The residual stress of the composite membrane is calculated from the pressure vs. deflection curve. The pressure vs. deflection curve can be curve fit with [10]

$$P(\delta) = E_B \frac{t^3 \delta}{(.015)a^4} + \frac{(3.40)\sigma_0 t \delta}{a^2} + \frac{(1.82)E_B t \delta^3}{a^4} \qquad (1)$$

where δ, E_B, t, a, and σ_0 are the deflection, biaxial modulus, membrane thickness, half the membrane side length, and the residual stress within the membrane, respectively. The variables in this expression are known except for the residual stress, assuming that the biaxial modulus is well established. In the case that the biaxial modulus is not well know, the pressure vs. deflection curve can be fit with

$$\begin{aligned} P(x) &= C_1(x - x_{offset}) + C_2(x - x_{offset})^3 - P_{offset} \\ C_1 &= \frac{3.4\sigma_0 t}{a^2} \\ C_2 &= \frac{1.82E_B t}{a^4} \end{aligned} \qquad (2)$$

where P is the pressure and x is the deflection. C_1 and C_2 have units of kPa/μm and kPa/μm^3, respectively. There may be an offset for both the pressure and the deflection, in order to account for the pressure vs. deflection curve not going through zero. C_1 can be utilized for calculating the residual stress in the membrane and C_2 can be used to calculate the biaxial modulus of the membrane. These expressions are useful because

they eliminate the need to assume one variable while determining the other. However, the fit does not provide a unique solution, since the variables could be slightly different for each membrane. This characterization tool is used to determine the residual stress and modulus of several of the composite membranes described in the following chapters.

In order to determine the stiffness of the membrane, k_s, the pressure vs. deflection curve is converted to a force vs. deflection curve. The force is calculated by dividing the pressure by the area of the membrane. The resulting curve is not linear, since the pressure vs. deflection was cubic in deflection. Therefore, the stiffness of the membrane is equal to the slope along the curve. The stiffness is

$$k_s = \frac{dF}{d\delta} \tag{3}$$

where F is the force and δ is the deflection of the membrane. The stiffness is included in Chapter 4, in which the design of a membrane that demonstrates improved behavior is described.

3.2 Electrometer

In order to measure the amount of charge produced by the piezoelectric thin film during active straining of the membrane, a Keithley 617 electrometer was connected in parallel to the membrane. This electrometer is useful because it is well grounded and can directly measure the charge produced when the membrane is strained. The precision of this instrument allows for low charge readings of down to 0.01 nC. This is important because the charge output of a typical piezoelectric film in this research ranged from 1.00 to 200.00 nC. With this range of possible charge output and in order for the noise level to

decrease to 0.01 to 0.04 nC, it is necessary to allow the instrument to warm up for at least an hour prior to use.

During setup of the experiment and after waiting for at least an hour for the instrument to warm up, the alligator clips can be connected to the probes that contact the top and bottom electrodes that sandwich the piezoelectric film in the membrane. The electrometer was typically used in combination with the static pressure deflection setup, in order to measure the charge, deflection, and pressure simultaneously. The method of measuring the charge output from the piezoelectric film included pressurizing the membrane to a specific deflection, zeroing the electrometer so that it displays 0.01 to 0.04 nC, and simultaneously opening the pressure valve on the bellows to release the pressure. The release of pressure allows the membrane to return to a zero deflection state and the electrometer to measure all of the charge output from the piezoelectric film. The charge should be recorded once the amount of charge has stabilized on the electrometer screen or a predetermined amount of time passes after the membrane is depressurized. Typically the amount of charge stabilized after three to five seconds after depressurization. However, on occasion the amount of charge reached a peak and then started to decrease. Thus, it is important to watch the electrometer display, so that the peak charge output is recorded. This type of experiment was found to be reproducible for membranes that are fully poled, which is discussed in Chapter 8.

The charge measurements that are determined with the electrometer were utilized to calculate the transverse piezoelectric coefficient, e_{31}, and the electrical energy produced, E, for several HOAc PZT films. Initially, the noise level must be subtracted

from the peak charge that was recorded, in order to provide the actual charge produced by the film. Then, in the case of a rectangular film, the actual charge is inserted into

$$e_{31} = \frac{Q}{A\varepsilon_1} \tag{4}$$

where Q is the actual charge produced by the piezoelectric material, A is the area of the top electrode, and ε_1 is the in-plane uniaxial strain induced during deflection. For the case of a square membrane, the actual charge is inserted into

$$e_{31} = \frac{3}{4}\frac{Qa^2}{\delta^2 A} \tag{5}$$

where a is half of the membrane's side length and δ is the deflection at the center of the membrane. The electrical energy for a square membrane was calculated with

$$E = \frac{2}{3}\frac{e_{31}\delta^2 A}{Ca^2}Q \tag{6}$$

where C is the stationary capacitance of the membrane. A complete description of how each of these expressions is determined is discussed in Chapter 7.

3.3 Dynamic Pressure Deflection

Another source of insight into the performance of a membrane requires dynamic operation. In the setup used for this research the membrane is mechanically forced to oscillate at a specified frequency, in order to make the piezoelectric film within the composite membrane produce charge continuously. The entire dynamic bulge tester without a sample is shown in Appendix III. A micrometer extends from the base of the instrument. Appendix III also provides a cross section of the interior of the bulge test setup. The interior of the instrument contains a piezoelectric actuator that pushes on a

stainless steel diaphragm. The diaphragm in turn pushes on a column of deionized water that forces the membrane the move. The oscillation of the piezoelectric actuator causes the membrane to oscillate. If the charge produced by the membrane oscillation is sent across a resistor, then the amount of output power can be determined at different frequencies of oscillation. It is important to note that the frequency utilized during the membrane's dynamic operation is the system frequency. Therefore, the resonant frequency found for each experiment is actually the system frequency, which includes the membrane and the entire setup, not the resonant frequency found by any other method. The scale of power produced is dependent on what type of membrane, the frequency, and the amount of force used to actuate the membrane. Utilizing the curves produced during operation, the mechanical work can be calculated as well. In general, dynamic operation of the piezoelectric membrane provides a good resource for understanding the performance for several types of applications including those that require power and those that do not.

Before dynamic operation can begin, the entire system must be configured so that there are no bubbles within the column of water that could interfere with the operation of the membrane. If the bulge tester has been sitting for a few days unused, this will require reassembling the interior of the bulge tester with a deionized water filled cavity. Instruction of how to do this is explicitly described by Skinner [11]. If by chance the bulge tester has been used, but there seems to be interference in the output signal from the membrane, then reassembling or use of the instrument without the membrane may be required. There may be a few small bubbles that need worked out of the system or have gotten trapped along the sides of the cavity. Once the system is operating with a clean

output signal, the chance of popping the membrane because of the setup itself is significantly reduced. Before placing the membrane over the hole at the top of the tester, make sure that there is a significant droplet of deionized water covering the hole, as shown in Appendix III. The mean pressure should also be zeroed at this time. This is done by rotating the screw in the piezoelectric actuator box. One of the oscilloscope channels should be dedicated to the output of the piezoelectric actuator, in order to monitor the mean pressure. The membrane should be placed in a carrier that can be clamped to the top of the bulge tester with a clamping bar, as shown in figure 3.3.

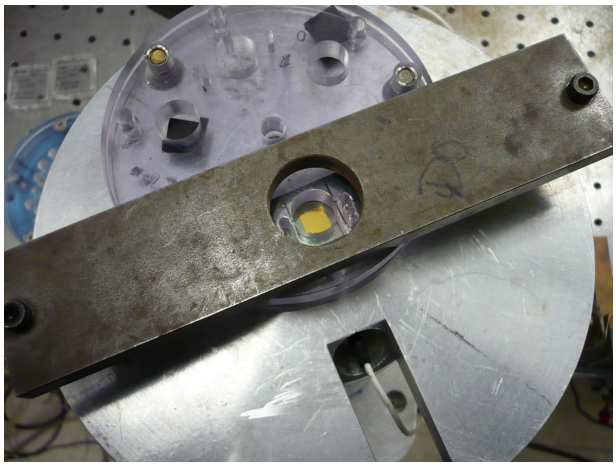

Figure 3.3: The sample is loaded into the plexiglass carrier with gasket material pieces distributed for even clamping. A bar is placed over the carrier to clamp the carrier in place. The hole in the bar provides probe access to the top and bottom electrodes.

Even clamping is important in both the loading of the membrane into the carrier and while clamping the carrier to the tester. While clamping down the carrier monitor the mean pressure because the water trapped under the membrane will force the membrane to bulge out. Turning the micrometer slightly, not the piezoelectric actuator screw, will

allow the membrane to return to a neutral position. When the carrier is fully clamped to the bulge tester make sure that the membrane is flat, which means it is in a neutral position. Place magnetic probes onto the clamping plate and check for capacitance of the membrane, in order to verify that there is a good electrical connection. The laser vibrometer should be set so that it is incident on the center of the membrane and there is full signal being detected by the photodiode. Typically, a laser vibrometer setting of 80 μm/V was used to capture the entire oscillating signal on the oscilloscope.

With the entire setup configured and the membrane ready for testing, the next step is to dynamically operate the membrane. Appendix III shows a schematic of the setup with the electrical connections for the open circuit configuration, in which the output of the membrane is directly monitored by the oscilloscope. The typical electrical connection setup included the laser vibrometer output connected to channel one of the oscilloscope, the output of the signal generator connected to channel two of the oscilloscope, the output of the pressure transducer connected to channel three of the oscilloscope, and the output of the membrane connected to channel four of the oscilloscope. During initial operation of the membrane it is necessary to determine the system resonance with an open circuit configuration, which is provided in Appendix III. An open configuration indicates that the output from the membrane is directly measured by an oscilloscope.

If the load resistance is placed in the path between the membrane and the oscilloscope, then the output power can be determined, which is called the closed circuit configuration. Figure 3.4 shows the typical electrical configuration for the closed circuit configuration.

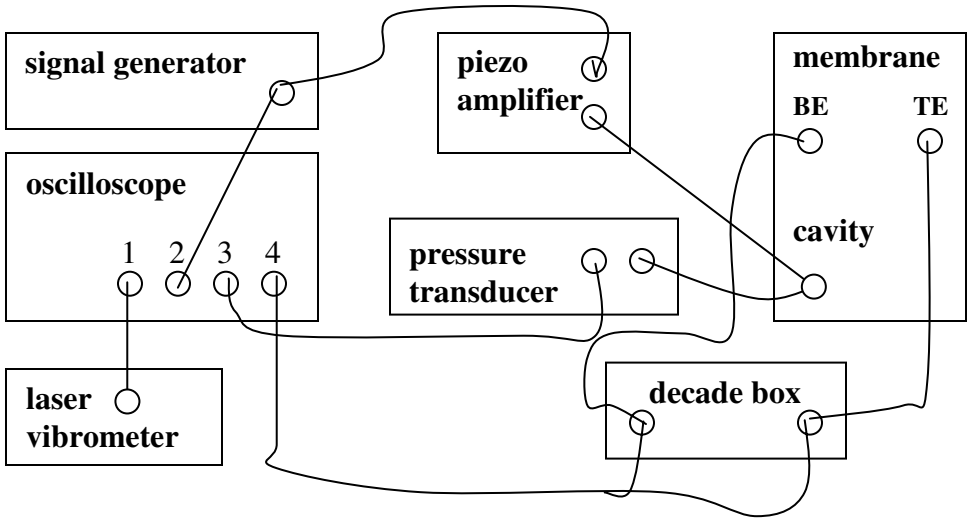

Figure 3.4: Schematic of electrical connections for the closed circuit configuration.

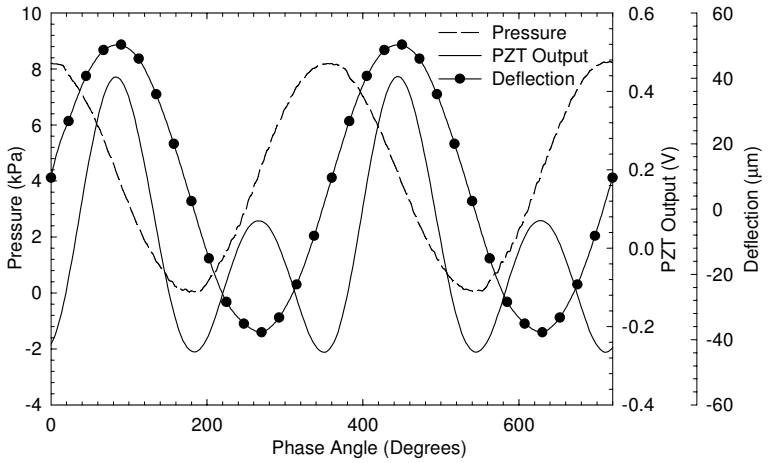

Figure 3.5: Typical oscillation curves for a membrane dynamically operating with the open circuit configuration at system resonance. Notice the 90º phase shift between the pressure and open voltage curves.

Begin with the lowest input voltage and frequency. Turn the piezoelectric amplifier on only after these inputs have been set. The mean pressure will need adjusted with the

micrometer under the bulge test instrument. Slowly ramp the frequency. The voltage output from the membrane will oscillate and increase in amplitude. When the amplitude peaks the system resonance has been found. This can be verified by a 90º shift between the pressure and output voltage signals. Figure 3.5 shows a typical oscillation curve set for the pressure, center deflection, and open circuit voltage output during operation at system resonance.

A few key aspects to be aware of during testing include the difference between the peak-to-peak pressure and the mean pressure, the peak-to-peak vs. root mean square (rms) output voltage from the membrane, and converting from volts to μm or kPa. The peak-to-peak pressure is the pressure amplitude of the pressure oscillation. The mean pressure is the level of pressure about which the membrane oscillates. The peak-to-peak pressure is changed by changing the voltage input from the signal generator. The mean pressure is changed by twisting the micrometer that extends from the bottom of the bulge testing instrument. Changing either pressure will cause the system resonance to change slightly because it effectively changes the stiffness of the membrane. Because the output voltage signal from the dynamic system is not sinusoidal, the rms output voltage should be measured instead of the peak-to-peak output voltage. In the case that the output signal is not saved during operation, the rms output value can be approximated by

$$V_{RMS} = \frac{V_{pp}}{\sqrt{8}} \tag{7}$$

A full description of how this is derived is provided in Chapter 8. The setting on the laser vibrometer indicates the conversion for obtaining the deflection in units of microns. The pressure signal levels are converted from volts to kPa by

$$kPa = \frac{V}{0.098}\left(\frac{6894.7573}{1000}\right) \tag{8}$$

The dynamic oscillation of the piezoelectric membrane provides several pieces of information that can be combined to determine the behavior of the membrane under different operating conditions. One of the key pieces of information is the amount of output power provided by the oscillating membrane. Other characteristics include the mechanical and electrical work, from which the efficiency of the energy conversion by the membrane to produce the output power can also be determined. These behavioral characteristics are important to applications that involve membrane oscillation at specific frequencies. The conditions under which the membrane operates can be adjusted to follow specifications. Utilizing the dynamic bulge test system enables the user to demonstrate the membrane's capabilities under oscillating conditions. The data that can be determined with this system includes the oscillation curves for the deflection, pressure, and voltage output from the membrane. In addition, specific details such as the operating system frequency, mean pressure, peak-to-peak pressure, and rms output voltage can be obtained from the equipment during use.

In order to determine the output power produced by the oscillating membrane, the output voltage from the membrane must be connected in a closed circuit with a load resistance. The resistance that produces the highest amount of output power is called the load resistance because it matches the impedance of the membrane as it oscillates within the testing system. The load resistance is found by operating the membrane at system resonance while a decade box is connected to the circuit. With this setup, the resistance can be incrementally changed while the membrane oscillates. The output power is calculated with

$$Power_{rms} = \frac{V_{rms}^2}{R} \tag{9}$$

where V_{rms} and R are the rms output voltage and the resistance. Figure 3.6 shows how the output power peaks as the resistance is incrementally changed during dynamic operation.

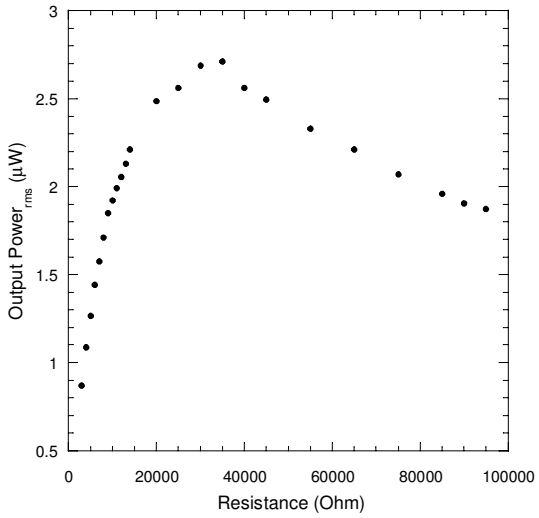

Figure 3.6: Typical output power vs. resistance plot used to determine the load resistance that matches the impedance of the oscillating membrane. This particular membrane had a PZT thickness of 1.5 μm and a frequency of 447 Hz was used.

The load resistance can also be estimated with

$$R_L = \frac{1}{2\pi f C_0} \tag{10}$$

where f is the frequency of operation and C_0 is the stationary capacitance of the membrane. This equation is used for resonant operating conditions, but experiment has shown that it is applicable to off resonant conditions as well for this dynamic operating system. It is important to note that as the frequency of operation changes, the load

resistance must be changed as well, in order to determine the peak output power for any specific operating condition. However, the estimation of the load resistance is typically within 1-2 Ω, which is good considering the load resistance that is required for impedance matching is typically around 10 kΩ. Therefore, the dynamic bulge testing system can be operated with different operating conditions to provide output power that is suitable for specific application requirements.

In addition to the output power, the mechanical and electrical work can be determined using the data provided by the dynamic bulge test system. Utilizing the data for the deflection curve, the volume for each time increment can be calculated with

$$Vol = \frac{4a^2}{\pi^2}\delta \tag{11}$$

where a is the membrane side length and δ is the center deflection of the membrane. This expression is the result of performing

$$Vol = \int_0^a \sin(\frac{\pi x}{a})dx \int_0^a \sin(\frac{\pi y}{a})dy \tag{12}$$

The double integral over the sinusoidal motion of the membrane approximates the volume under the deflected membrane in a similar way to that provided by Vlassak *et al*. [12]. The next step is to calculate the mechanical work. This involves taking the time derivative of the volume and multiplying by the pressure. Integrating this result with respect to time provides the mechanical work, W_{mech}, as given by,

$$W_{mech} = \int P \frac{dVol(t)}{dt} dt \tag{13}$$

The electrical work, W_{elec}, is calculated with

$$W_{elec} = \frac{Power_{rms}}{f_{system}} \tag{14}$$

The efficiency of the energy conversion by the membrane to produce the output power is calculated with

$$\eta_P = \frac{W_{elec}}{W_{mech}} \tag{15}$$

In summary, the dynamic bulge test system provides not only the output power from the oscillating membrane, but it also provides data that enables the calculation of the mechanical and electrical work the ratio of which provides the efficiency of the power generation by the membrane.

3.4 Impedance Analyzer

An impedance analyzer can be used to determine many frequency dependent phenomena of thin film membranes. In this research an Agilent 4294A Precision Impedance Analyzer was used to excite the piezoelectric membrane to low deflections that maintained plate-like membrane behavior. In other words, the peak membrane deflections did not exceed the thickness of the membranes. This type of actuation enables the determination of the membrane behavior in terms of the quality factor, Q, the coupling coefficient, k^2, and the efficiency, η.

The typical setup for each experiment involves a membrane holder, the connecting cable from the instrument to the probes that access the top and bottom electrodes, and the impedance analyzer. Figure 3.7 shows the typical setup with each of the necessary components.

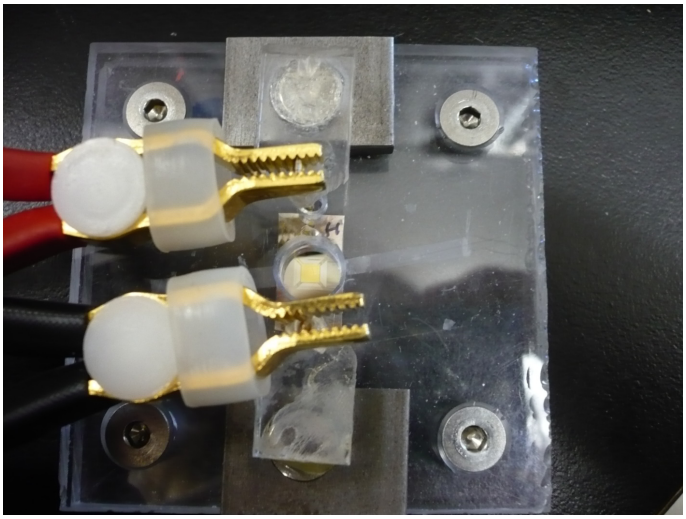

Figure 3.7: A 4 mm membrane sample is clamped between two plexiglass plates. The probes are held in place with magnets. The impedance analyzer cables are connected to the instrument with the probes.

The details of how to operate the impedance analyzer is described by Cho [13]. For the purpose of describing the experiments conducted in this research, however, a brief description follows. After the membrane is fully poled, the sample is loaded into the holder. It is necessary to make sure that the corners of the membrane are not pinned by the holder, in order to allow the membrane to have a full range of motion. The sample should be grounded by connecting the probes that access the electrodes, in order to eliminate any residual charge that has collected on it. The impedance analyzer can then be connected to the sample via the connecting cable. Let the holder hang freely in the air instead of resting on a table. This eliminates any additional frequency response from the environment. Once a frequency range is selected on the impedance analyzer, the objective is to determine the resonant frequency, which corresponds to the highest peak in the phase curve. There is a corresponding impedance curve to this frequency that

provides the information to determine the behavior properties of interest in this research. A typical plot of the impedance curve is shown in figure 3.8.

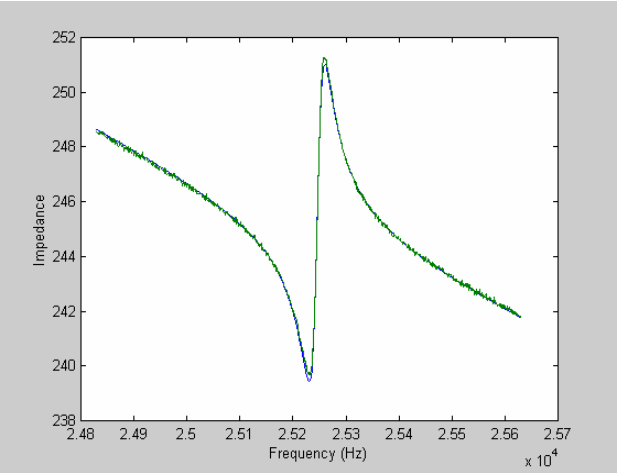

Figure 3.8: Typical impedance curve with *Matlab* curve fit overlay.

Analysis of the impedance curve requires a curve fit to the impedance curve. In order to establish a curve that fits the data, an equivalent circuit is utilized that incorporates the equivalent analog circuit components for the piezoelectric material within the composite membrane. There is a full description of the equivalent circuit that is used in this research by Cho [13]. Utilizing the equivalent circuit equations from Cho's research, a curve fitting program was created with the software *Matlab*, in order to define a curve fit that fits the impedance data and incorporates each of the circuit components. Figure 3.8 shows a curve fit overlaying the impedance data. The specifics of the code, which was generated for the research described here, are explicitly provided in Appendix I. When the data is fit well by the curve generated by this code, the results obtained are the values for each of the circuit components (R_m, L_m, C_m, and C_0), the

coupling coefficient, the resonant frequency, and the quality factor. The coupling coefficient is calculated by using

$$k^2 = \frac{C_m}{C_o + C_m} \tag{16}$$

where C_m and C_0 are the equivalent mechanical capacitance of the PZT and the stationary capacitance of the membrane, respectively. The resonant frequency is calculated with

$$f_r = \frac{1}{2\pi\sqrt{L_m C_m}} \tag{17}$$

where L_m is the equivalent mechanical inductance of the PZT. The quality factor is calculated with

$$Q = 2\pi f_r \frac{L_m}{R_m} \tag{18}$$

where R_m is the equivalent mechanical resistance for the PZT within the composite membrane. The expression for the efficiency is a combination of the coupling coefficient with the quality factor.

$$\eta = \frac{\frac{1}{2}\frac{k^2}{1-k^2}}{\frac{1}{Q} + \frac{1}{2}\frac{k^2}{1-k^2}} \tag{19}$$

The load resistance, R_L, can also be calculated with the results from the impedance data by (10). This value is utilized when determining what load to put in parallel with the membrane during dynamic operation, in order to impedance match and therefore determine the peak power output by the piezoelectric membrane. A table of typical results for each of these calculations is provided in Table 3.1 for three different 5 mm membranes.

Table 3.1: Typical impedance results for three different 5 mm membranes.

C_o (F)	R_m (Ω)	L_m (H)	C_m (F)	k^2	f_r (Hz)	Q	η	R_L (Ω)
2.81E-08	38200	32.6	2.05E-11	7.31E-04	6150	32.9	1.19	921
2.72E-08	5580	49.2	1.18E-11	4.32E-04	6610	36.7	0.79	886
2.78E-08	25900	35.9	1.81E-11	6.52E-04	6230	54.2	1.74	919

Operating the piezoelectric membrane with conditions that provide plate-like behavior offers good insight into the fundamental behavior of the membrane. It also provides useful characterization that can be utilized when designing for optimal performance in a particular thin film membrane application.

3.5 Uncertainty in Measurements

Each piece of equipment used has a resolution that is stated in the respective section in this chapter. However, to calculate the uncertainty in the measured data, the following method was utilized. For example, in order to determine the uncertainty in the deflection, several membranes were pressurized to 10 kPa at which the laser vibrometer was used to measure the deflection. The mean, $\bar{x}$, of these deflections was then calculated with

$$\bar{x} = \frac{1}{N}\sum_{i=1}^{N} x_i \tag{20}$$

where x_i is the deflection in each measurement and N is the number of measurements. The standard deviation, σ, was then calculated with

$$\sigma = \sqrt{\frac{1}{N}\sum_{i=1}^{N}(x_i - \bar{x})^2} \tag{21}$$

The standard deviation indicates how much uncertainty there is in the measurement of one variable. In the case that there are several variables measured and then combined in an equation, the uncertainty in the result of the equation involves further calculation [14]. For example, in the case of the power produced by a membrane, $P=V^2/R$, the standard deviation of the power is calculated with

$$\sigma_P^2 = (\frac{\partial P}{\partial V})^2 \sigma_V^2 + (\frac{\partial P}{\partial R})^2 \sigma_R^2 \qquad (22)$$

The number of partials depends on the number of variables within the equation. Each of the standard deviations stated in the following chapters were calculated with this method.

References

[1] N. Pugno, B. Peng, H.D. Espinosa, "*An analysis of the membrane deflection experiment used in the investigation of mechanical properties of freestanding submicron thin films*," International Journal of Solids and Structures **42** (2005) p. 647-661.

[2] M. Jozwik, P. Delobelle, C. Gorecki, A. Sabac, L. Nieradko, C. Meunier, F. Munnik, "*Optomechanical characterization of compressively prestressed silicon oxynitride films deposited by plasma-enhanced chemical vapour deposition on silicon membranes*," Thin Solid Films **468** (2004) p. 84-92.

[3] J.F. Shepard Jr., P.J. Moses, S. Trolier-McKinstry, "*The wafer flexure technique for the determination of the transverse piezoelectric coefficient (d_{33}) of PZT thin films,"* Sensors and Actuators A **71** (1998) p. 133-138.

[4] A. Karimi, O.R. Shojaei, T. Kruml, J.L. Martin, "*Characterisation of TiN thin films using the bulge test and the nanoindentation technique*," Thin Solid Films **308-309** (1997) p. 334-339.

[5] B. Schoeberle, M. Wendlandt, C. Hierold, "*Long-term creep behavior of SU-8 membranes: Application of the time-stress superposition principle to determine the master creep compliance curve*," Sensors and Actuators A, *Article in Press* (2007).

[6] P. Muralt, M. Kohli, T. Maeder, A. Kholkin, K. Brooks, N. Setter, R. Luthier, "*Fabrication and characterization of PZT thin-film vibrators for micromotors*," Sensors and Actuators A **48** 2 (1995) p.157-165.

[7] I. Demir, A.L. Olson, J.L. Skinner, C.D. Richards, R.F. Richards, D.F. Bahr, "*High strain behavior of composite thin film piezoelectric membranes*," Microelectronic Engineering **75** (2004) p. 12-23.

[8] P. Ochoa, J.L. Pons, M. Villegas, J.F. Fernandez, "*Effect of bonding layer on the electromechanical response of the cymbal metal-ceramic piezocomposite*," Journal of the European Ceramic Society **27** (2007) p. 1143-1149.

[9] M. Buigas, F.M. Espinosa, G. Schmitz, I. Ameijeiras, P. Masegosa, M. Dominguez, "*Electro-acoustical characterization procedure for cMUTs*," Ultrasonics **43** (2005) p. 383-390.

[10] E. Bonnotte, P. Delobelle, L. Bornier, "*Two interferometric methods for the mechanical characterization of thin films by bulging tests. Application to single crystal silicon*," Journal of Materials Research **12** 9 (1997) p. 2234.

[11] J.L. Skinner, "*Piezoelectric membrane generator characterization and optimization*," Masters Thesis, Washington State University (2002).

[12] J.J. Vlassak, W.D. Nix, "*A new bulge test technique for the determination of Young's modulus and Poisson's ratio of thin films*," Journal of Materials Research **7** 12 (1992) p. 3242-3249.

[13] J.H. Cho, "*Electro-mechanical characterization of piezoelectric for MEMS power*," Masters Thesis, Washington State University (2004).

[14] A.C. Melissinos, Experiments in Modern Physics, Academic Press, New York (1966).

CHAPTER 4

GEOMETRIC CHANGES

Micropower sources are increasingly becoming necessary as devices decrease in size. The battery sources currently available provide more than enough power, but they do not meet the reduced size requirement. Piezoelectric materials convert mechanical strain energy to electrical energy when strained. This energy conversion should be utilized to provide both the micropower and size requirements of various devices. During piezoelectric membrane fabrication however, the residual stress in the composite structure accumulates to typical values of 100 MPa [1]. In order to achieve efficient energy conversion, the residual stress must be minimized. Several research groups have examined various methods to reduce the residual stress with methods that include changing the piezoelectric material, doping the piezoelectric material, and changing the structure of the membrane that encompasses the piezoelectric material [2, 3, 4]. A discussion follows that describes a geometric route to reduce the residual stress of 3 mm square membranes that incorporate lead zirconate titanate (PZT) films with a ratio of Zr to Ti of 40:60. This discussion will also include how the reduced residual stress improves the energy conversion for the membranes.

Also, fundamental to the design of a MEMS piezoelectric device is the characterization of the electromechanical behavior. This behavior is described in part by the coupling coefficient, k^2, and the compliance of the structure. Both of these properties were experimentally determined, however there are several factors that influence them including the amount of residual stress. Several groups have studied PZT and its

ferroelectric properties, in order to utilize this material as a micropower source that provides good performance [5, 6, 7, 8]. The discussion that follows describes how these performance characteristics were improved with geometric changes.

A finite element model, which was previously created, was utilized to determine trends of how specific factors influence k^2 and the compliance of the structure. Modeling was also instrumental in determining the relationship between the amount of residual stress and the coupling coefficient. In addition to conducting finite element modeling, experiments were conducted that realized trends for k^2, the compliance, and the residual stress. Calculations varying the thickness ratio between the silicon and PZT were carried out, which provided an overall peak performance recipe for this micro scale membrane. These calculations and modeling efforts provided the guidelines for the geometric design of the membranes that were utilized in experiments. The intention of this chapter is to describe how to determine the geometry that optimizes these characteristic properties for micromachined piezoelectric membranes.

4.1 Simulations

4.1.1 Finite Element Simulations

Studies were conducted with finite element simulations, which were based on previously developed finite element models, were utilized to characterize the effect of varying geometric aspects such as the boundary conditions, electrode coverage on the flexing piezoelectric membrane, the Si/PZT thickness ratio, and the affect of residual stress on the coupling coefficient [9, 10]. The model developed by Xu does not incorporate the residual stress of the membrane, while the model developed by Al-

Hattamleh did include the residual stress inherent to the membrane. Two types of boundary conditions were investigated including fully clamped and simply supported. The percent of electrode coverage was quantified in relation to the output voltage produced as the membrane deflects. For each of these studies, the Si/PZT thickness ratio was varied from 0.33 and 2 with a silicon thickness of 1.1 μm and a PZT thickness between 0.36 and 2.1 μm. The values for e_{31} and d_{31} for PZT (6.7 C/m^2, 850 pC/N) were experimentally determined using a membrane flexure technique [8]. Simulations of the Si/PZT thickness ratios revealed that these e_{31} and d_{31} properties provide an optimal coupling coefficient and thus were utilized in all of the numerical simulations.

4.1.2 Analytical Calculations

Designing a composite membrane that provides a maximum amount of charge output required the use of analytic calculations. Since the film layers within the composite structure must work together to provide optimal performance, fundamental expressions were adapted with a thickness weighted method. The fundamental expressions were [11],

$$E_B = \frac{E}{1-\nu} \tag{1}$$

where the Young's modulus, E, and Poisson's ratio, υ, are used to determine the biaxial modulus, E_B, and

$$\varepsilon = \frac{\sigma}{E} \tag{2}$$

in which the film strain, ε, is calculated by the ratio of the film stress, σ, and Young's modulus. Equations (1) and (2) were utilized with a thickness weighted method that

determines the total biaxial modulus, E_{BT}, and similarly for the total strain for the composite membrane structure, such as in the total biaxial modulus expression

$$E_{B_T} = \sum_{i=0}^{N} E_{B_i} (\frac{t_i}{t_T}) \tag{3}$$

where t_i and t_T are the layer thickness and the total membrane thickness, respectively. The thickness weighted biaxial modulus and thickness weighted total strain of the composite structure are utilized to determine the composite residual stress for the structure by a modified Hooke's law,

$$\sigma_{r_W} = \left[\sum_{i=1}^{n} E_{B_i} * \left(\frac{t_i}{t_T} \right] * \left[\sum_{i=1}^{n} \left(\frac{\sigma_{r_i}}{E_i} \right. * \left(\frac{t_i}{t_T} \right] \right. \tag{4}$$

where σ_{rW}, E_{Bi}, t_i, t_T, and E_i are the weighted residual stress, biaxial modulus of each layer, thickness of each layer, total thickness, and the modulus of each layer, respectively. The composite residual stress is equal to the product of the thickness weighted biaxial modulus and the total strain, σ_r/E, of the membrane.

The residual stress calculated in (4) was utilized in a model provided by Degen *et al.* [12].

$$f_r = \frac{1}{L * \sqrt{2 * \rho_W}} \sqrt{\left(\frac{1.644 * E_{b_W}}{1 - \upsilon_W^2} \right. * \left(\frac{t_T^2}{L^2} \right. + \sigma_{r_W}} \tag{5}$$

where L, ρ_W, E_{bW}, and υ_W, are membrane side length, the thickness weighted density, thickness weighted biaxial modulus, and thickness weighted Poisson's ratio, respectively. The resonant frequency was investigated because the membranes fabricated will be incorporated into the P3 microengine and the ability to tailor the resonant frequency is important to each device in which the microengine is used [13]. The model provided by

Degen *et al*. was verified against experiment data and it was found that the data falls within ±10% of the model.

The positioning of the neutral axis is optimum, in the case of plate-like behavior, just below the piezoelectric layer so that as the membrane deflects the piezoelectric layer will deflect to its maximum ability and thereby generate the highest amount of charge [14]. The neutral axis position during deflection of the composite membrane is calculated with

$$0 = \int_{z_0}^{z_1} E_0(z - z')dz + \int_{z_1}^{z_2} E_1(z - z')dz + \int_{z_2}^{z_3} E_2(z - z')dz + \ldots \quad (6)$$

where E_0 is the biaxial modulus of each material layer, z is the thickness of the material in each layer, and z' is the position of the neutral axis. The silicon substrate layer corresponds to z_0, the silicon oxide to z_1 and so on for however many layers are in the composite. Several composite membranes were designed using these five expressions. Since the ratio of PZT to silicon thickness is highly influential to the membrane performance, several different thickness ratios were defined. Table 4.1 provides the values used in the experiments. The material properties of Poisson's ratio and elastic modulus for PZT (0.25, 61 GPa) and silicon (0.2, 115 GPa) are published values [15].

4.2 Fabrication Procedures

The membranes discussed in this chapter were fabricated with processing that involved thermally growing a 100 nm silicon oxide from a silicon substrate. Then the silicon was anisotropically wet etched with ethylene diamine pyrocatechol (EDP) to 2.1 µm thick using a boron etch stop, which created 3 mm square membranes. A 175 nm Pt bottom electrode was then sputtered onto the oxide with a 5 nm Ti adhesion layer.

During processing, tensile residual stresses accumulate due to the techniques that are utilized. The largest contributing factor to the residual stress is incurred during the Pt annealing step, in which the sample is heated to 650 ºC that induces plastic flow of the platinum. Upon cooling the tensile stress in the platinum reaches approximately 800 MPa. Next, with a ratio of Zr to Ti of 40:60, 2MOE-based PZT sol-gel deposition involved sequential deposition with rapid thermal annealing iterations at 700 ºC after each 3 layers (approximately 0.25 µm of PZT per annealing step). Further tensile stress accumulation was due to this PZT film deposition process. A top electrode that consisted of 300 nm of Au on a 12.5 nm Ti/W adhesion layer was then sputter deposited onto the PZT [16]. The typical composite residual stress after processing in the membrane was 100 MPa tensile. The total PZT thickness in this study ranged from 1.1 to 2.2 µm. The total composite structure was then patterned with contact photolithography in order to establish the desired geometry.

One fabrication change that occurred, in order to reduce the residual stress of the composite was to thicken the silicon oxide to 1.5 µm and deposit all subsequent layers before wet etching the pits with potassium hydroxide (KOH) to create the membranes [17]. This processing change occurred because the silicon oxide is compressively stressed and it compliments the tensile stresses that accumulate during processing. However, the thickness of silicon oxide required to reduce the composite stress of the membrane would buckle the membrane during initial processing. Thus the pit must be etched after all of the processing steps.

Another fabrication change to the structure of the composite membrane, in order to reduce the amount of residual stress, was to thin the silicon by isotropically wet

etching with HNA. HNA is a mixture of hydrofluoric, nitric and acetic acids. In addition, a compressively stressed 100 nm layer of tungsten was DC Magnetron sputtered onto a few of the membranes to produce a near zero net residual stress [1]. Table 4.1 summarizes the thicknesses used for silicon and PZT and also provides the location of the neutral axis.

Table 4.1: Summary of Si and PZT thicknesses for specific Si/PZT thickness ratios and neutral axis positions.

Si (µm)	PZT (µm)	Ratio Si/PZT	neutral axis location
2.3	**1**	**2.3**	**Si**
2.07	**1**	**2.07**	**Si**
2.3	**1.5**	**1.53**	**Si**
1.86	**1**	**1.86**	**Si**
1.1	**1**	**1**	**SiO_2**
1.1	**1.5**	**0.73**	**SiO_2**
1.1	**2**	**0.55**	**Pt**

4.3 Results and Discussion

4.3.1 Simulation

The result of finite element simulations, as shown in figure 4.1, shows that simply supported structures provide higher deflections than fully clamped structures. The Si/PZT thickness ratios of 1.0 and 2.07 were examined it was found that as the total thickness increases the system compliance decreases, which is also shown in figure 4.1.

Because of the boundary condition simulation results, an electrode coverage study was conducted in which a simply supported boundary condition was used. In order to harvest the optimal amount of charge from the flexing membrane, the effect of changing

the percent electrode coverage for the 3 mm square membrane was investigated. Utilizing finite element simulations, a trend of increasing output voltage as the percent electrode coverage decreases was determined, as shown in figure 4.2.

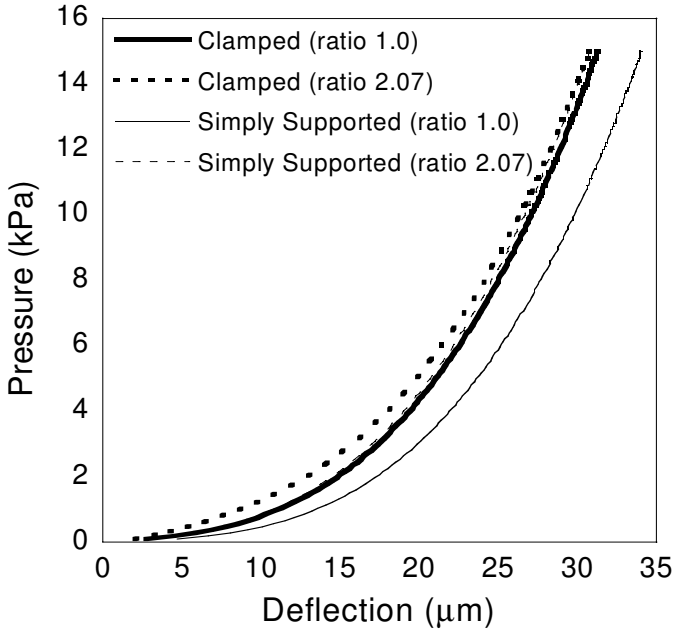

Figure 4.1: Comparison of simulated fully clamped and simply supported boundary condition pressure deflection curves for Si/PZT thickness ratios of 1.0 and 2.07.

It should be noted that in comparison with experimentation results, the electrode in the simulation is only located on the membrane and does not have the electrical lead, which is created for electrical contact while the membrane is in motion during experiments. Comparison between the experimental results and simulation do not match for percent electrode coverage of less than 40%. The reason for this is that the contribution of the electrical lead becomes significant as the electrode coverage decreases. Experimentally

this effect is hidden because the electrical lead is always present; however simulations do not require the lead for data collection purposes.

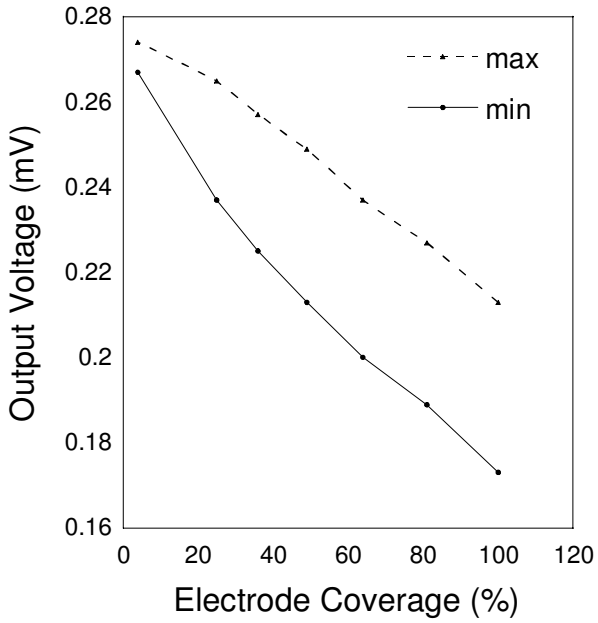

Figure 4.2: Comparison of the simulated simply supported output voltage vs. electrode coverage. The dashed curve provides the maximum voltage found by simulation and the solid line indicates the minimum voltage found for all of the Si/PZT thickness ratios that were investigated.

The effect of varying the thickness ratio on the coupling coefficient was also examined. The finite element simulations provided by the model developed by Xu utilized the properties in (7) to (9) to calculate k^2, where the electrical work, W_e, depends on the voltage, resistance, and time, while the mechanical work, W_m, depends on the pressure and the voltage.

$$k = \sqrt{\frac{W_e}{W_m}} \tag{7}$$

$$W_e = \sum_{t=0}^{250} \frac{V^2}{R} \cdot t \tag{8}$$

$$W_m = \sum_{cycle} P \cdot dV \tag{9}$$

These simulations revealed that as the PZT thickness increased in comparison to the silicon thickness, the coupling coefficient increases as well.

The finite element simulations provided by the model created by Al-Hattamleh, which incorporate the residual stress of the membrane, are shown in figure 4.3. The side length of the membrane was varied and the resulting coupling coefficient was determined for Si/PZT ratios of 1 and 2 as well as residual stresses of 10 and 100 MPa. These simulations determined that the coupling coefficient should decrease as the membrane side length increases for each of these situations. The dots in figure 4.3 are experimental data for 4, 5, and 8 mm side length membranes. The data and the simulations correlate very well. The residual stresses of each of the membranes also corresponds to the decreasing trend of the coupling coefficient, where the 4, 5, and 8 mm membranes had residual stresses of 60, 10, and less than 10 MPa.

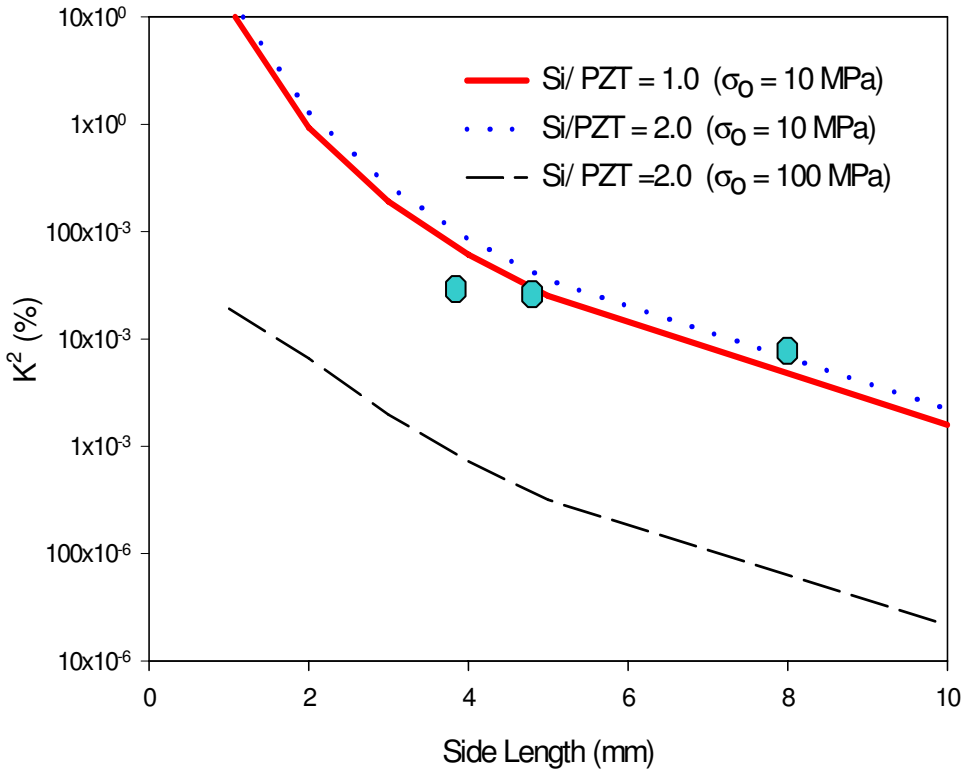

Figure 4.3: Effect of side length on electromechanical coupling coefficient.

4.3.2 Experiment

4.3.2.1 Adding Tungsten

Static bulge testing was utilized to directly measure the deflection of the membranes for given applied pressures. Figure 4.4 shows the measured data for a membrane with added tungsten and one without compared to simulation.

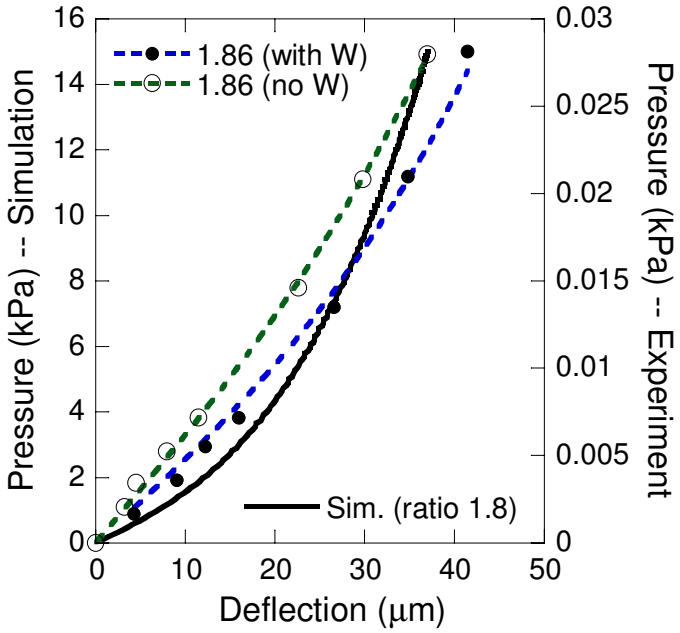

Figure 4.4: Comparison of simulation and experiment of pressure vs. deflection relationships for a Si/PZT thickness ratio of 1.86.

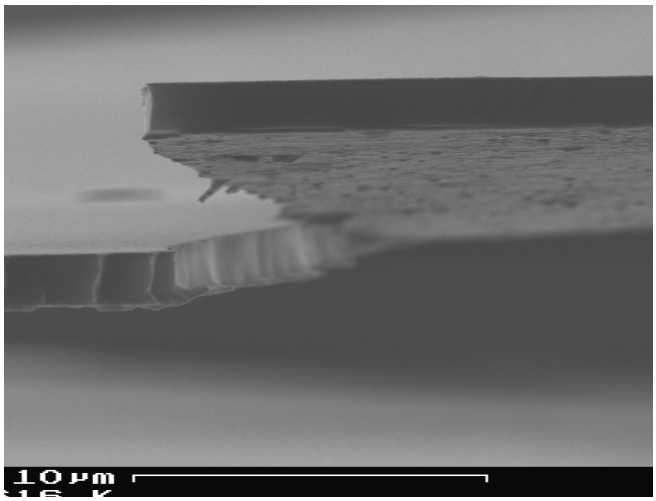

Figure 4.5: FESEM image shows the curvature of a membrane due to the tensile stresses accumulated during processing.

Figure 4.4 shows that the experiment data are stiffer at low pressures than the simulation provides. This is due to the fact that the simulation did not incorporate the residual stresses that dominate in the low pressure regime. Figure 4.5 shows an FESEM image of the effective curvature of the membrane after fracture, which is a result of the tensile stresses (the portion of the image on the right is bowing out of the plane of the remainder of the membrane). The technique of adding a compressive tungsten layer was utilized to experimentally lower the effective residual stress and create a more mechanically compliant membrane. The membranes were then bulge tested again to reveal, as shown in figure 4.4, an increase in the membrane deflection by approximately 17%.

The coupling coefficient was examined by electrically exciting membranes with an impedance analyzer. This method provided frequency vs. deflection data that was simulated utilizing the equivalent circuit for the composite structure, which enables the components of the equivalent circuit to be determined [18]. The coupling coefficient using this method is given by

$$k^2 = \frac{C_m}{C_o + C_m} \tag{10}$$

where C_m is the mechanical capacitance and C_o is the stationary capacitance. In comparison with the coupling coefficient, the stiffness coefficient is defined by [13],

$$k_s = \frac{dF}{d\delta} \tag{11}$$

in which F is the force that is calculated from a pressure vs. deflection curve and δ is the deflection of the curve. From [18],

$$k_s \propto \frac{1}{C_m} \tag{12}$$

Note also that k_s is directly related to the tensile residual stress because it is the initial portion of the pressure vs. deflection curve. Because of the large volume of the material in the experiment that is not excited during the test and the high residual stresses, the capacitance of the entire system, including the electrical leads, is much larger than the mechanical capacitance of the system.

In order to decrease the stiffness of the system, thereby increasing k^2, a tungsten layer was sputtered onto the bottom of the electrode support structure. This layer had a compressive stress of about 1 GPa, which effectively lowered the residual stress of each membrane. Table 4.2 shows the effects of applying a tungsten layer to five different membranes in terms of a change in residual tensile stress and resonant frequency. The effective change in stiffness correlates to an increase in k^2 by a factor of 2.

Table 4.2: Comparison of residual stress and resonant frequency changes for standard membranes and membranes with added tungsten.

	Average composite tensile residual stress (MPa)	Resonant Frequency (kHz)
PZT membranes	123	26.8
PZT membranes with compressive W layer	80	17.7

For the various Si/PZT ratios there were no clear trends shown, as a result of adding a compressively stressed film. It is only when the average stresses are measured from each membrane that the effectiveness of adding the compressive layer is clearly noted, as shown in Table 4.2. This is likely because the total thickness of the system

changes with the Si and PZT thicknesses. Therefore, there are some situations (thin Si, thin PZT) that would be more effected by the addition of a compressively stressed film than others (thick Si, thick PZT).

4.3.2.2 Trenching

The layers that constitute the standard 3 mm membranes are fully connected to the surrounding substrate, which is also known as fully clamped. During mechanical or electrical actuation of these membranes, the residual stress inherent to the membranes must be overcome before the membrane can fully deflect. Etching a trench around the membrane should approach a simply supported boundary condition. A simply supported boundary condition is defined as the condition that allows for the connected membrane edges to act as a hinge. With this type of boundary condition, more deflection occurs for a given pressure than in the case of a clamped boundary condition. Figure 4.6 shows a schematic of the resulting cross section of a membrane that has been trenched.

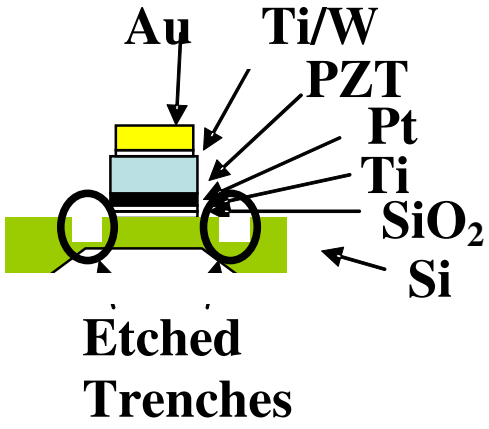

Figure 4.6: Simply supported boundary condition approached with HNA etch into the silicon substrate.

The trench was created by etching through the silicon substrate with a wet etchant HNA, which is a mixture of hydrofluoric, nitric, and acetic acids. Trenches formed in experiment were actually much shallower than shown in the schematic, but the schematic reveals how the trench slightly overlaps the membrane. Figure 4.7 shows a 3 mm membrane that has a trench overlapping the membrane. The addition of a trench around a 1.5 mm membrane increased the compliance of the membrane and as a result decreased the residual stress by 30%.

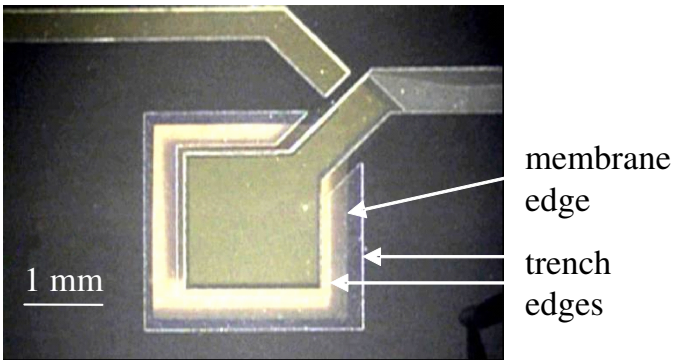

Figure 4.7: One-corner electrode configuration with trench for a 3 mm membrane.

4.3.2.3 Electrode Configuration

In addition to adding a compressive layer of tungsten to the composite membrane and trenching, experiments reveal that the configuration of the electrode that sandwiches the PZT layer also affects the membrane behavior. Typically, the Pt, PZT, and Au layers are connected at each corner of the square membrane creating what is referred to as the standard configuration, but in order to make the trenching more continuous around the membrane a few changes were incorporated. The first change was to introduce what is

referred to as a two-corner connected electrode configuration. This type of electrode configuration has two opposite corner connections etched so that the bottom electrode and top electrode extend off opposite corners. Figure 4.8 shows the two-corner configuration with a trench introduced.

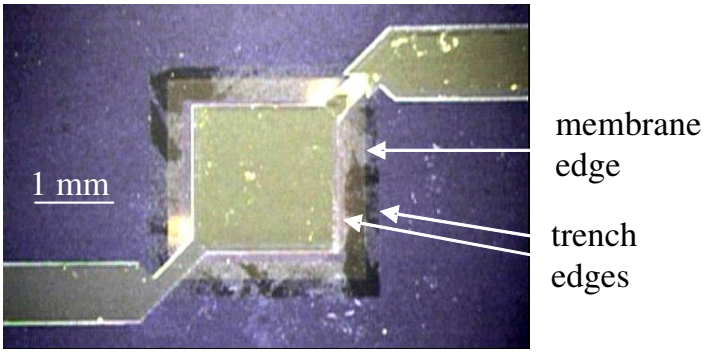

Figure 4.8: Two-corner electrode configuration with a trench.

The second type of electrode configuration change took this idea a step further by removing one more connection that produces what is called a one-corner electrode configuration. In this type of configuration both electrodes extend off the same corner and the PZT is utilized to insulate between them to ensure good electrical connection. Figure 4.7 shows the one-corner electrode configuration with the trench edges indicated.

Each of the three electrode configurations were tested before and after trenching utilizing the static bulge tester to obtain the pressure vs. deflection curves that are shown in figure 4.9. Comparison of the three electrode configurations before trenching reveals that the residual stress of the composite membrane incrementally decreases from the standard to the two-corner and further with the one-corner configuration. The total

reduction of the residual stress was 38% when a one-corner electrode configuration was used compared to the standard. With the trench introduced in the one-corner and two-corner configuration, indicated by the 57 and 55 second etch times in figure 4.9 respectively, the residual stress was reduced by another 16% in the case of the one-corner configuration.

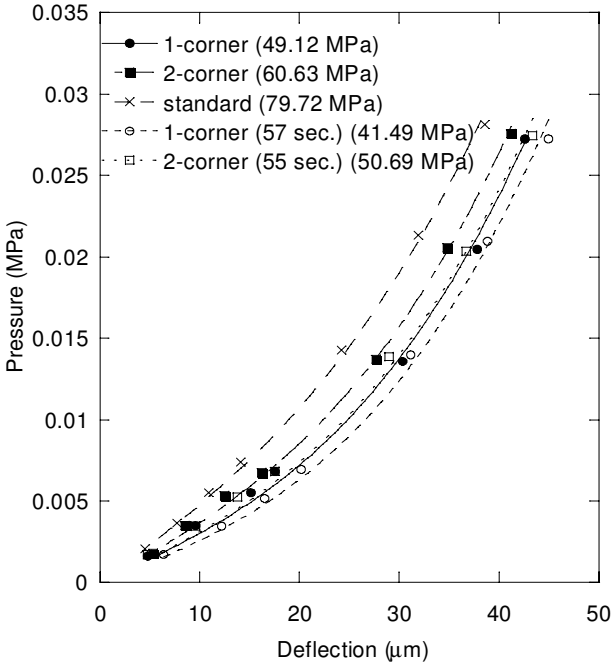

Figure 4.9: Comparison of each electrode configuration change with and without trenching.

4.3.2.4 Thickened SiO_2

Another method to reduce the stiffness is to increase the compressive silicon oxide thickness to compensate for the high tensile stresses that accumulate during processing. In the calculations, measured values of the elastic modulus and residual

stress for each layer were used. The thickness of each layer was: Si = 2.2 µm, SiO_2 = variable, Ti = 5 nm, Pt = 175 nm, 40:60 PZT = 1 µm, Ti/W = 12.5 nm, and Au = 75 nm. A calculated silicon oxide thickness of 1.5 µm was determined to balance the stresses in the composite structure. Figure 4.10 shows a finished membrane that was fabricated based on these calculations that has a thickened oxide. The membrane is slightly bulged due to over compensation of the tensile stresses leaving it compressive after processing.

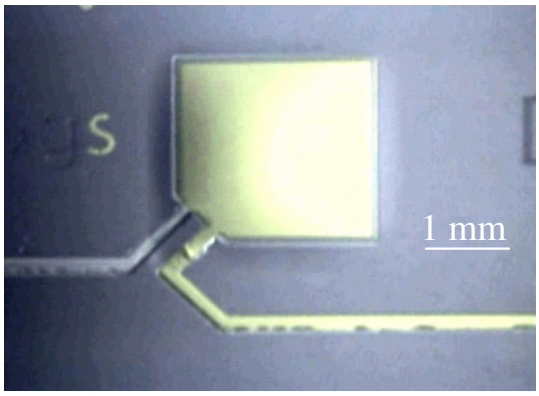

Figure 4.10: Slightly buckled membrane due to over compensation of the accumulated tensile stresses within the composite membrane.

Measurements were conducted on membranes such as the example shown in figure 4.10 for the coupling coefficient, the residual stress of the composite, and the resonant frequency. A laser vibrometer was used to measure a resonant frequency of 7.5 kHz, which is a decrease of 75% compared to standard membranes with 27 kHz. The residual stress was found to be 11 MPa, which is an overall decrease of 90% over standard membranes. The coupling coefficient was measured with an impedance analyzer, from

which it was determined that an improvement of 330% was obtained with a thickened silicon oxide and a one-corner electrode configuration.

4.4 Conclusions

For improved piezoelectric membrane performance, the effective residual stress of the composite structure must be reduced. A route has been shown that has reduced the overall effective residual stress by 90%. Growing a thick silicon oxide, incorporating a one-corner electrode configuration, and introducing a trench all work toward obtaining a lowered stress, but incorporating these fabrication changes together will create a piezoelectric membrane with nearly balanced stresses. With balanced stresses, the membrane performance improves towards optimal conditions for maximum output from the piezoelectric layer.

References

[1] M.S. Kennedy, D.F. Bahr, C.D. Richards, R.F. Richards, "*Residual Stress Control to Optimize PZT MEMS Performance*," Materials Research Society Proceedings **741** (2003) J5.37.1-J5.37.6.

[2] P. Muralt, A. Kholkin, M. Kohli, T. Maeder, N. Setter, "*Characterization of PZT thin films for micromotors*," Microelectronic Engineering **29** (1995) p. 67-70.

[3] L. Vergara, M. Clement, E. Iborra, A. Sanz-Hervas, J. Gacia Lopez, Y. Morilla, J. Sangrador, M. Respaldiza, "*Influence of oxygen and argon on the crystal quality and piezoelectric response of AlN sputtered thin films*," Diamond and Related Materials **13** 4-8 (2003) p. 839-842.

[4] C. Johnson, J. Ruud, R. Bruce, D. Wortman, "*Relationships between residual stress, microstructure and mechanical properties of electron beam-physical vapor deposition thermal barrier coatings*," Surface and Coatings Technology **108-109** (1998) p. 80-85.

[5] N. Ledermann, P. Muralt, J. Baborowski, S. Gentil, K. Mukati, M. Cantoni, A. Seifert, N. Setter, "*{100}-Textured, piezoelectric $Pb(Zr_x, Ti_{1-x})O_3$ thin films for MEMS: integration, deposition and properties*," Sensors and Actuators A **105** (2003) p. 162.

[6] R.W. Whatmore, Q. Zhang, Z. Huang, R.A. Dorey, "*Ferroelectric thin and thick films for microsystems*," Mater. Sci. in Semiconductor Processing **5** (2003) p. 65.

[7] L. Lian, N.R. Sottos, "*Effects of thickness on the piezoelectric and dielectric properties of lead zirconate titanate thin films*," J. Appl. Phys. **87** (2000) p. 3941.

[8] J.F. Shepard Jr, P.J. Moses, S. Trolier-McKinstry, "*The wafer flexure technique for the determination of the transverse piezoelectric coefficient (d_{33}) of PZT thin films*," Sensors and Actuators A **71** (1998) p. 133-138.

[9] C. Xu, T.S. Fiez, K. Mayaram, "*A nonlinear finite element analysis of a piezoelectric laminate*," Journal of Microelectromechanical Systems **12** (2003) p. 649.

[10] O. Al-Hattamleh, J. Cho, R. Richards, D. Bahr, C. Richards, "*The effect of design and process parameters on electromechanical coupling for a thin-film PZT membrane*," Journal of Microelectromechanical Systems **15** (2006) p. 1715-1725.

[11] M.J. Madou, Fundamentals of Microfabrication, CRC Press LLC (2002) p. 553.

[12] A. Degen, N. Abedinov, T. Gotszalk, E. Sossna, M. Kratzenberg, I.W. Rangelow, "*Stress analysis in Si membranes for open stencil masks and mini-reticles using double bulging and resonance methods*," Microelectronic Engineering **57-58** (2001) p. 425-432.

[13] S. Whalen, M. Thompson, D.F. Bahr, C.D. Richards, R.F. Richards, "*Design, fabrication and testing of the P^3 micro heat engine*," Sensors and Actuators A **104** (2003) p. 290-298.

[14] O. Crabtree, "*A numerical study of nonlinear static and dynamic behavior of a square thin plate membrane structure for application to a MEMS micro-generator*," Masters thesis, Washington State University (2004).

[15] M.S. Kennedy, A.L. Olson, J. C. Raupp, N. R. Moody , D.F. Bahr, "*Coupling bulge testing and nanoindentation to characterize material properties of bulk micromachined structures*," Microsystem Technologies **11** (2005) p. 298-302.

[16] L.M.R. Eakins, B.W. Olson, C.D. Richards, R.F. Richards, D.F. Bahr, "*Microstructural characterization and mechanical reliability of interfaces in piezoelectric based microelectromechanical systems*," Thin Solid Films **441** (2003) p. 180.

[17] P.D. Hayenga, "*Fabrication methods to improve performance of a piezoelectric membrane generator*," Masters Thesis, Washington State University (2005).

[18] Standards Committee of the IEEE Ultrasonics, Ferroelectrics, and Frequency Control Society, "IEEE Standard on Piezoelectricity," ANSI/IEEE Std. **176** (1987) p. 9-52.

CHAPTER FIVE

GOLD BOTTOM ELECTRODE

Piezoelectric materials are utilized for their ability to produce a charge when strained in applications such as sensors [1], actuators [2], and micropower generators [3]. Lead zirconate titanate (PZT), a piezoelectric ceramic, has been integrated into several ferroelectric devices that require a large switching charge and a small coercive field [4]. Typically PZT is suitable for small capacitors due to its ability to exhibit a large switching charge, but it also demonstrates a coercive field that is higher than that of strontium bismuth tantalum (SBT), which meets the size requirements necessary for low voltage operation. The discussion that follows in this paper reveals that PZT is an attractive piezoelectric ceramic because it crystallizes at a lower processing temperature than competing piezoelectric materials such as SBT and bismuth lanthanum titanium (BLT).

Several devices such as FeRAM, DRAM, VLSI, accelerometers [5], and micromotors [6] require a structure that consists of thin metal layers sandwiching the piezoelectric material in the fashion of a capacitor, in order to store the charge produced by the piezoelectric material [7, 8]. Platinum has been utilized as the bottom electrode metal because it can withstand the high temperature (often >600 ºC) processing required to crystallize the piezoelectric material [8]. It has been found that Pt shows poor fatigue properties for PZT capacitors with Pt electrodes [9]. However, Pt is difficult to pattern and etch accurately to sub-µm feature dimensions [8]. In order to overcome these drawbacks, conductive oxides such as RuO_2 and Pt-Ir oxides have become attractive substitutes for Pt. These oxides are attractive because they exhibit low resistivity at room

temperature, act as good diffusion barriers, and can be patterned with greater precision than Pt. Despite these improvements over Pt, a drawback to these oxides is that they exhibit leakage currents that often exceed limitations of VLSI and non-volatile memory devices. The main drawback, however, is that these oxides are costly to fabricate and the fabrication process is complex. RuO_2 exhibits metallic behavior only in its single crystalline form that is obtained by DC Magnetron sputtering with Ar + O_2 plasma onto a sapphire substrate [8]. Pt-Ir oxides are created by RF sputtering with Pt-Ir alloy targets with Ir chips set on the target [9]. Platinum has been utilized as an electrode material in accelerometer and micromotor devices because it is not necessary to pattern to sub-μm feature dimensions. However, the high tensile stress of Pt after heat treatment is the major drawback to using Pt in accelerometers and micromotors. Many methods have been utilized in an attempt to circumvent this limitation and effectively improve device performance [10, 11]. In order to overcome the limitations of Pt, fabricate thin metal layers for capacitor based devices in a cost effective manner, and improve performance properties; in this study gold has been integrated as a bottom electrode material. A discussion follows that will describe how PZT was successfully solution deposited onto a gold bottom electrode and tested for structural morphology and piezoelectric properties in comparison to PZT/Pt/SiO_2/Si structures.

5.1 Experiment

Typical fabrication for a piezoelectric element on a thin silicon support membrane with a patterned platinum bottom electrode using a lift-off technique consists of 15 process steps. Beginning with a boron doped silicon wafer, a 120 nm thick SiO_2 layer

was grown on it by a low temperature oxide growth process and patterned for lift-off processing of the Pt bottom electrode. A 175 nm Pt layer was DC Magnetron sputtered onto an adhesion layer. Attractive adhesion layers are Ti, Zr and Ta [12, 13]. For these experiments a 12 nm layer of Ti was used due to reports that Pt grain boundaries may allow for Ti diffusion so that PZT nucleation occurs with columnar microstructure orientation [14]. After lifting off the Pt in an acetone bath, the bottom electrode was annealed at 650 °C for 10 minutes in a furnace for the purpose of increasing the platinum grain size for improved PZT adhesion [15]. A sacrificial 150 nm Au layer was DC Magnetron sputtered onto the platinum bottom electrode side of the sample, in order to ensure that the PZT does not react with the SiO_2 layer, and later removed from the platinum using a gold etchant. An acetic acid based solution of lead zirconate titanate (HoAc-PZT) was deposited onto the Pt/sacrificial Au layer in several steps [16, 17, 18]. The HoAc-PZT has a molarity ratio of Zr to Ti of 40:60. The first layer is spun at 3000 rpm for 30 seconds and then placed onto a 350 ℃ hotplate for 1 minute. This step is repeated for a total of three layers. The sample is then crystallized in a rapid thermal annealer (RTA) for 30 seconds at 650 °C. This process of HoAc-PZT deposition was repeated until the desired thickness of PZT was obtained. The PZT film was patterned using standard photolithography and wet etching in a solution that consists of approximately 0.1 vol% hydrofluoric acid, 2.5 vol% hydrochloric acid, and 97.4 vol% DI water [19]. The sacrificial gold was etched, followed by deposition of a 300 nm gold top electrode that was DC Magnetron sputtered onto an adhesion layer of 5 nm Ti/W. This top electrode was photolithographically patterned and etched using a wet etchant. The backside of the sample was patterned for defining membrane structures and then etched

in a heated bath of potassium hydroxide (KOH) solution to define the silicon support, resulting in membranes with an active piezoelectric layer. A schematic is provided in figure 5.1 that compares the fabrication process for an Au vs. a Pt bottom electrode.

Using a gold bottom electrode to define the same piezoelectric membrane structure reduces the processing steps from 15 to 10. Using a substrate of boron doped Si/SiO_2, a 300 nm gold layer was DC Magnetron sputtered with an adhesion layer of Ti/W. The adhesion layer thickness varied between 5-20 nm, in order to determine the best design that produces films that are free from defects. The bottom electrode was annealed at 650 ºC for 10 minutes. The HoAc-PZT was solution deposited onto the bottom electrode as described previously, but layer deposition sequences of (3x3x3), (2x2x3x2), and (2x3x4) were used that correspond to each Ti/W layer thickness, as shown in Table 5.1. The HoAc-PZT was then patterned to expose probe access points to the bottom electrode. A 300 nm gold top electrode with a 5 nm Ti/W adhesion layer was DC Magnetron sputtered onto the HoAc-PZT and patterned. The membranes were then formed utilizing the same KOH etching procedure previously described. Replacing the platinum bottom electrode with a gold bottom electrode reduces the number of processing steps, which makes the total process more economical and faster.

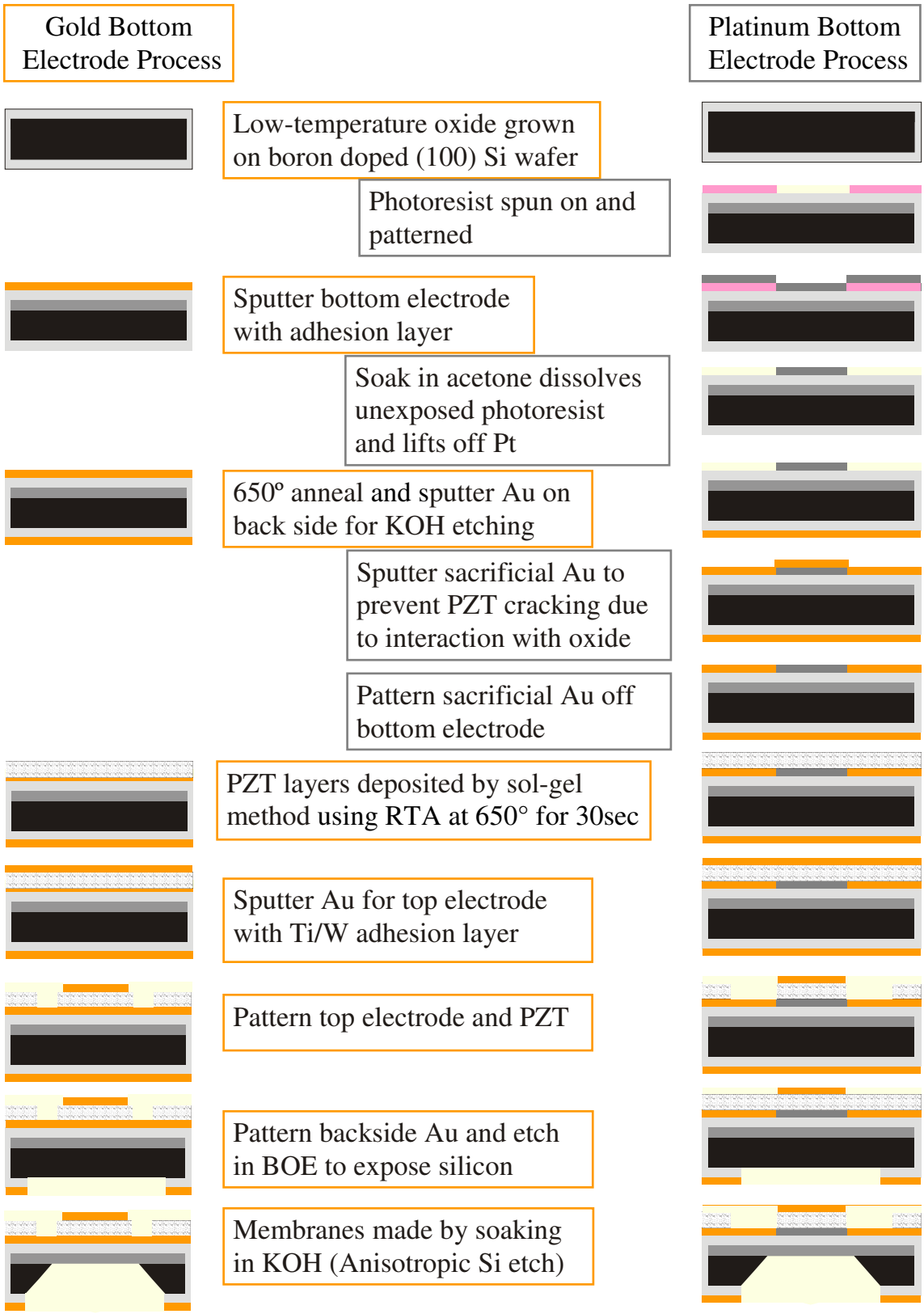

Figure 5.1: Comparison of the processes for Au or Pt as the bottom electrode material.

Table 5.1: Summary of adhesion layer thicknesses, PZT deposition sequences, and structural results.

Ti/W Thickness (nm)	PZT Sequence	Structural Result
5	3,3,3	Cracking in 3rd layer
10	3	Cracking in 3rd layer
20	3,3,3	Cracking in 3rd layer
20	2,3,4	Cracking in 9th layer
20	2,2,3,2	No Cracking

5.2 Results and Discussion

5.2.1 Structural Characterization

5.2.1.1 Cracking

During HoAc-PZT deposition, cracking initiated during the heat treatment process. The optical microscope images in figure 5.2 show that as the Ti/W adhesion layer thickens, the crack density decreases across a three inch wafer.

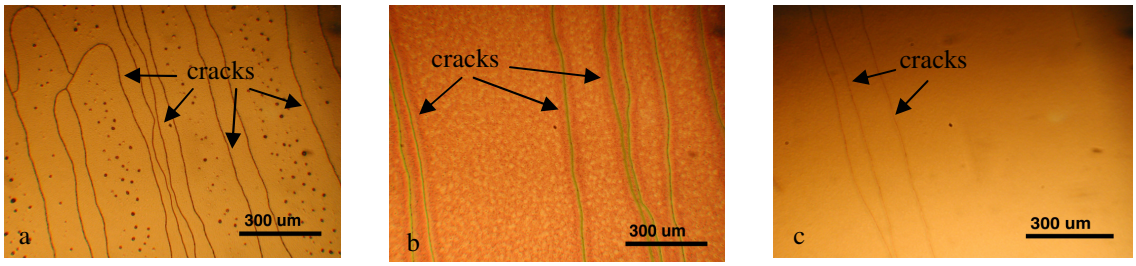

Figure 5.2: Optical microscope images of typical cracking across 3 inch wafer with Ti/W adhesion layer thicknesses of a) 5 nm, b) 10 nm, and c) 20 nm. As the adhesion layer thickness increases, the crack density decreases across the wafer.

The SEM micrographs of figure 5.3 show (a) a top view and (b) a cross sectional view of a crack that has gone through three pyrolosis steps and a single crystallization heat treatment. The top view reveals that the grains of the gold bottom electrode are well defined and have increased in size compared to the as sputtered grain size, while the cross sectional view shows that the gold grains have been extruded into the space between the edges of the crack. The crack edges in the top view also reveal that the PZT was sheared apart as evidenced by edges which match morphologically across the fracture. The cracks in this study initiated in the third pyrolosis heat treatment step. Elongation and spreading of the crack was induced by further heat treatment during crystallization in the RTA.

Two possible reasons for these fractures are the elastic strain energy which occurs due to the mismatch of thermal expansion coefficient and subsequent densification of the glass phase, and the formation of second phases due to interdiffusion between the substrate and piezoelectric films. The strain energy due to thermal expansion mismatch between the film and substrate will increase linearly with the thickness of the film, and the energy in a given crystallization step will be minimized by decreasing the film thickness. However, the amount of lead loss with each heat treatment through evaporation of PbO will increase, further altering the chemistry of the film. The PZT deposition sequence was therefore changed, as shown in Table 1, in an attempt to minimize the total the strain energy while minimizing the amount of lead loss. The results in Table 5.1 show that PZT deposition with a sequence of (2x2x3x2) provides a crack free ceramic film.

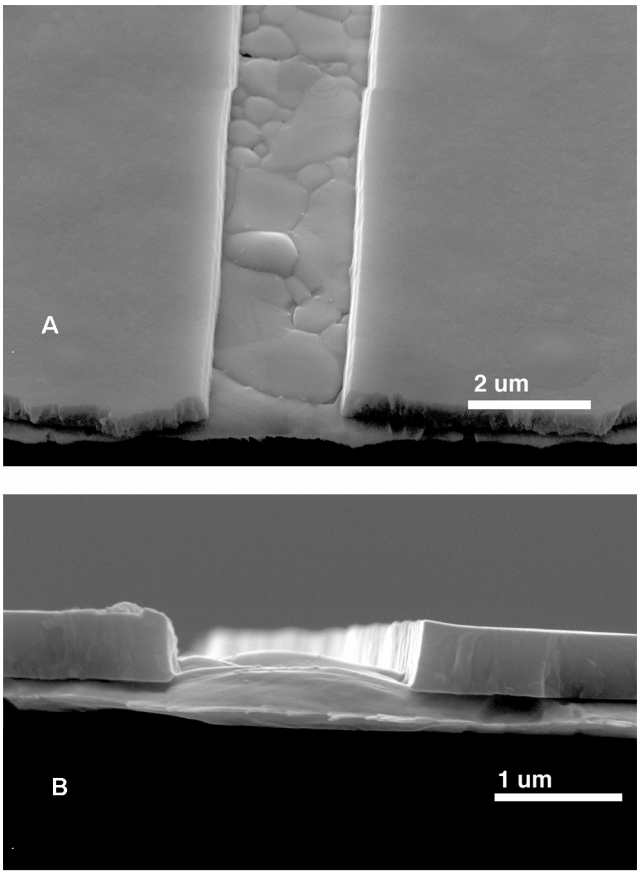

Figure 5.3: SEM micrographs of a) top view of crack and b) cross sectional view of the same crack.

Another mechanism that may lead to cracking in PZT thin films is a poor diffusion barrier that leads to the formation of lead silicides. A suitable diffusion barrier prevents lead from diffusing through the bottom electrode material so that it cannot interact with the SiO_2 substrate. The Ti/W adhesion layer acts as a diffusion barrier in this case and, therefore, if silicides were indeed forming, a thicker adhesion layer may help eliminate the cracks. Table 5.1 shows that utilizing a 10 nm or a 20 nm Ti/W adhesion layer results in a crack free PZT film. In order to investigate the diffusion of the interfaces within the composite, XPS was utilized to examine the chemistry of the bottom

electrodes on crack free samples which had undergone all three heat treatment steps at 650 °C. Figure 5.4 reveals that the W region slightly decreases in atomic concentration when subjected to the heat treatments involved in PZT processing.

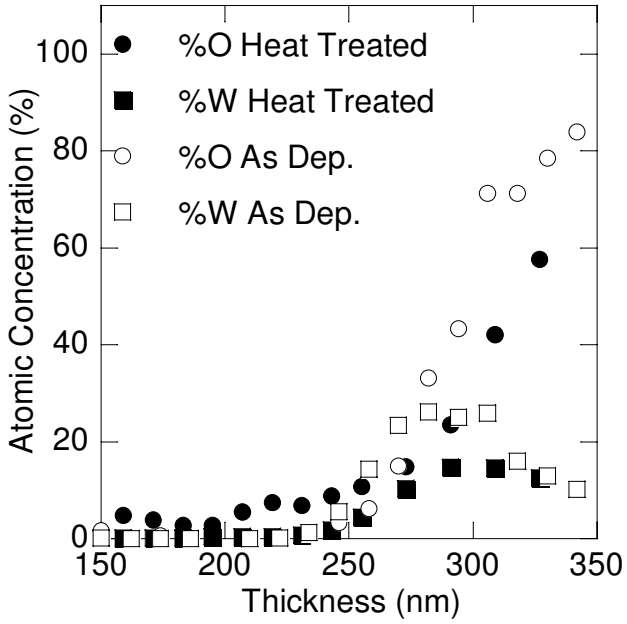

Figure 5.4: W composition comparison of as deposited and heat treated films.

Figure 5.5 shows how the concentration of gold in the sample decreases at a slower rate compared to another sample that did not go through the heat treatment process. This indicates that the Ti/W/gold interface region broadens with heat treatments. Since the Au portion of the Ti/W/gold region broadened, while the Ti/W region did not, the oxygen atomic concentration was examined. It was found that there is a shift in the amount of oxygen that corresponds to the shift in the gold. XPS also revealed that the components in the deposited PZT do not diffuse through the gold bottom electrode and Ti/W adhesion layer to induce cracking, so the Ti/W acts as a good diffusion barrier

between the underlying glass and the bottom electrode, and hence it is reasonable to conclude the cracking is controlled by the strain energy balance between the HoAc-PZT and the gold bottom electrode, and not the formation of any second phases.

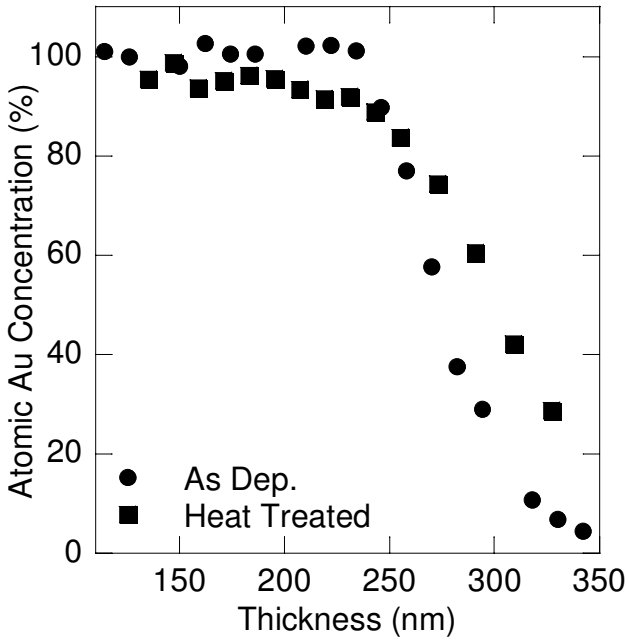

Figure 5.5: Au composition at the substrate/film interface for as deposited and heat treated films.

5.2.1.2 Morphology

The membranes with a gold bottom electrode were examined with an SEM, in order to directly compare the grain structure of the PZT on gold compared to the structure of PZT on platinum. Figure 5.6 reveals that the grain structure of the PZT is columnar in each case. It is also apparent that the voids present in the PZT grown on platinum are not present in the case of the PZT grown on gold. The voids are due to lead loss during the crystallization of the HoAc-PZT [15]. The effect of these voids on the properties of the

PZT is unclear, but a comparison of the PZT properties grown on platinum versus gold with be discussed in the next section of this paper. The overall morphology of the HoAc-PZT on gold is similar to that produced on platinum with columnar grains that are on the order of 100 nm in diameter.

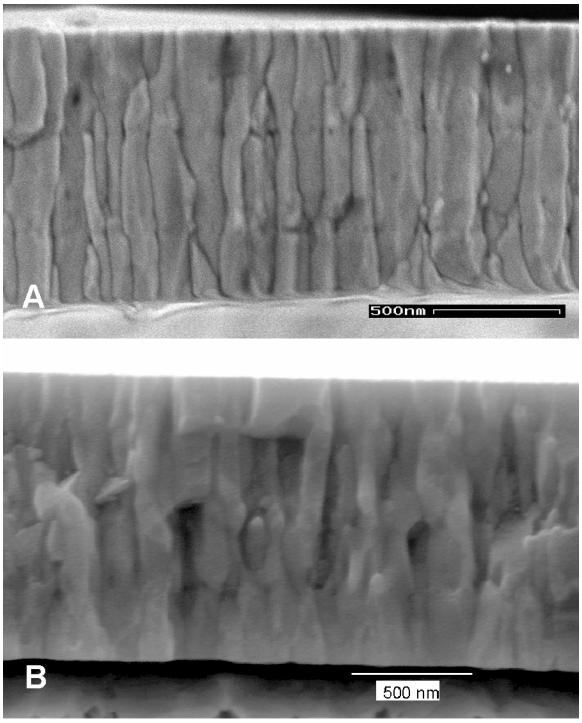

Figure 5.6: Comparison of PZT columnar grain structure on a) Platinum and b) Gold.

5.2.2 Properties

5.2.2.1 Piezoelectric

Crack free membranes were fabricated and tested for piezoelectric properties and compared to piezoelectric properties established for membranes with a platinum bottom electrode. In order to determine the piezoelectric coefficient, rectangular membranes

were formed to measure the transverse piezoelectric coefficient [20]. Figure 5.7 shows a schematic of the experimental setup.

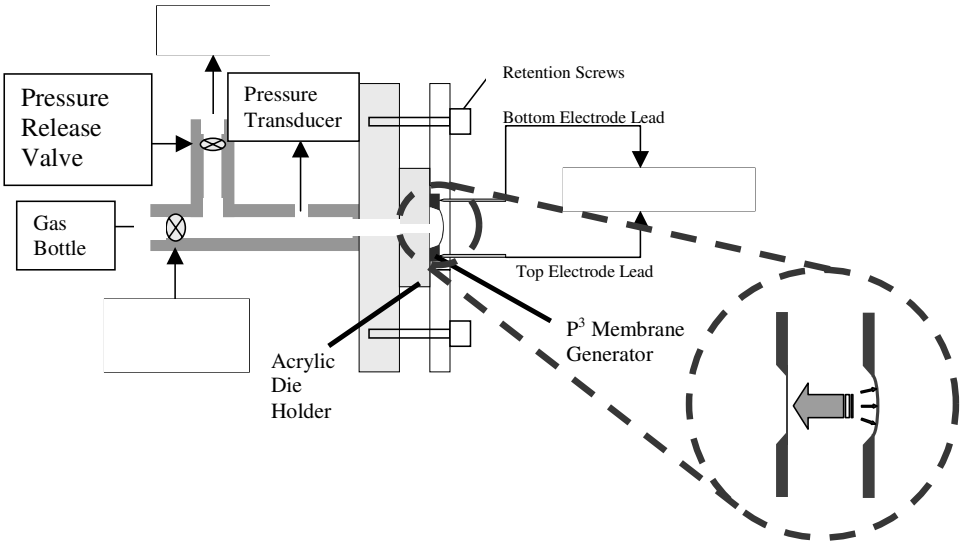

Figure 5.7: Rectangular Membrane Method (RMM) schematic of experiment setup.

The rectangular membranes had dimensions of 2x8 mm that effectively imposes a uniaxial strain for simplified calculation of the strain based piezoelectric coefficient, e_{31}. The strain within a deflected rectangular membrane is given by [21],

$$\varepsilon = \varepsilon_0 + \frac{a^2 + h^2}{2ah}\arcsin\left(\frac{2ah}{a^2 + h^2}\right) - 1 \qquad (1)$$

where ε, ε_0, a, and h are the strain, residual plane strain within the film, half the membrane width, and the center deflection of the membrane. Using one dimensional geometry simplifies the ability to measure this property on a thin film which is usually tested in a biaxial condition [22]. In this study, pressure is applied to the membrane and an integrated charge circuit measures the charge produced for that pressure. A laser

vibrometer simultaneously measures a change in displacement. The piezoelectric coefficient is then calculated with,

$$e_{31} = \frac{Q}{Ak_1} \tag{2}$$

where the variables Q, A, and k_1 are the measured charge, area of the electrode that is centered on the membrane, and the uniaxial strain. The average e_{31} found with the RMM test for 7-9 membranes with 1 μm of HoAc-PZT was -5.31 C/m^2 with a standard deviation of ± 0.15 C/m^2. This piezoelectric property was also measured for 9-12 membranes with 2 μm of HoAc-PZT and the average e_{31} was -5.43 ± 0.18 C/m^2. These values are comparable to e_{31} measurement results that were made with the same technique for rectangular membranes with a platinum bottom electrode, as shown in Table 5.2.

Table 5.2: Summary of bottom electrode materials used and the corresponding PZT thicknesses, dielectric constants for these films, and transverse piezoelectric constants.

bottom electrode material	PZT thickness (μm)	k (200 Hz)	e_{31} (C/m^2)
Pt	1	850	-5.5
Au	1	814	-5.31 ± 0.15
Au	2	814	-5.43 ± 0.18

The relative dielectric constant was determined to be 814 with an impedance analyzer at a frequency of 200 Hz for membranes with a gold bottom electrode. In comparison, the dielectric constant found for a membrane with a platinum bottom electrode was 850 at 200 Hz. The dielectric constant is calculated using,

$$k = \frac{Cd}{A}, \tag{3}$$

where k, C, d, and A are the dielectric constant, the capacitance of the membrane, the distance between the electrodes, and the area of the electrode, respectively. Increasing the PZT thickness did not change the dielectric constant. In summary, the membranes with a gold bottom electrode show comparable piezoelectric coefficients and dielectric constants as compared to PZT films formed on Pt electrodes. Both values are approximately 4% lower with the Au electrode, but these values are similar to the range of experimental variation, as summarized in Table 5.2.

5.2.2.2 Pressure – Deflection Behavior

In order to determine the pressure-deflection behavior of the crack free piezoelectric films, square membranes were fabricated and tested. Each membrane was clamped and a laser vibrometer was positioned on the top electrode that is centered on the membrane. The laser vibrometer was utilized to measure the displacement of the membrane at specific applied pressures of 0.25-3.5 psi. Figure 5.8 reveals a comparison of the pressure-deflection curves found for membranes with a gold or platinum bottom electrode.

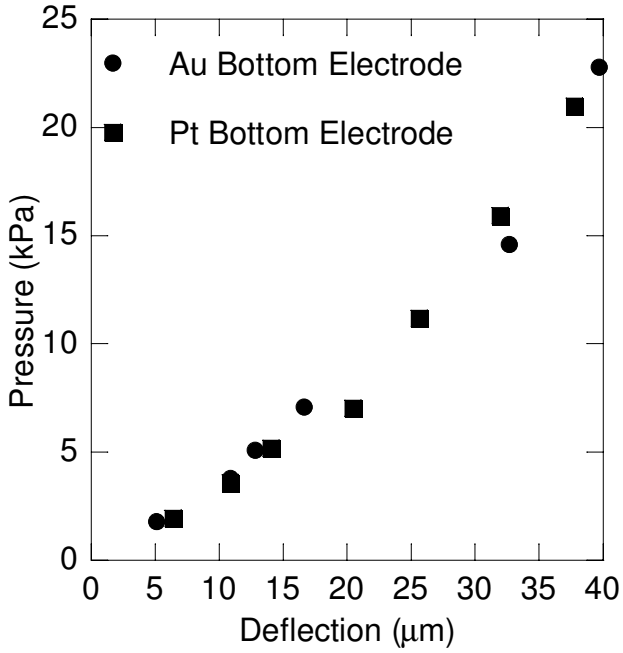

Figure 5.8: Pressure deflection relationship for PZT coated membranes with gold vs. platinum bottom electrode.

The pressure-deflection data was fitted with a model described by Bonnotte *et al.*,

$$P(W_0) = E_B \frac{t^3 W_0}{(0.015)a^4} + \frac{(3.4)\sigma_0 t W_0}{a^2} + \frac{(1.82)E_B t W_0^3}{a^4} \qquad (4)$$

in which E_B, t, W_0, a, and σ are the composite biaxial modulus, total thickness, membrane deflection, half the membrane side length, and the effective residual stress of the composite membrane, respectively [23]. A thickness weighted biaxial modulus for each membrane was determined to be 161 GPa and 183 GPa for gold and platinum bottom electrodes, respectively. The pressure-deflection curves in figure 6.8 reveal that the behavior of the square membranes is comparable for each bottom electrode. Utilizing equation (4), the effective residual stress for a composite membrane with a gold bottom

electrode is 50 MPa, while for a composite membrane with a platinum bottom electrode it is 55 MPa.

5.2.2.3 Resonant Frequency

An impedance analyzer was used to determine the resonant frequency of each square membrane. A frequency sweep was used to electrically excite a membrane and a resonant frequency of 22.1 kHz was determined for membranes with a gold bottom electrode and 1 μm of HoAc-PZT. The typical resonant frequency of a membrane with a platinum bottom electrode with the same thickness of HoAc-PZT is 24.5 kHz. Thus, substituting gold for the platinum bottom electrode allows the composite membrane to perform comparably when electrically excited.

5.2.2.4 Reliability

A fatigue test was conducted that incorporated a square membrane with a gold bottom electrode in order to establish the integrity of the composite structure when operating as a piezoelectric sensor. The piezoelectric coefficient was initially measured for the membrane. Then the membrane was mechanically deflected at 240 Hz to a total strain of .0193%. After 1,000,000 cycles, the membrane was retested for its piezoelectric coefficient. A 3% change in e_{31} was identified. This amount of change falls within the standard deviation of a typical e_{31} measurement. Therefore, the piezoelectric performance of a composite membrane with a gold bottom electrode does not degrade over the range of conditions used in this type of mechanical cycling.

5.3 Conclusions

A process for depositing piezoelectric thin films on gold bottom electrodes through a solution deposition technique, which reduces the number of processing steps needed to fabricate piezoelectric MEMS structures, has been described. The morphology of the grain structure of PZT on gold, which has columnar grains with diameters on the order of 100 nm, is similar to that formed on platinum, with no evidence of voids forming at the crystallization steps. Cracking in the PZT films appears to be driven by differences in thermal expansion coefficient, and not via formation of silicide phases. The piezoelectric and dielectric properties of the PZT films are comparable to those formed on platinum bottom electrodes. The PZT film on gold does not exhibit any significant properties degradation after mechanical cycling for one million cycles.

References

[1] R. Ali, D. Roy Mahapatra, S. Gopalakakrishnan, "*An analytical model of costrained piezoelectric thin film sensors*," Sensors and Actuators A **116** (2004) p. 424.

[2] P. Muralt, A. Kholkin, M. Kohli, T. Maeder, "*Piezoelectric actuation of PZT thin film diaphragms at static and resonant conditions*," Sensors and Actuators A **53** (1996) p. 398.

[3] S. Whalen, M. Thompson, D. Bahr, C. Richards, R. Richards, "*Design, fabrication and testing of the P3 micro heat engine*," Sensors and Actuators A **104** (2003) p. 290.

[4] Y. Arimoto, H. Ishiwara, "*Current status of ferroelectric random-access memory*," Materials Research Society Bulletin **29** 11 (2004) p. 823.

[5] H.Yu, L. Zou, K. Deng, R. Wolf, S. Tadigadapa, S. Trolier-McKinstry, "*Lead zirconate titanate MEMS accelerometer using interdigitated electrodes*," Sensors and Actuators A **107** (2003) p. 26.

[6] P. Muralt, A. Kholkin, M. Kohli, T. Maeder, N. Setter, "*Characterization of PZT thin films for micromotors*," Microelectronic Engineering **29** (1995) p. 67.

[7] E. Defay, C. Millon, C. Malhaire, D. Barbier, "*PZT thin films integration for the realization of a high sensitivity pressure microsensor based on a vibrating membrane*," Sensors and Actuators A **99** (2002) p. 64.

[8] K. Takemura, T. Sakuma, Y. Miyasaka, "*High dielectric constant (Ba, Sr)TiO_3 thin films prepared on RuO_2/sapphire*," Applied Physics Letters **64** 22 (1994) p. 2967.

[9] K. Kuribayashi, Y. Fujita, H. Isige, T. Iwanuma, "*Sputter deposited Pt-Ir oxides thin films and their characterization*," Materials Science and Engineering B **109** (2004) p. 188.

[10] M.C. Robinson, P.D. Hayenga, J.H. Cho, C.D. Richards, R.F. Richards, D.F. Bahr, "*Fabrication methods for improved electromechanical behavior in piezoelectric membranes*," Materials Research Society Symposium Proceedings **872** (2005) J18.26.

[11] P.D. Hayenga, "*Fabrication methods to improve performance of a piezoelectric membrane generator*," Masters Thesis, Washington State University (2005).

[12] I. Meyyappan, A.P. Malshe, H.A. Naseem, W.D. Brown, "*Au/(Ti-W) and Au/Cr metallization of chemically vapor-deposited diamond substrates for multichip module applications*," Thin Solid Films **253** (1994) p. 407.

[13] R.J. Miller, A. Gangulee, "*Electromigration in gold and copper thin film conductors*," Thin Solid Films **69** (1980) p. 379.

[14] G.J. Willems, D.J. Wouters, H.E. Maes, "*Influence of the Pt electrode on the properties of sol-gel PZT films*," Microelectronic Engineering **29** (1995) p. 217.

[15] L.M.R. Eakins, B.W. Olson, C.D. Richards, R.F. Richards, D.F. Bahr, "*Influence of structure and chemistry on piezoelectric properties of lead zirconate titanate in a microelectromechanical systems power generation application*," Journal of Materials Research **18** (2003) p. 2079.

[16] W. I. Lee, J. K. Lee, Materials Research Bulletin **30** (1995) p. 1185.

[17] G. Yi, Z. Wu, M. Sayer, "*Preparation of Pb(Zr,Ti)O_3 thin films by sol gel processing: Electrical, optical, and electro-optic properties*," Journal of Applied Physics **64** (1988) p. 2717.

[18] J.V. Martinez, "*Fabrication, materials, and characterization for efficient MEMS power generation*," Masters Thesis, Washington State University (2004).

[19] B.W. Olson, "*Optimization of a piezoelectric membrane generator*," Masters Thesis, Washington State University (2002).

[20] T.M. Sullivan, "*Development of a Novel method for measuring the Transverse Piezoelectric Coefficients of Thin Piezoelectric Films*," Masters Thesis, Washington State University (2004).

[21] Y. Xiang, X. Chen, J.J. Vlassak, "*Plane-strain bulge test for thin films*," Journal of Materials Research **20** 9 (2005) p. 2360.

[22] J.F. Shepard Jr., P.J. Moses, S. Trolier-McKinstry, "*The wafer flexure technique for the determination of the transverse piezoelectric coefficient (d_{33}) of PZT thin films,"* Sensors and Actuators A **71** (1998) p. 133.

[23] E. Bonnotte, P. Delobelle, L. Bornier, "*Two interferometric methods for the mechanical characterization of thin films by bulging tests. Application to single crystal silicon*," Journal of Materials Research **12** 9 (1997) p. 2234.

CHAPTER SIX

STRAIN AT FAILURE

The design of micromachined piezoelectric membranes is typically specific to the type of microelectromechanical system (MEMS). One performance parameter that is important to understand for these applications is the amount of strain that a membrane can withstand before failure. On the macro scale, tensile tests and three and four point bending are typically used to characterize the fracture strength of materials. However, the micro scale provides limitations to this type of testing because of the dimensions and the difficulties in accurately measuring the applied pressures and displacements. Therefore, bulge testing and beam element bending have been utilized because of the ability for optical methods to measure the deflections achieved in the experiments. One study investigated 36 polysilicon diaphragms to failure using applied pressure to perform a bulge test, and it was found that the available mean strain at failure was 1.7%, with a standard deviation of 0.34% [1]. Other research groups have investigated the mechanisms that influence the fracture strength of a variety of MEMS structures, where the range of strain at failure extends from 0.45% to 5.8% [2, 3, 4, 5]. These studies include ultrananocrystalline Si and Si_3N_4 by bulge testing at the low end, boron doped Si achieved by bending beam elements in the mid range, and pure bulk Si beam fracture by bending at the upper end of the range. A bulk PZT fracture study showed that 260 μm PZT withstood up to 0.06% strain when subjected to 40 MPa applied stress. The fracture in this study was found to be influenced by both the applied electric field and the applied mechanical stress, although the electric field effect was minimal compared to the applied

level of stress [6]. In comparison, the mechanisms that influence the strain at failure for micromachined membranes containing piezoelectric elements have been studied far less thoroughly. In one study, strains of 0.1% to 0.2% caused failure for 3 mm membranes tested with bulge testing [7]. These MEMS structures had a 1.5 µm thick piezoelectric element and silicon support structures that were 1.5 to 3 µm thick.

This chapter will provide a discussion of the results for a parametric study that investigated the strain at failure for different types of piezoelectric composite membranes. Several structural aspects were examined including the type of PZT chemistry, the volume of the membrane, the membrane side length, the volume of PZT subjected to strain, the type of bottom electrode material, and the amount of residual stress in the composite membrane. In addition, a quantitative study of microcracking was conducted, in order to determine if the presence of the microcracking affected the strain at failure. Experiments were also conducted in which the applied pressure direction to the membrane was investigated, in order to define which produces the highest strain at failure.

6.1 Experiment Procedure

6.1.1 Membrane Fabrication

Square membranes were bulk micromachined from a composite structure that consisted of a thin film layer sequence of SiO_2/Ti/Pt/PZT/Ti/W/Au on a (100) Si wafer. In order to create this structure, SiO_2 was thermally grown to thicknesses of 110 nm and 1.5 µm from a 2.1 µm thick boron doped silicon substrate. A 175 nm thick platinum thin film was then DC magnetron sputtered onto the oxide after deposition of a 5 nm titanium

adhesion layer that oxidizes during subsequent processing [8]. A lead zirconate titanate (PZT) film that had a Zr:Ti ratio of 40:60 was solution deposited onto the Pt by spin coating. PZT chemistries of 2-methoxyethanol-based (2MOE) and acetic acid-based (HOAc) were created in a variety of thicknesses [9]. Typical PZT film solution deposition consisted of spinning 0.11 μm layers, each of which was pyrolized at 350 ºC for 1 minute. At each accumulation of 0.33 μm thickness a crystallization heat treatment at 650 ºC for 30 seconds was conducted using a rapid thermal annealer. This process was repeated until the desired PZT thickness was reached. A 300 nm thin film of Au was then DC magnetron sputtered onto the PZT film with a 12 nm adhesion layer of Ti/W. Contact photolithography was utilized to create the features on the top of the membrane. Ethylene diamine pyrocatechol (EDP), which is an anisotropic etchant, was then used to etch the silicon on the backside of the sample, in order to create square composite membranes with a total thickness that ranged from 3.7 μm to 5.8 μm and had lateral dimensions of 3, 4, 5, and 6 mm side lengths. After etching the membranes, the wafers were diced to isolate the individual membranes.

6.1.2 Testing Procedure

The membrane containing die were glued with *Crystal Bond 555* to an aluminum puck that has a 0.2 mm hole in the center. The hole enables the pressure to be applied to the membrane using a static bulge testing apparatus. A cast iron bellows was controlled manually to apply pressure to the cavity side (back side) of the membrane or to pull a vacuum so that the ambient air was effectively pressurizing the membrane from the top electrode side (front side) of the membrane. Figure 6.1 shows a cross sectional schematic

of a membrane with the applied pressure directions indicated and the corresponding nomenclature used for each direction.

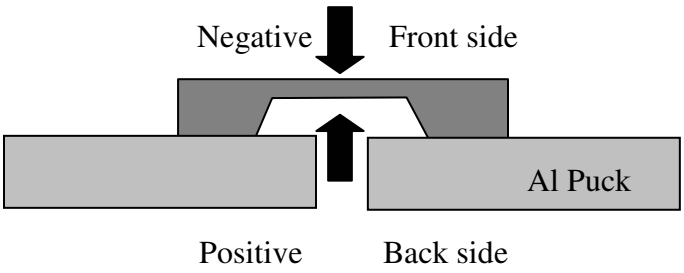

Figure 6.1: Cross section schematic of a membrane with applied pressure directions indicated and the corresponding nomenclature used for each direction.

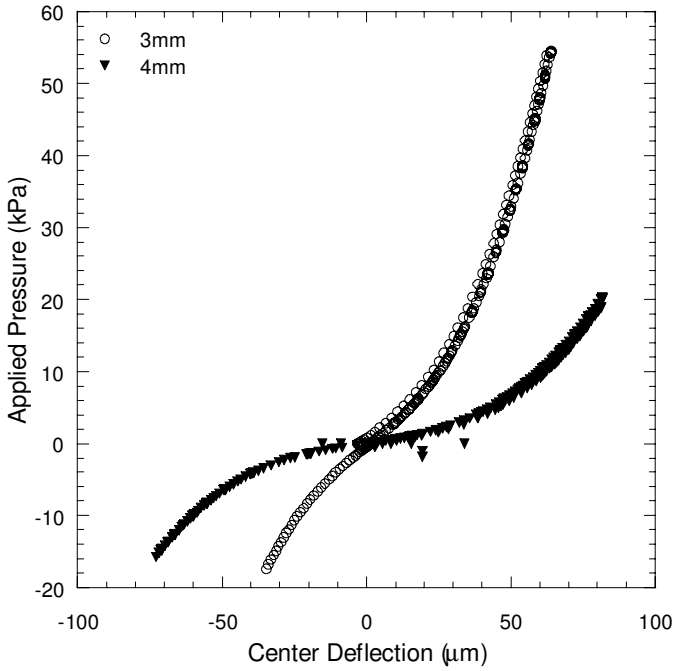

Figure 6.2: Typical pressure vs. deflection curves for 3 and 4 mm square PZT MEMS. Both the deflection and pressure extend over positive and negative values.

A laser vibrometer was aligned with the center of the membrane so that the incident light reflected directly back into the laser vibrometer sensor as the membrane deflects. The laser vibrometer was used to measure changes in the center deflection as the membrane was pressurized. A software program created with *LabView* recorded both the applied pressure and the center deflection of the membrane. Figure 6.2 shows typical pressure vs. deflection curves for a 3 and 4 mm membrane tested with this setup. The recorded pressures extend over both positive and negative values. There were between 20 and 30 membranes tested with this setup for the results that are presented in this chapter.

6.2 Results and Discussion

The surfaces of many of the PZT films were inspected by FESEM, in order to determine the surface microstructure. Membranes with 2MOE-based PZT chemistry revealed a clean surface that was free of any apparent defects. The HOAc-based films had pre-existing cracks that extend through the entire PZT thickness and were qualitatively similar to mud-flat cracking [10, 11]. Figure 6.3a reveals typical cracking that extends over the entire piezoelectric film surface of the HOAc-based PZT samples used in this study. It was determined by inspection of the PZT film that surrounds the membrane compared to the PZT film that covers the top of the membrane that the cracking is the same type and density in each case. Figure 6.3b shows that the crack extends through the entire PZT thickness. The cracks have a width of 110 to 130 nm. The cracks are narrow enough to not allow the Au top electrode to penetrate farther than a few 10s of nm into the PZT thickness that ranged from 1 to 3 μm.

a)

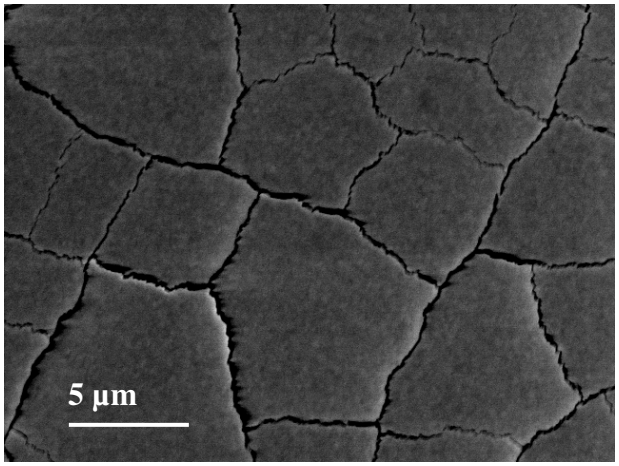

b)

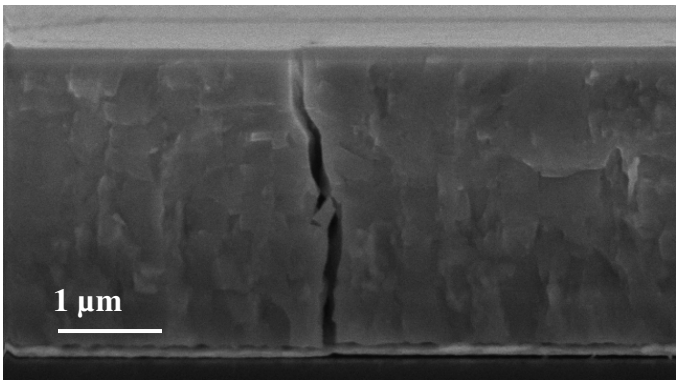

Figure 6.3: FESEM micrographs of the a) surface of a typical HOAc PZT film on a 3 mm membrane with significant cracking that extends over the entire sample and b) a crack that extends through the entire PZT film thickness.

The crack length per area is calculated by initially counting the number of crack intersections that are parallel and perpendicular to one side of a square section of cracked PZT surface [12].

Since the property of interest in this set of experiments was the strain at failure, each of the membranes had an increasing amount of pressure applied until the membrane fractured. In order to determine the strain at failure for each of the membranes tested, a

pressure vs. deflection curve was measured. The uniaxial strain, ε, at the center of the membrane is determined by [13],

$$\varepsilon = \frac{2}{3}\frac{\delta^2}{a^2} \tag{1}$$

where δ is the center deflection and a is half of the membrane side length.

6.2.1 Cracks in PZT films

An area of 54 µm x 31 µm within a compilation of crack images was selected for counting the number of cracks for each membrane that had HOAc-based PZT film. The crack length per area was calculated to be approximately the same in the region surrounding the membrane and directly on the membrane. Table 6.1 provides the crack length per area for the microcracking that was present as the residual stress of the membranes varied.

Table 6.1: Comparison of the crack length per area to the amount of residual stress within the 3, 4, and 5 mm composite membranes.

	Residual stress (MPa)	Crack length / area (mm/mm^2)
3mm	54	1275
4mm	59	868
	12	665
5mm	10	425

The residual stress and biaxial modulus were calculated from the curve fit for each pressure vs. deflection curve, by utilizing [14]

$$P(\delta) = E_B \frac{t^3\delta}{(.015)a^4} + \frac{(3.40)\sigma_0 t\delta}{a^2} + \frac{(1.82)E_B t\delta^3}{a^4} \tag{2}$$

where δ, E_B, t, a, and σ_0 are the deflection, biaxial modulus, membrane thickness, half the membrane side length, and the residual stress within the membrane, respectively. It is assumed that with fixed strain conditions between the layers in the composite, the amount of residual stress and the biaxial modulus are averages. In general, as the residual stress decreased, the crack length per area decreased. Therefore, the cracking across the PZT film was not reducing the amount of residual stress within the composite membrane.

6.2.2 Applied Pressure Direction

The 3, 4, and 5 mm bare silicon membranes that were created for these tests had 2.1 µm thick silicon and a native oxide. Other 3 mm membranes had 2.1 µm thick Si plus a 100 nm layer of SiO_2. Initially a vacuum was pulled on the membrane so that the membrane deflected into the cavity a certain amount and then the pressure was applied to the backside of the membrane, in order to deflect the membrane in the opposite direction to an amount equal that of the initial deflection. The applied pressure was then increased as the membrane reached a higher deflection into the cavity. For these tests the highest amount of pressure was always applied to the membrane in the negative regime first. The 4 and 5 mm composite membranes, which had a 2.1 µm thick Si layer and a 1.8 µm thick Si layer respectively, were examined in a similar manner. In addition to these layer thicknesses, each composite membrane had 175 nm Pt, 1 µm PZT, and 300 nm Au. The PZT and Au films were etched, as shown in figure 6.6a. For comparison, the experiment was conducted so that the pressure was applied to the back side, or positive pressure was applied, of the membrane first. Table 6.2 shows a comparison of the average strain at failure for each applied pressure direction (front side vs. back side) for each type of

membrane. The highest strain at failure of 0.49% was determined for a bare Si membrane when the pressure was applied to the back side of the membrane. The additional SiO_2 layer strengthens the membrane when the pressure is applied to the front side of the membrane, by approximately 50%. However, the additional SiO_2 layer weakens the membrane when the pressure is applied to the back side of the membrane compared to the bare Si membranes. The composite membrane has a higher strain at failure than the Si/SiO_2 membranes when the pressure is applied to the back side of the membrane, but does not reach the strength of the bare Si membranes.

Table 6.2: Comparison of the average strain at failure for membranes of different side lengths that have bare Si, Si/SiO_2, and composite structures.

	bare Si				**Si/SiO_2**		**composite**	
pressure direction	back	back	front	front	back	front	back	front
membrane side length	3mm	5mm	4mm	5mm	3mm	3mm	4mm	4mm
average strain at failure	0.45%	0.49%	0.07%	0.13%	0.17%	0.26%	0.3%	0.17%
standard deviation	0.02%	0	0.02%	0.09%	0.07%	0.06%	0.04%	0.04%

The composite membrane has a lower strain at failure than the Si/SiO_2 membranes that have the pressure applied to the front side, but the strain at failure for the composite is higher than that of the bare Si membranes.

Statistical Wilcoxon-Mann-Whitney Rank Sum Tests were performed on the strain at failure data. This type of statistical test is used when there are two sets of data that have unpaired amounts of data in each set. A P-value of greater than 0.05 indicates

that the samples are most likely from the same population. For example, with a P-value of 0.4, there is a 40% chance that the two sets of data are from the same population. A P-value of 0.02 indicates that there is a 2% chance that the two sets of data are from the same population, which is indicated by different in the result column of Table 6.3. Several different tests were conducted and the results are summarized in Table 6.3.

Table 6.3: Summary of the Wilcoxon-Mann-Whitney Rank Sum Tests performed on the strain at failure data sets.

Tests	P-value	Result
1) Bare Si 4mm front vs. Bare Si 5mm front	0.4	same
2) Bare Si 3mm back vs. Bare Si 5mm back	0.12	same
3) Bare Si front vs. Bare Si back	0.009	different
4) Si/SiO_2 front vs. Si/SiO_2 back	0.23	same
5) Composite front vs. Composite back	0.004	different
6) Bare Si front vs. Si/SiO_2 front	0.048	different
7) Bare Si back vs. Si/SiO_2 back	0.029	different
8) Si/SiO_2 front vs. Composite front	0.4	same
9) Si/SiO_2 back vs. Composite back	0.004	different
10) Bare Si front vs. Composite front	0.11	same
11) Bare Si back vs. Composite back	0.008	different

The statistical tests reveal several aspects of the strain at failure data that were unclear by just looking at the data. Since tests one and two are both from the same population, the side length of the membrane does not matter. Since tests three and five indicate that the data sets are from different populations, the applied pressure direction does matter for bare Si or the composite membrane structures. However, the applied pressure direction does not matter for Si/SiO_2 structures, as verified by test four. Tests six and seven reveal that adding the SiO_2 layer to the membrane structure influences the strain at failure. However, when the entire composite structure was compared to the Si/SiO_2 structure, it

was found that these types of membrane structure are from the same population, as shown by test eight. This indicates that adding PZT to the structure does not influence the strain at failure when the pressure is applied from the front side. This result was verified with test ten, in which case the bare Si membranes were compared with the composite membrane structures for the case when the pressure is applied to the front side. In contrast with this result, adding PZT to the Si/SiO_2 structure does influence the strain at failure when the pressure is applied from the back side, as revealed by test nine. Test eleven verifies this result, in which case the bare Si membranes were compared to the composite membrane structures for the case when the pressure is applied to the back side.

6.2.3 Materials in the Composite Membrane

Two types of PZT chemistry including 2MOE and HOAc and two types of bottom electrode material including Pt and Au were examined to determine which provided a higher strain at failure. The precursor chemistry of the PZT layer in the composite membrane is of particular interest because it is the piezoelectric material that produces charge when strained. The type of PZT will influence how much charge is produced by a particular membrane, but understanding how much the membrane can be strained before failure is critical to the performance of the membrane as well. Each of the composite 3 mm membranes had 110 nm SiO_2, 175 nm Pt, and 1 μm of PZT. Four 2MOE membranes and three HOAc membranes were tested to failure. Table 6.4 shows that the average strain at failure for the 2MOE PZT chemistry is approximately 0.16% ± 0.03% and the HOAc PZT is 0.14% ± 0.02%.

Table 6.4: Comparison of the average strain at failure for membranes with PZT chemistries of 2MOE or HOAc and bottom electrode materials of Pt or Au.

PZT chemistry	2MOE	HOAc	HOAc	HOAc
bottom electrode	Pt	Pt	Pt	Au
membrane side length	3mm	3mm	4mm	4mm
average strain at failure	0.16%	0.14%	0.26%	0.25%
standard deviation	0.03%	0.02%	0.04%	0.03%

The bottom electrode material in the composite membrane undergoes several heat treatments during processing. The change in temperature during the heat treatment induces plastic flow and diffusion at the interfaces. Platinum and gold were examined because previous studies showed that the residual stress state of the composite membrane after heat treatment for either bottom electrode material is not significantly different and the PZT microstructure remains columnar for each case [15]. However, SEM images from that study reveal that the microstructure of the PZT deposited onto Pt had approximately 20 nm voids at the interface, while the microstructure of the PZT deposited onto Au did not show this type of defect. In order to determine the effect of the voids in the composite membrane on the integrity of the composite membrane, the strain at failure was studied for each bottom electrode material. The membranes examined for this part of the study were 4 mm membranes that had 110 nm SiO_2 and 1 μm of HOAc-based PZT. Three Au and two Pt bottom electrode membranes were tested. It was found that all of the membranes failed within a range of 0.23% to 0.28% strain.

Overall, the material used within the composite membrane, whether it is 2MOE or HOAc-based PZT or a bottom electrode made of Pt or Au, provides a strain at failure that

agrees with the level of strain at failure presented in Table 6.2 for membranes that had the pressure applied to the front side. In addition, the presence of voids or microcracks within the composite structure does not significantly influence the strain at failure. Therefore, changing the materials within the composite structure will not decrease the strength of the membrane.

6.2.4 Volume of PZT Subjected to Strain

The composite membrane accumulates residual stress during processing to levels of up to 90 MPa. In order to increase the compliance of the piezoelectric membrane, portions of the PZT were etched from the regions at the edge of the membrane. Figure 6.4 shows an example of the etched regions in the surrounding area of the membrane. The volumes of PZT etched off of the membranes included 37.5%, 56%, and 75%. Tests to failure were performed for five 4 mm, three 5 mm, and six 6 mm membranes. Each of these membranes had layer thicknesses of 110 nm SiO_2, 175 nm Pt, and 1 μm PZT. The pressure vs. deflection curves were fit with equation 2, from which the effective residual stress was calculated for each type of membrane. With the etched regions, the calculation should not be viewed as an exact value of residual stress, but a relative measure of compliance. The results of these calculations and the testing are shown in Table 6.5. Each of the 4 mm membranes had approximately the same amount of residual stress and the corresponding average strain at failure levels were approximately equal for each amount of etched PZT. Increasing the membrane side length to 5 mm decreased the amount of residual stress in half, but the average strain at failure remained at approximately the same level as the 4 mm membrane results.

(a)

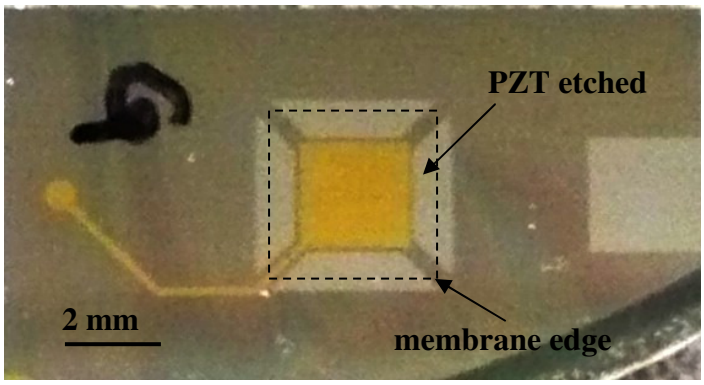

(b)

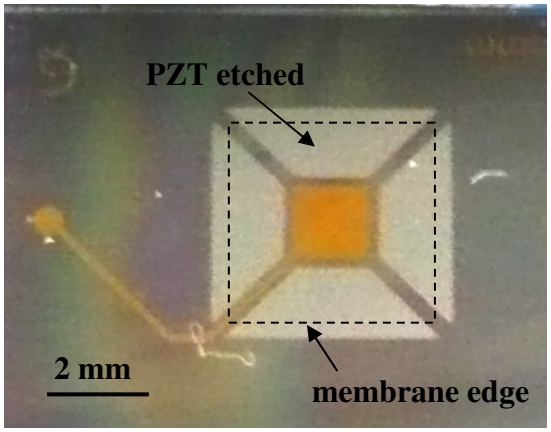

Figure 6.4: Optical images of two 4 mm membranes that have a) 37.5% of the PZT volume etched and b) 75% of the PZT volume etched from the samples. The dash lined square indicates the edges of the membrane.

When the membrane side length was increased further to 6 mm, the residual stress stayed relatively constant between for the membranes of this size and the PZT volume that was etched. However, despite the amount of PZT etched or the side length of the membrane, the average strain at failure levels remained unchanged.

Table 6.5: Comparison of the strain at failure and effective residual stress for different amounts of PZT volume and membrane side length.

PZT volume etched	4 mm ε_f	4 mm σ_r (MPa)	5 mm ε_f	5 mm σ_r (MPa)	6 mm ε_f	6 mm σ_r (MPa)
37.5%	0.26%	86	0.23%	40	NA	NA
56%	0.24%	89	0.33%	39	0.25%	68
75%	0.27%	85	NA	NA	0.26%	50

Therefore, the changes in the compliance provided by this type of structural change to the composite membrane do not decrease the strength of the composite membrane. This is most likely due to the amount of change in the residual stress in the composite membrane.

6.2.5 PZT Thickness Variation

Another type of structural change to the composite membrane that was investigated, in order to examine the effect of residual stress, was to change the thickness of the PZT layer. The 3 mm piezoelectric membranes that were fabricated consisted of 2.1 µm Si, 110 nm SiO_2, 175 nm Pt, and 300 nm Au, in which the PZT thickness was varied to include 1, 1.5, 2, and 2.9 µm thicknesses. Table 6.6 shows the average strain at failure and residual stress for each of the membranes. Each of the composite structures tested had approximately the same amount of residual stress. The level of residual stress is within the range that was found for the previously described volume variation that was provided by etching the PZT.

Table 6.6: Comparison of the average strain at failure and effective residual stress for each PZT thickness.

PZT thickness (μm)	Average ε_f	σ_r (MPa)
1.0	0.16%	56
1.5	0.22%	54
2.0	0.15%	55
2.9	0.22%	42

The PZT thickness variation provided very similar average strain at failures, which also fall in the range of the average strain at failure levels described in the previous section of this paper. Therefore, changing the PZT thickness does not cause a significant change in the overall strength of the membrane.

6.2.6 Increasing Support Layer Compliance

Two levels of effective residual stress including high (58 MPa) and low (10 MPa) were investigated, in order to examine the effect of increasing the compliance of the support layers within the composite structure on the level of the average strain at failure. In order to achieve these levels of effective residual stress, a compressively stressed SiO_2 layer with a thickness of 110 nm in the 4 mm composite membranes and 0.5 μm in the 5 mm composite membranes was used. The compressively stressed SiO_2 can be used to decrease the effective tensile residual stress that accumulates during processing in the composite. The other layers in the composite structures included 2.1 μm Si, 175 nm Pt, 2 μm PZT, and 300 nm Au in the 4 mm membrane, while the 5 mm membranes had 1.8 μm Si, 175 nm Pt, 2.9 μm PZT, and 300 nm Au. The 4 mm membrane had a PZT etch geometry that is shown in figure 6.4a, while the 5 mm membrane had a PZT etch geometry that is shown in figure 6.5.

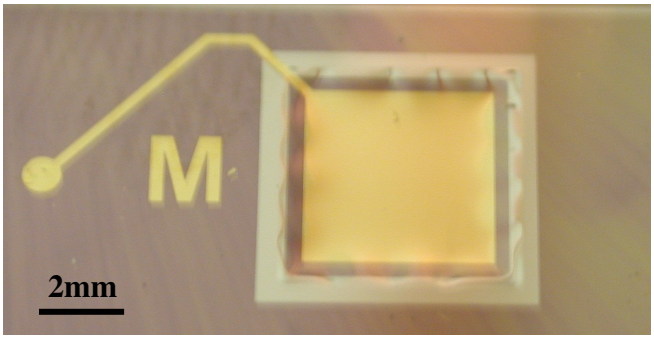

Figure 6.5: Optical image of a low stress 5 mm membrane that has a PZT etch pattern that extends around almost the entire membrane edge.

Each membrane tested was pressurized to failure. It was found that the average strain at failure for the membranes with effective residual stresses of 58 MPa was 0.19%, while the average strain for the low stress membranes was lower at 0.146%. The difference between the average strain at failure results is larger than the changes obtained with changes in layer thickness and etch pattern. However, increasing the compliance of the support layers actually decreased the strain at failure, which is the opposite effect desired. Therefore, the average strain at failure for composite membranes is influenced by the level of the effective residual stress, however the upper limit to the strains that can be achieved by these membrane structures is approximately 0.2%.

6.3 Conclusions

The average strain at failure was investigated for several micromachined membranes. Using a biaxial bulge testing system, the amount of microcracking decreased as the level of residual stress decreased in the composite membranes, which

suggests that the cracks are not acting to relieve residual stresses. The bare Si membranes provided the highest overall average strain at failure of 0.49%. Adding a SiO_2 layer to the Si decreased the strength of the membrane, but an average strain at failure of 0.26% ± 0.06% was provided when the pressure was applied to the front side of the membrane compared to the back side, which provided 0.17% ± 0.07%. In comparison to the Si/SiO_2 membrane, the composite membrane achieved higher levels of average strain at failure at 0.3% ± 0.04% in the case where the pressure was applied to the back side of the membrane. Statistical tests reveal that the membrane side length does not influence the strain at failure and that the applied pressure direction does impact the strain at failure in the case of bare Si and composite membranes with the membrane failing at lower strains when the pressure is applied to the front side as compared to the back side. These tests also show that adding SiO_2 to the bare Si membrane influences the strain at failure. This was also the case for adding PZT to the Si/SiO_2 structures when the pressure is applied from the back side of the membrane. It was found that material changes within the composite do not decrease the average strain at failure of the composite membranes. In addition, changing the composite membrane structure did not significantly change the average strain at failure. Increasing the SiO_2 thickness increased the compliance of the composite membrane by decreasing the amount of effective residual stress from 56 MPa to approximately 10 MPa. This type of change in residual stress, unfortunately decreased the strain at failure, which is the opposite effect from what was desired. Thus, the composite membrane structures studied have an upper limit to the amount of achievable strain of approximately 0.2%.

References

[1] S.C. Bromley, L.L. Howell, B.D. Jensen, "*Determination of maximum allowable strain for polysilicon micro-devices*," Engineering Failure Analysis **6** (1999) p. 27-41.

[2] F. Ericson, J-A. Schweitz, "*Micromechanical fracture strength of silicon*," Journal of Applied Physics **68** (1990) p. 5840-5844.

[3] N. Setter, R. Waser, "*Electroceramics materials*," Acta Materialia **48** (2000) p. 151–178.

[4] D.A. Hall, "*Nonlinearity in piezoelectric ceramics*," Journal of Material Science **36** (2001) p. 4575–4601.

[5] B. Peng, N. Pugno, H.D. Espinosa, "*An analysis of the membrane deflection experiment used in the investigation of mechanical properties of freestanding submicron thin films*," International Journal of Solids and Structures **43** (2006) p. 3292-3305.

[6] G.A. Schneider, F. Felten, R.M. McMeeking, "*The electrical potential difference across cracks in PZT measured by Kelvin Probe Microscopy and the implications for fracture*," Acta Materialia **51** (2003) p. 2235-2241.

[7] I. Demir, A.L. Olson, J.L. Skinner, C.D. Richards, R.F. Richards, D.F. Bahr, "*High strain behavior of composite thin film piezoelectric membranes*," Microelectronic Engineering **75** (2004) p. 12-23.

[8] L.M.R. Eakins, B.W. Olson, C.D. Richards, R.F. Richards, D.F. Bahr, "*Microstructural characterization and mechanical reliability of interfaces in piezoelectric based microelectromechanical systems*," Thin Solid Films **441** (2003) p. 180-186.

[9] L.M.R Eakins, B.W. Olson, C.D. Richards, R.F. Richards, D.F. Bahr, "*Influence of structure and chemistry on piezoelectric properties of lead zirconate titanate in a microelectromechanical systems power generation application*," Journal of Materials Research **18** (2003) p. 2079-2086.

[10] M.D. Thouless, "*Crack spacing in brittle films on elastic substrates*," J. Am. Ceram. Soc. **73** (1990) p. 2144-2146.

[11] H.B. Chew, T.F. Guo, L. Cheng, "*Vapor pressure and residual stress effects on failure of an adhesive film*," International Journal of Solids and Structures **42** (2005) p. 4795-4810.

[12] DeHoff, Rhines, Quantitative Microscopy, McGraw-Hill, New York, (1968).

[13] Y. Xiang, X. Chen, J.J. Vlassak, "*Plane-strain bulge test for thin films*," Journal of Materials Research **20** (2005) p. 2360-2370.

[14] E. Bonnotte, P. Delobelle, L. Bornier, "*Two interferometric methods for the mechanical characterization of thin films by bulging tests. Application to single crystal silicon*," Journal of Materials Research **12** (1997) p. 2234.

[15] M.C. Robinson, D.J. Morris, P.D. Hayenga, J.H. Cho, C.D. Richards, R.F. Richards, D.F. Bahr, "*Structural and electrical characterization of PZT on gold for micromachined piezoelectric membranes*," Applied Physics A (2006) DOI: 10.1007/s00339-00603674-1.

CHAPTER SEVEN

COUPLING COEFFICIENT

A variety of applications including micromotors, sensors, and micropumps are dependent on the amount of induced strain energy applied to a piezoelectric membrane [1, 2, 3, 4]. The core element of these devices is a thin film piezoelectric membrane. Piezoelectric materials such as lead zirconate titanate (PZT), zinc oxide, and aluminum nitride, show properties that can be exploited for these devices. In particular, the properties of d_{31} and e_{31} are the main focus. However, d_{31} is most appropriate for bulk ceramic applications, while thin film based piezoelectric applications often rely on e_{31} for performance characterization. Most of these applications function due to the deflection of a cantilever or membrane and only the transverse piezoelectric coefficient, e_{31}, can describe this phenomenon effectively [5]. Of the piezoelectric materials listed, PZT thin films have the durability to allow for increased applied force and output power compared to ZnO and AlN thin films [6].

Another key contributing factor to the performance of a piezoelectric membrane is the electromechanical coupling coefficient, commonly referred to as k^2. This coefficient is defined as the ratio of the electrical energy converted over the total input energy used to actuate the structure [7]. Analytical modeling has been conducted by Cho *et al.* that determined the relationship between the coupling coefficient and the residual stress for a membrane [8]. Several research groups report that lowering the amount of residual stress will directly improve the electromechanical coupling of a composite thin film membrane

[2, 9, 10]. Recent experiments have revealed that membranes with a low composite residual stress provide an electromechanical coupling coefficient that is orders of magnitude higher than membranes that have a high residual stress [11].

Literature provides a discussion of membranes that perform in either the low [12] or high strain regimes [13, 14]. However, most examples are concerned with the low strain regime due to specific application purposes. The low strain operating regime limits the membrane operation to plate-like or bending behavior, while the high strain regime extends the membrane operation to the stretching mode [15, 16, 17]. This chapter will describe a method to measure the electromechanical coupling behavior for thin film composite membranes operating in the stretching mode. The discussion includes a description of how the transverse piezoelectric coefficient, e_{31}, the modulus of the piezoelectric layer, and the dielectric coefficient influence this behavior. This chapter provides a discussion of predicting performance from piezoelectric membranes in terms of the membrane's electromechanical coupling coefficient.

7.1 Experiment Procedures

7.1.1 Membrane Preparation

The square piezoelectric membranes used in this study were micromachined from a composite structure. The substrate was a boron doped silicon wafer from which a SiO_2 layer was grown with a combination of dry and wet oxidation to comprise a 110 nm or a 0.5 μm SiO_2 thin film. Onto this surface an 18 nm Ti adhesion layer and a 175 nm thick Pt layer were deposited using DC magnetron sputtering. A PZT layer was deposited using solution deposition techniques [18]. A 110 nm layer of the PZT sol-gel

was deposited and then pyrolyzed at 350º for 1 min. This step was repeated three times. Crystallization was conducted in a HeatPulse 610 Rapid Thermal Annealer for every 330 nm, in which the temperature was ramped in 10 s to 650 ºC and held for 30 s then ramped down in 10 s. The sample was allowed to fully cool to room temperature for 5 additional minutes prior to further deposition. Piezoelectric films between 2 µm and 3.8 µm thick were deposited. A 300 nm Au with a 5 nm Ti/W adhesion layer was DC magnetron sputtered onto the PZT. The composite structure was then patterned with contact photolithography. Windows in the SiO_2 film were created on the back side of the wafer with a buffered oxide etch that will define diaphragm structures of lateral dimensions between 4 and 8 mm square. The Au and PZT were patterned so that the Au is utilized as the top electrode and the Pt can be utilized as the bottom electrode. The wafer was placed into an EDP solution that etches the silicon for approximately 6 hours to create the 1.8 to 2.1 µm thick boron doped silicon layer within the composite membranes. A finished 5 mm membrane is shown in figure 7.1.

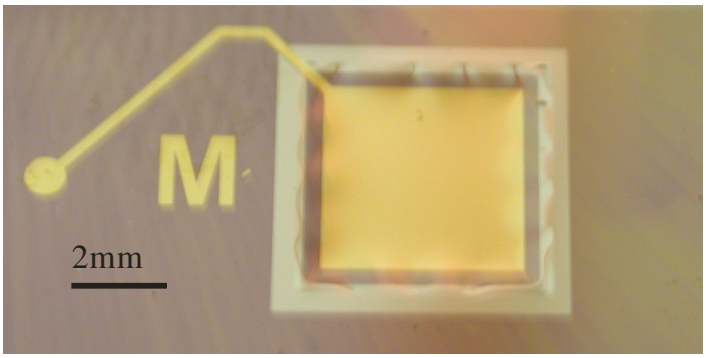

Figure 7.1: Membrane with patterned Au top electrode and PZT etched to reveal Pt along the edge of the membrane.

Membrane preparation continued with poling. Poling involves applying a field to the piezoelectric film by applying a voltage to the electrodes. The poling procedure consists of initially measuring the capacitance of the membrane to see if there are any shorts. Then a voltage is slowly incrementally applied, from zero to a peak voltage, held for 1 minute, and then slowly decreased to zero. In order to determine the applied field that aligns all of the dipoles within the piezoelectric film, the current across the membrane was measured simultaneously during the application of voltage to the membrane. Figure 7.2 shows the correlation between the applied voltage and the response in the current across the membrane.

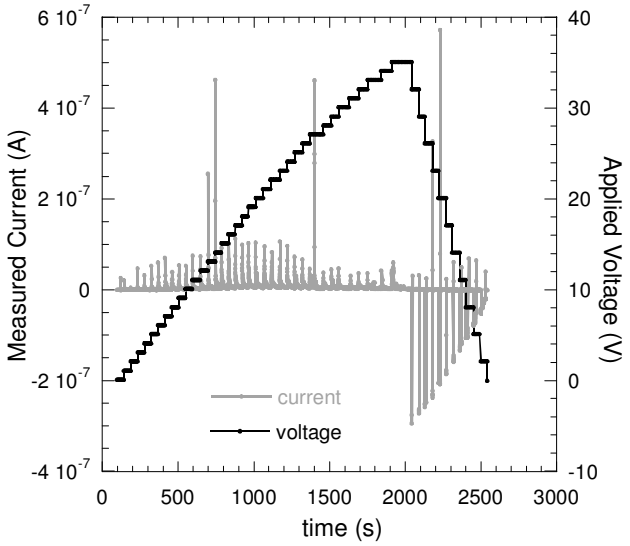

Figure 7.2: Voltage applied to 8 mm membrane while current was monitored.

The spikes in the current trace, when the voltage is applied, indicate that the dipoles within the PZT are aligning to the applied field direction, which is perpendicular to the electrodes. Figure 7.3 shows a zoomed in view of one of the current spikes.

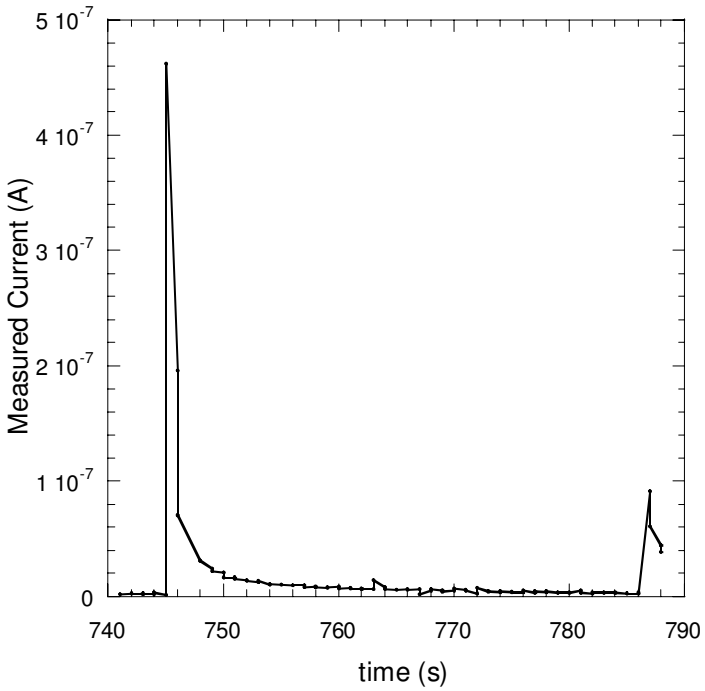

Figure 7.3: Zoomed in view of an individual current spike measured during poling.

The measured current is composed of the polarization current and the conduction current. The sharp peak in the current that is due to the alignment of the dipoles is dominated by the polarization current, which drops off exponentially to the level of the conduction current. Once all of the dipoles have aligned, the polarization current significantly drops and the total measured current remains low as the voltage is continuously increased. The current spikes that occur while the voltage is decreased are due to the flow of current to the voltage source, since the capacitive membrane is initially at a higher voltage than the voltage source at each decreasing step in voltage. Figure 7.2 indicates that this particular 3 μm film was fully poled with 27 V, which corresponds to 90 kV/cm. The applied field for the 4, 5, and 8 mm membranes was 12 V/μm, 10 V/μm, and 12 V/μm, respectively. This technique for determining the

applied field that should be used for poling does not always provide a clear decrease in the current trace. Ferroelectric testing was conducted to verify the saturation voltage of 3 µm PZT films. The saturation voltage corresponds to the applied field that is required to align the dipoles within the film. Figure 7.4 shows a typical test for a 5 mm membrane with this PZT film thickness.

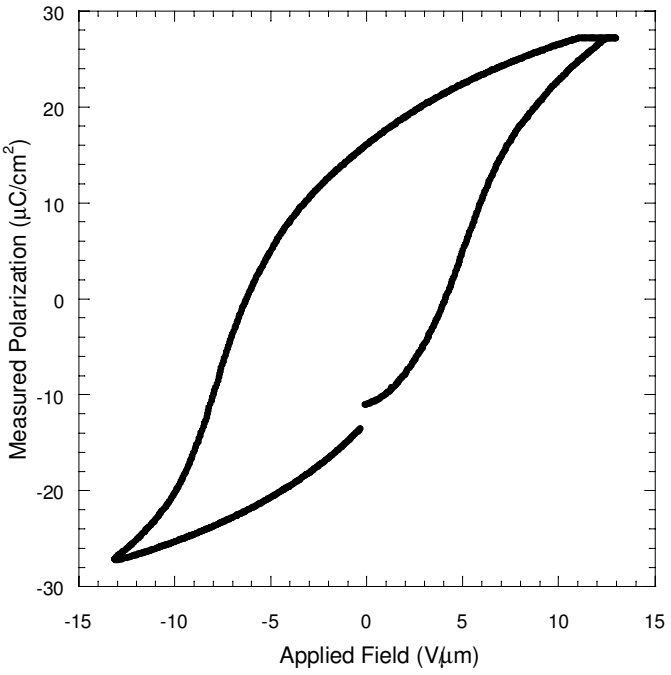

Figure 7.4: Ferroelectric test on 3 µm PZT film.

The saturation field for this film is 10 V/µm, which is very similar to the necessary applied field found by the current monitoring poling test described previously for a 5 mm membrane. Waiting 24 hours after poling provides piezoelectric properties that are reproducible, due to dipole relaxation within the initial hours after poling [19].

7.1.2 Testing Procedures

Square membranes were tested using a static deflection test. A membrane is glued to a puck and placed on a holder that is sealed while pressurized air is applied to the back side of the membrane. The pressure is cycled from zero pressure to a higher or lower pressure, which means that a positive or negative pressure is applied to the membrane, and then cycled back to zero pressure without any breaks in the application of pressure. In order to simultaneously measure the deflection, a laser vibrometer is incident on the center of the membrane and as the membrane changes position the laser vibrometer registers a change in velocity that is converted into a change in membrane position or deflection.

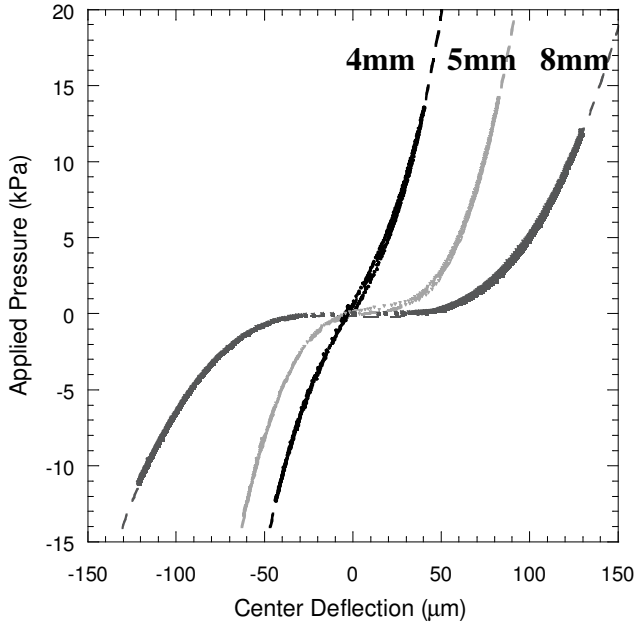

Figure 7.5: Applied pressure vs. center deflection response of 4, 5, 8 mm membranes, which have PZT thicknesses of 2, 3, and 3 μm, respectively.

This produces a smooth pressure vs. deflection relationship, in which any pressure within the applied pressure range will have a corresponding deflection, as shown in figure 7.5.

There are several properties that are measured and reported for piezoelectric membranes. One of the key components of the discussion in this paper is the transverse piezoelectric coefficient, e_{31}. The membranes used in this test are 2x8 mm rectangular membranes. A rectangular membrane is utilized because the strain induced in the membrane by the applied pressure is uniaxial [12, 15, 19]. The transverse piezoelectric property is calculated with

$$e_{31} = \frac{Q}{A\varepsilon_1} \tag{1}$$

where Q is the charge produced by the piezoelectric material, A is the area of the electrode, and ε_1 is the in-plane uniaxial strain. The uniaxial strain is defined by [20]

$$\varepsilon_1 = \frac{2}{3}\frac{\delta^2}{a^2} \tag{2}$$

where δ is the center deflection and a is half of the membrane's short side length. A laser vibrometer is used to measure the deflection of the membrane. The pressure and deflection are recorded by a computer with a *LabView* program. In addition, a Keithley 617 Electrometer is used to measure the charge that is produced by the piezoelectric membrane. Initially the membrane is bulged from a zero deflection state to a higher deflection state with a specific applied pressure, which ranges from 0 to 12 kPa. Once the membrane is deflected and the pressure is stable, the electrometer is zeroed and simultaneously the applied pressure is removed. With full depressurization, the electrometer provides the amount of charge produced by the change in the strain of the

membrane. Three similar PZT films were tested with this method and the typical e_{31} was found to be 3.995 C/m^2.

7.2 Results and Discussion

In a static deflection test the amount of charge produced is related to the capacitance of the membrane, *C*, and the voltage field generated between the electrodes, *V*, by [21]

$$Q = CV \tag{3}$$

In order to determine the electrical energy output from the square membranes,

$$D_i = \sum e_{ik}\varepsilon_k \tag{4}$$

is utilized, where D_i is the electric displacement, e_{ik} is the piezoelectric coefficient, and ε_k is the strain in the membrane. The indices *i* and *k* can be *1*, *2*, or *3*, which correspond to directions in the plane, *1* and *2*, and perpendicular to the plane of the membrane, *3* [22]. Since the applied pressure in these tests was in the direction perpendicular to the plane of the membrane, the electric displacement will have the index *3*. In the case of uniaxial strain, which correlates to the rectangular membrane tests, the electric displacement is given by

$$D_3 = e_{31}\varepsilon_1 \tag{5}$$

In the case of the biaxial strain in square membranes,

$$D_3 = e_{31}\varepsilon_1 + e_{32}\varepsilon_2 \tag{6}$$

The induced strain in the square membranes is biaxial, so $\varepsilon_1=\varepsilon_2$. In addition, since the microstructure of the PZT films is columnar in the *3* direction of the film and randomly oriented in the plane of the film, $e_{31}=e_{32}$. Therefore, (6) can be rewritten as

$$D_3 = 2e_{31}\varepsilon_1 \tag{7}$$

With the area of the electrode, A, and the transverse piezoelectric coefficient, e_{31}, for the case of biaxial strain [23],

$$D_3 = \frac{Q}{A} = 2e_{31}\varepsilon_1 \tag{8}$$

This expression can be rearranged to form,

$$Q = \frac{4}{3}\frac{e_{31}\delta^2 A}{a^2} \tag{9}$$

in which the charge is dependent on membrane geometry, the deflection, and the transverse piezoelectric coefficient, e_{31}.

The electrical energy can be determined from the charge measurements described in the previous section. The electrical energy, Ue, is defined by [21]

$$U_e = \frac{1}{2}CV^2, \tag{10}$$

where C and V are the capacitance and open circuit voltage as defined previously. Substitution of (3) and (9) into (10) with algebraic manipulation provides

$$U_e = \frac{4}{9}\frac{e_{31}^2\delta^4 A^2}{Ca^4} \tag{11}$$

for calculating the electrical energy produced by a square membrane.

The strain energy, U_S, within a deflected membrane is determined with

$$U_S = \frac{Yt}{2(1-\nu^2)}\iint(\varepsilon_x^2 + \varepsilon_y^2 + 2\nu\varepsilon_x\varepsilon_y + \frac{1}{2}(1-\nu^2)\gamma_{xy})dxdy \tag{12}$$

in which Young's modulus, Y, the total membrane thickness, t, and Poisson's ratio, υ, are accompanied by the strains in the membrane that are given by ε_x, ε_y, and γ_{xy} [24]. The composite modulus for each membrane was determined from a measured pressure

vs. deflection curve, while the PZT film thickness was determined with FESEM. Using the software program *Mathematica*, (12) was evaluated in order to calculate the strain energy input to the square membranes examined in this study. Because the deflection of the membranes is larger than the thickness of the membrane, bending effects have been neglected.

In order to account for the residual stress, Bonnotte *et al*. provide the expression, [25]

$$P(\delta) = Y_B \frac{t^3 \delta}{(.015)a^4} + \frac{(3.40)\sigma_0 t \delta}{a^2} + \frac{(1.82)Y_B t \delta^3}{a^4}, \qquad (13)$$

where δ, Y_B, t, a, and σ_0 are the deflection, biaxial modulus, membrane thickness, half the membrane side length, and the stress within the membrane, respectively. Since the thickness, biaxial modulus, and membrane side lengths are known for the membranes, the residual stress was determined with (13). Figure 7.5 reveals that with this expression, the pressure versus deflection curves match theory very well. The 4 mm membrane, which has a SiO_2 thickness of 110 nm, has a residual stress of 56 MPa, while the 5 and 8 mm membranes, which have a SiO_2 thickness of 0.5 μm, have residual stresses of less than 5 MPa.

For the applied peak-to-peak pressures used to operate the piezoelectric membranes in this research, the coupling coefficient is defined as the ratio of the electrical energy out, U_e, over the total input energy, $U_S + U_e$ [7],

$$k^2 = \frac{U_e}{U_S + U_e} \qquad (14)$$

Figure 7.6 shows the electric energy output divided by the strain energy input for several membranes as a function of the characteristic membrane strain. The

characteristic membrane strain is a convenient method to eliminate the effect of the membrane side length on the induced strain during testing. Membranes with 4, 5, and 8 mm side lengths were tested. The 4 mm membranes were poled with a field of 12 V/µm. The 5 mm membrane results show some variation that is most likely due to slight differences in PZT thickness and piezoelectric properties. The 5 mm membranes were poled with the same applied field of 10 V/µm. The 8 mm membranes were all poled with a field of 15 V/µm.

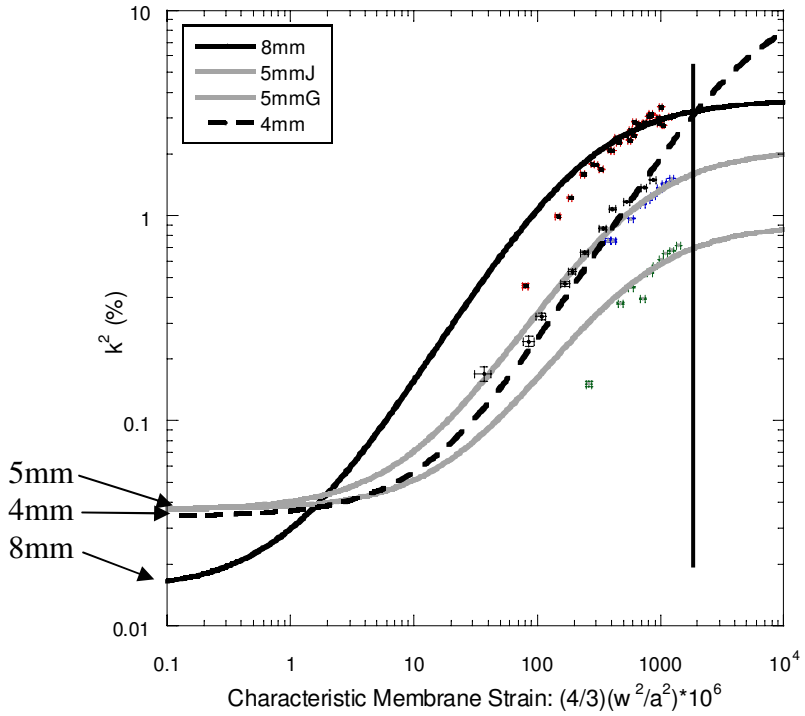

Figure 7.6: Membranes tested for k^2 limit versus applied strain.

The coupling coefficient was measured with an impedance analyzer that provided the lower bound values for the 4, 5, and 8 mm membranes of 342µ, 370µ, and 150µ, respectively, the locations of which are designated by arrows in figure 7.6. The solid

vertical line in figure 7.6 indicates the approximate fracture strain that is typical for these membranes.

FESEM micrographs were used to examine the PZT microstructure in cross section for samples that are from different parts of the same wafer. It was found that the grain structure is columnar over the entire wafer with some variation in grain size, as shown in figure 7.7. It was also determined that the thickness varies by 0.06 μm from the center to the edge of the wafer, which is due to changes in revolution speed during the PZT deposition process [26]. This corresponds to a thickness variation of 1.5%.

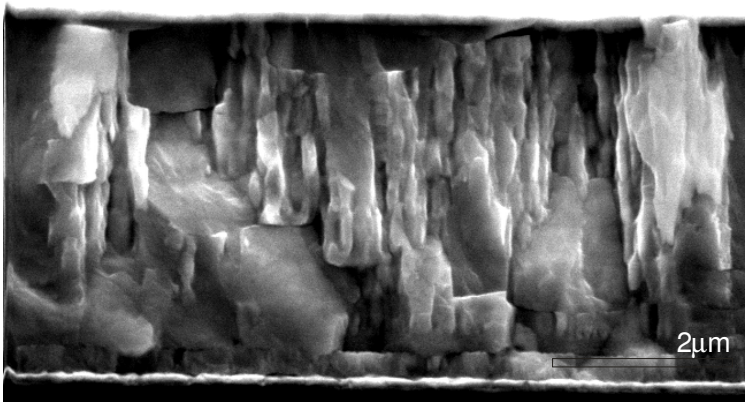

Figure 7.7: FESEM micrograph of a PZT cross section at the center of the wafer.

A recent study by Morris *et al.* provides a derivation of the ratio of the electromechanical coupling, k^2 [16]. This recent study focused on the membrane stretching regime because applied pressures were 5-25 kPa and initial stresses were large, which allows bending effects to be neglected. Morris shows that the normalized

electromechanical coupling increases as the characteristic membrane strain increases with

$$\frac{k^2}{k_{31}^2} = \frac{\chi_D \varepsilon_{char}}{\frac{2\gamma}{\tau_P}\frac{\sigma_r}{E_P} + \varepsilon_{char}\frac{\delta}{\tau_P}[\tau_P + \frac{E_P}{E_S}(1-\tau_P)]} \tag{15}$$

where χ_D is a constant that is related to the mean strain in a pressurized membrane, ε_{char} is the characteristic membrane strain, γ and δ are shape constants, $_P$ is the thickness fraction of the piezoelectric material, E_P is the modulus of the piezoelectric film, E_S is the thickness weighted average moduli of the support materials, and σ_r is the residual stress of the membrane. The electromechanical coupling coefficient approaches a limit that depends on the type of elastically isotropic material used to produce the charge. The type of sol-gel PZT used in Morris's study is the same as that used for obtaining the results presented in figure 7.6. Morris predicts that there is a limit to $k^2 \approx 0.6\%$ for high stress (120 MPa) membranes and approximately 2.0% for low stress (40 MPa) membranes. The limit in k^2 is readily calculated using

$$k_{31}^2 = \frac{e_{31}^2}{\varepsilon_{33} E_p}, \tag{16}$$

where E_p is the modulus of the piezoelectric film and ε_{33} is the dielectric constant. This expression is appropriate in the stretching regime. The experiments used to verify the predicted behavior of the square diaphragms in Morris's study are similar to the experiments conducted for the discussion in this paper. However, the difference is that Morris's experiments produced instantaneous charge at specific applied pressures and the experiments discussed here produce average charge measurements for a particular peak applied pressure. Figure 7.6 reveals that for each type of membrane, the curve fit that is

provided by the addition of the bending contribution that was measured with the impedance analyzer, and the stretching contribution, which was determined with (15), aligns well with the data. The measured values that were used for e_{31} and ε_{33} are provided in Table 7.1. A reasonable measured value for E_p is 70 GPa. The variation between prediction and the data shown in figure 7.6 may be due to the differences in testing procedure, which in this case provides an average k^2 rather than an instantaneous value. Since each of the membranes tested that are discussed here have a residual stress of 56 MPa or less, the data aligns well with the theory that the k^2 limit should be approximately 2% for membranes with a residual stress of approximately 40 MPa.

Table 7.1: Properties used to calculate coupling coefficient in equation (16).

sample	e_{31} (C/m^2)	ε_{33} (F/m)
4mm	4.8	$6.04*10^{-9}$
5mmG	3.9	$6.44*10^{-9}$
5mmJ	3.9	$6.75*10^{-9}$
8mm	5.06	$7.67*10^{-9}$

7.3 Conclusions

Piezoelectric membranes were tested for the purpose of determining the electromechanical coupling limit for large strains in the stretching mode. Static membrane tests were conducted to determine the transverse piezoelectric coefficient e_{31}. It was determined that the static pressure vs. deflection results match well to theory that incorporates the residual stresses inherent to composite piezoelectric membranes. The average output charge for the sol-gel PZT film combined with the biaxial strain were utilized in calculating the output electrical energy for large deflections of the membrane. The strain energy input to the membrane was determined utilizing a formulation provided

by literature with applied pressure and deflection data. The ratio of the electrical energy out over the input strain energy provided results that correlate well with a similar recent study of square diaphragms. Despite testing differences with this recent study, each membrane provided an electromechanical coupling limit that was very similar to the predicted k^2 limit of 2% provided by theory.

References

[1] A.M. Flynn, L.S. Tavrow, S.F. Bart, R.A. Brooks, D.J. Ehrlich, K.R. Udayakumar, L.E. Cross, "*Piezoelectric micromotors for microrobots*," Journal of Microelectromechanical Syst. **1** (1992) p.44.

[2] M.-A. Dubois, P. Muralt, "*PZT thin film actuated elastic fin micromotor*," IEEE Trans. Ultrason. Ferroelect. Freq. Contr. **45** (1998) p. 1169.

[3] B. Adhikari, S. Majumdar, "*Polymers in sensor applications*," Progress in Polymer Science **29** (2004) p. 699.

[4] P. Luginbuhl, S.D. Collins, G.-A. Racine, M.-A. Gretillat, N.F.d. Rooij, K.G. Brooks, N. Setter, "*Ultrasonic flexural Lamb-wave actuators based on PZT thin films*," Sensors and Actuators A **64** (1997) p. 41.

[5] M.-A. Dubois, P. Muralt, "*Measurement of the effective transvers piezoelectric coefficient $e_{31,f}$ of AlN and Pb(Zr_x, Ti_{1-x})O_3 thin films*," Sensors and Actuators A **77** (1999) p. 106.

[6] P. Muralt, "*Piezoelectric thin films for MEMS*," Integrated Ferroelectrics **17** (1997) p. 297.

[7] "IEEE Standard on Piezoelectricity," IEEE Std **176** (1987) p. 44-46.

[8] J. Cho, C.D. Richards, M.A. Anderson, D.F. Bahr, and R.F. Richards, "*Optimization of electromechanical coupling for a thin-film PZT membrane: I. Modeling*," Journal of Micromechanics and Microengineering **15** (2005) p. 1797.

[9] C. Johnson, J. Ruud, R. Bruce, D. Wortman, "*Relationship between residual stress, microstructure and mechanical properties of electron beam-physical vapor deposition thermal barrier coatings*," Surface and Coatings Technology **108-109** (1998) p. 80.

[10] L. Vergara, M. Clement, E. Iborra, A. Sanz-Hervas, J. Gacia Lopez, Y. Morilla, J. Sangrador, M. Respaldiza, "*Influence of oxygen and argon on the crystal quality and piezoelectric response of AlN sputtered thin films*," Diamond and Related Materials **13** (2003) p. 839.

[11] J. Cho, M. Anderson, R. Richards, D. Bahr, C. Richards, "*Optimization of electromechanical coupling for a thin-film PZT membrane: II. Experiment*," Journal of Micromechanics and Microengineering **15** (2005) p. 1804.

[12] Y. Xiang, X. Chen, T.Y. Tsui, J-I. Jang, J.J. Vlassak, "*Mechanical properties of porous and fully dense low-k dielectric thin films measured by means of nanoindentation and the plane-strain bulge test technique*," Journal of Materials Research **21** (2006) p. 386.

[13] A. Degen, N. Abedinov, T. Gotszalk, E. Sossna, M. Kratzenberg, I.W. Rangelow, "*Stress analysis in Si membranes for open stencil masks and mini-reticles using double bulging and resonance methods*," Microelectronic Engineering **57-58** (2001) p.425.

[14] S. Raja, P.K. Sinha, G. Prathap, D. Dwarakanathan, "*Influence of active stiffening on dynamic behavior of piezo-hygro-thermo-elastic composite plates and shells*," Journal of Sound and Vibration **278** (2004) p. 257.

[15] J.J. Vlassak and W.D. Nix, "*A new bulge test technique for the determination of Young's modulus and Poisson's ratio of thin films*," Journal of Materials Research **7** (1992) p. 3242.

[16] U. Komargiri, M.R. Begley, J.G. Simmonds, "*The mechanical response of freestanding circular elastic films under point and pressure loads*," Journal of Applied Mechanics **72** (2005) p. 203-212.

[17] D.J. Morris, M.C. Robinson, L.W. Weiss, C.D. Richards, R.F. Richards, D.F. Bahr, "*Mechanical-to-electrical energy conversion of thin-film piezoelectric diaphragms*," Mater. Res. Soc. Symp. Proc. **973** (2007) BB06-04.

[18] M.C. Robinson, D.J. Morris, P.D. Hayenga, J. Cho, R.F. Richards, C.D. Richards, D.F. Bahr, "*Structural and electrical characterization of PZT on gold for micromachined piezoelectric membranes*," Applied Physics A: Materials Science and Processing **85** (2006) p. 135.

[19] T.M. Sullivan, "*Development of a Novel Method for Measuring the Transverse Piezoelectric Coefficients of Thin Piezoelectric Films*," Masters Thesis, Washington State University (2004).

[20] R.P. Vinci and J.J. Vlassak, "*Mechanical behavior of thin films*," Ann. Rev. Mat. Sc. **26** (1996) p. 431.

[21] E. Hecht, Physics Calculus, Brooks and Cole Publishing Company (1996).

[22] S. Trolier-McKinstry, P. Muralt, "*Thin film piezoelectrics for MEMS*," Journal of Electroceramics **12** (2004) p. 7.

[23] M.F. Iskander, Electromagnetic Fields and Waves, Prentice-Hall Inc. (1992).

[24] S. Timoshenko, S. Woinowsky-Krieger, Theory of Plates and Shells, McGraw-Hill (1959).

[25] E. Bonnotte, P. Delobelle, L. Bornier, "*Two interferometric methods for the mechanical characterization of thin films by bulging tests. Application to single crystal silicon*," Journal of Materials Research **12** (1997) p. 2234.

[26] L.M. Eakins, "*Development and characterization of materials in MEMS power generation*," Masters Thesis, Washington State University (2003).

CHAPTER EIGHT

POWER PRODUCTION FROM A MEMS SCALE OSCILLATING PZT MEMBRANE

Dynamic operation of piezoelectric membranes has been utilized recently to characterize and develop MEMS devices that produce micropower. Typically, reports of piezoelectric output include how the material properties of the membrane are improved or the amount of output voltage is presented in relation to a specific change in membrane structure [1, 2, 3]. The purpose of these types of improvements to the membrane is often meant to meet design specifications of MEMS devices [4, 5]. The P3 micro engine [6], contains a membrane with a piezoelectric element, which produces electrical power from the engine cycle, and the operation of this membrane will be discussed in this chapter.

The ability for a piezoelectric membrane to produce electrical power is influenced by many factors. An investigation was conducted for membranes that have a piezoelectric layer within the composite structure. Dynamic operation enabled the investigation to include similar operating conditions to the micro engine, while examining geometric and material property effects on the amount of micropower produced by the membrane.

The operating conditions of the micro engine that drive the design specifications of the piezoelectric membrane include having a resonance that is as low as possible, a compliant membrane with low residual stress, and a heat transfer rate that creates efficiently produced micropower [6]. In order to meet these specifications, aspects of the membrane geometry were examined including the electrode configuration and the layer

thicknesses within the composite structure. In addition, material properties were studied including PZT chemistry and the transverse piezoelectric coefficient, e_{31}. The combination of utilizing the dynamic testing apparatus in experiments and analytical calculations enabled a predictive expression for micropower production for the piezoelectric membrane to be formed. The discussion that follows will describe how this prediction tool was created and verified with both experiment and theory.

8.1 Experiment

8.1.1 Membrane Fabrication

Several square membranes were micromachined from a composite structure that consisted of Si/SiO_2/Ti/Pt/PZT/Ti/W/Au layers. The membranes in each experiment described in this chapter had this structure, but the individual film layer thicknesses varied from experiment to experiment. The side lengths of the square membranes varied from 3 to 8 mm. The electrode size typically covered 60% of the membrane and was centered over the membrane. Section 8.2.6 describes a few cases in which the electrode coverage was changed. Therefore, each section will include a brief description of the membrane structure that was utilized in each specific experiment.

A typical membrane was fabricated initially by thermally growing a silicon oxide layer on a boron doped silicon wafer. The oxide thicknesses for these membranes ranged from 110 to 500 nm. A 175 nm Pt film was then DC magnetron sputtered with a 5 nm thick Ti adhesion layer onto the oxide. This layer was heat treated to 650 ºC for 10 minutes, in order to improve adhesion with the piezoelectric film. Two types of piezoelectric film will be discussed in this chapter, but the typical process involved

solution deposition of approximately 100 nm of lead zirconate titanate (PZT), which was then heat treated at 350 ºC for 1 minute [7]. Two additional layers were deposited and heat treated in a similar manner. Then the wafer was placed into a Heatpulse 610 rapid thermal annealer (RTA) for 30 seconds at 650 ºC. This solution deposition process continued until the desired PZT film thickness was achieved, which ranged from 1 to 3 µm. A 300 nm Au film was then DC magnetron sputtered onto the PZT with a 12 nm Ti/W adhesion layer. This entire film stack comprised the composite structure, which was then patterned with contact photolithography and various regions were etched to create the micromachined membranes that were utilized for this research.

8.1.2 Testing Procedure

A detailed description of how to test the composite membranes for output power is described in Appendix III. The experiments described in this chapter utilize various portions of the complete description provided in Appendix III. Therefore, each section of this chapter will include a brief description of the testing procedure that was used.

Typical testing procedures involved poling each membrane one day prior to testing. Then, the membrane was clamped between two plexiglass disks, while deionized water was sealed beneath the cavity. The clamped disks with the membrane were then placed over the hole in the dynamic bulge test apparatus and clamped down. Appendix III provides a picture of the top of the dynamic bulge test apparatus and the hole that is centrally located. There is deionized water covering the hole, in order to eliminate any air bubbles from entering the system once the carrier setup is clamped into place. Figure 3.3 shows a top view of the clamped plexiglass carrier that has the membrane visible with

electrode access points to each side of the membrane. The capacitance of the membrane was then measured to ensure it has not shifted during assembly. Appendix III shows how the probes are placed onto the electrode access points. A good electrical connection is indicated by a capacitance of 5 to 150 nF, depending on the type of membrane, while the membrane is stationary in the carrier. A variable load resistor is connected in series with the electrodes. The driving piezoelectric-stack and amplifier were turned on so that the membrane oscillated at a low frequency. The frequency was then ramped up slowly to find resonance. From this point, the testing procedures that followed depended on what type of experiment was desired.

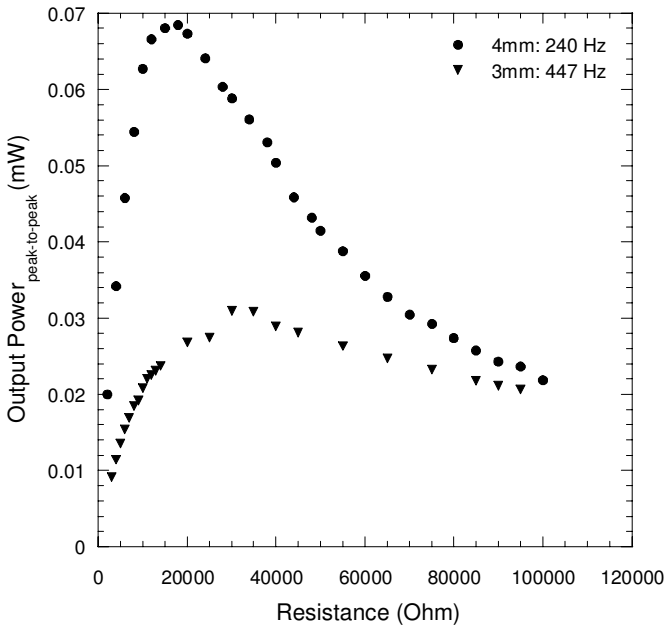

Figure 8.1: Typical load resistance vs. the peak-to-peak power curves for a 3 and 4 mm membrane that were operated at resonant frequencies of 447 and 240 Hz, respectively.

Typically the first step in the testing procedure is to determine the load resistance that matches the impedance of the membrane, as shown in figure 8.1 for a 3 and 4 mm membrane. This enables the maximum output power to be calculated from the charge produced by the membrane during operation. For the 3 and 4 mm membranes, the maximum power is achieved by using a load resistance of 30 and 18 kΩ, respectively. Chapter 3 provides a detailed description of how to calculate the maximum output power from the load resistance.

8.2 Results and Discussion

8.2.1 Poling

By definition, poling is the dipole alignment by an electric field. The polarization after the removal of the field is called remanant polarization, P_r. The field necessary to bring the polarization to zero is called the coercive field, E_C. The spontaneous polarization, P_s, can be defined as the surface charge density or the dielectric displacement of the polar material or the dipole moment per unit volume. It should be noted that E_C is determined from the intercept of the hysteresis loop with the field axis and is not an absolute threshold field [8]. When the PZT is initially deposited and heat treated, it has a small amount of spontaneous polarization. However, this amount is not capable of producing the output charge that is required by MEMS devices. Hence, the piezoelectric membranes were poled prior to testing. Poling conditions vary widely for different materials. Ceramics are poled or subjected to a large electric field, by which domains switch to orient the spontaneous polarization with the applied field [9]. Some ceramics are heated during the poling process [10]. Studies have found that applying a

specified field across the piezoelectric material for a given amount of time provides a fully poled sample [11, 12]. The effect of poling conditions on the piezoelectric properties has been studied by other authors [13, 14]. In particular, Jonscher describes the total current through the piezoelectric material under an applied field as the polarization current, which arises from the tendency of the polarizing species in the material to respond in a delayed manner to the exciting field and must go to zero at infinitely long time, and the conduction current, which is constant with time and arises from a continuous movement of free charges across the dielectric material from one electrode to another. This current does not change in any way the "centre of gravity" of the charge distribution in the system. The polarization current, therefore, characterizes the most important property of the dielectric system [14]. Thus, while a field is applied to the piezoelectric film, the corresponding current should indicate if the film is fully poled by decreasing to nearly zero after some amount of time passes during poling.

Two different poling techniques were used to pole membranes for the research discussed in this chapter. One technique involved ramping up an applied field across the piezoelectric film, beginning with no field, holding at 12 V/μm for one minute and then slowly decreasing the field back to zero. This technique was used for membranes that had a piezoelectric layer thickness of 1 μm. For membranes with a side length of 3, 4, or 5 mm, this technique worked well. A software program in *Labview* was created to automatically control the ramp speed. However, once the membrane structures were changed so that the composite structure had a low composite residual stress, the ramping speed of the applied field was impractical because it needed to be very slow, or the

membrane would fracture. At this point, it was necessary to introduce the second type of poling technique.

The second poling technique also applied a field by ramping to a specified voltage, but simultaneously monitored the current. The ramping speed was adjusted with this system, in order to eliminate excessive current spiking that indicates fast dipole alignment and is the most likely cause of fracture. Figure 8.2 shows a poling cycle for an 8 mm membrane that had a 2.7 μm PZT film. The voltage was applied in 1 V increments with a holding time of 45 seconds between each increment. This figure shows that as the voltage is increased, the spikes in the current trace increase in height, which indicates that the dipoles within the film are aligning. A closer view of an individual current spike is provided in figure 8.3. It is evident that the current rises rapidly and decays exponentially. The current returns to nearly 0 A before the next peak, however it does not fully reach zero. This corresponds to the conduction current, which is small compared to the polarization current. The height of the spikes stays relatively level after approximately 10 V/μm is applied. Typically, it is difficult to decipher if the height of the spikes in the current are going to remain at this level. Therefore, the voltage is continually increased to see if any further spikes occur. There is a trade off though because the membrane can only receive so much applied voltage before it fails. Therefore, 18.5 V/μm was considered the limit to the applied voltage. In figure 8.2, once the voltage begins to decrease, the spikes in the current increase in height, but this is due to the speed at which the applied field is decreasing. This technique was used for some 5 mm and all of the 8 mm membranes that are discussed in this chapter.

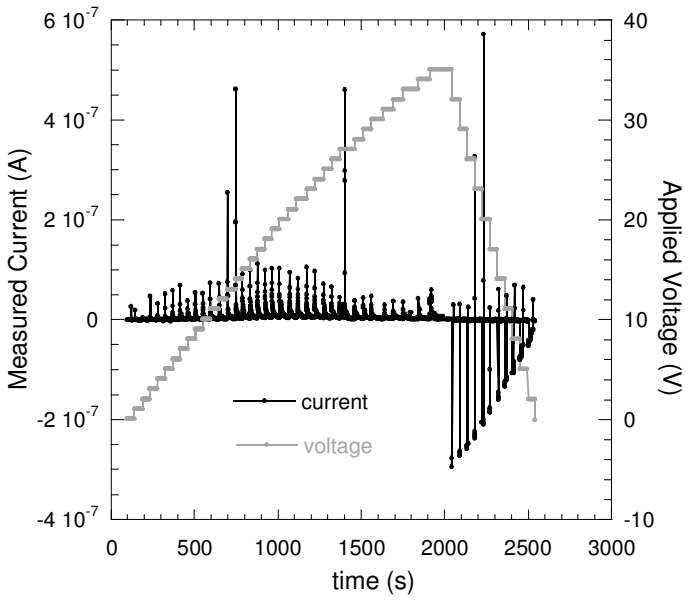

Figure 8.2: A typical poling process using the current monitoring technique during a ramp of an applied field to a 2.7 µm PZT film in an 8 mm membrane.

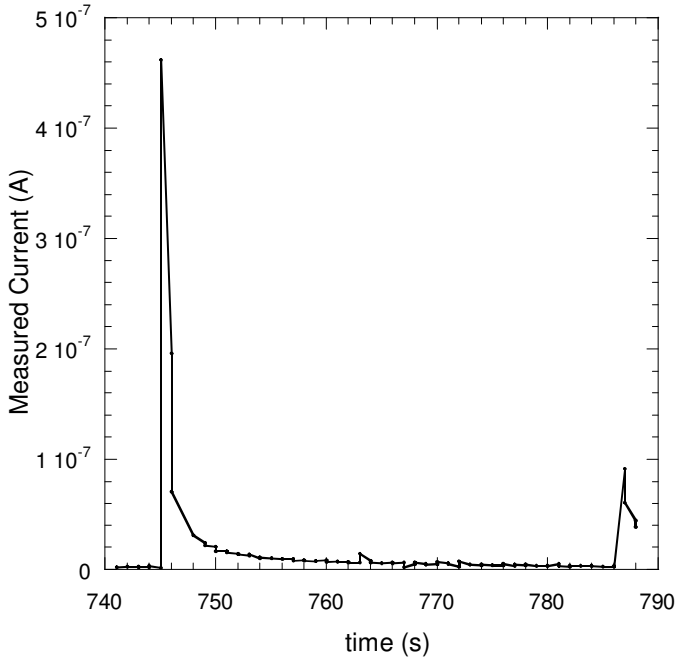

Figure 8.3: Closer view of an individual current spike, in order to examine the current behavior during poling.

8.2.2 RMS vs. Peak to Peak

The key element to each of the tests discussed in this chapter is the amount of output voltage. When the piezoelectric membrane oscillates, a charge is produced that can be measured as the output voltage from the membrane. The driving voltage that is applied to the membrane through the fluid that is coupled to the piezoelectric actuator is sinusoidal. However, the measured output from the membrane is not sinusoidal in either the open or closed circuit configuration. This is most likely due to the system that is comprised of the fluid, the carrier, the gasket, the membrane, and perhaps tiny bubbles that are introduced during assembly. Thus, in order to measure the output voltage accurately for a nonharmonic output signal, the root-mean-square voltage, V_{rms}, should be utilized. The peak-to-peak voltage, V_{pp}, is related to V_{rms} for a sinusoidal signal by

$$V_{rms} = \frac{V_{pp}}{2\sqrt{2}} \tag{1}$$

This provides a first order approximation using the peak-to-peak voltage. However, a more accurate method for determining the output rms power is to calculate the integral over the signal trace that is measured by an oscilloscope.

$$P_{rms} = \frac{1}{R}\frac{1}{T}\int_0^T V(t)^2\,dt \tag{2}$$

where R is the load resistance, T is one period of oscillation, and t is time. Solving this integral provides

$$P_{rms} = \frac{V_{pp}^2}{8R} \tag{3}$$

in which V_{pp} has been used as an approximation for $V(t)$ in (2) and since power is equal to V^2/R, then (1) follows directly. The values that are reported for output rms power in this dissertation were determined by the oscilloscope performing this integral over the output voltage data trace during dynamic testing. Equation (3) can be used, however, to approximate the amount of output rms power.

8.2.3 2MOE vs. HOAc PZT

The effect of the PZT chemistry on the performance of the membrane was investigated with the dynamic bulge tester apparatus. Two chemistries were examined including a 2MOE-based and a HOAc-based PZT, both of which had a 40:60 ratio of zirconium to titanium. The 3 mm membranes that were used in these experiments had a composite structure that consisted of 2.1 μm Si, 110 nm SiO_2, 175 nm Pt, 1 μm PZT, and 300 nm Au. It was important to have identical composite membrane structures, in order to reveal the effect of the PZT chemistry on the membrane performance.

One experiment was conducted that involved measuring the peak-to-peak output voltage for the case when the membranes have the same mean deflection, while the mean pressure was allowed to change. Figure 8.4 shows typical data traces for the applied pressure and center deflection. The mean deflection is approximately 4 μm, while the mean pressure in this case is approximately 8.5 kPa. Each membrane tested had a driving voltage of 20.8 V.

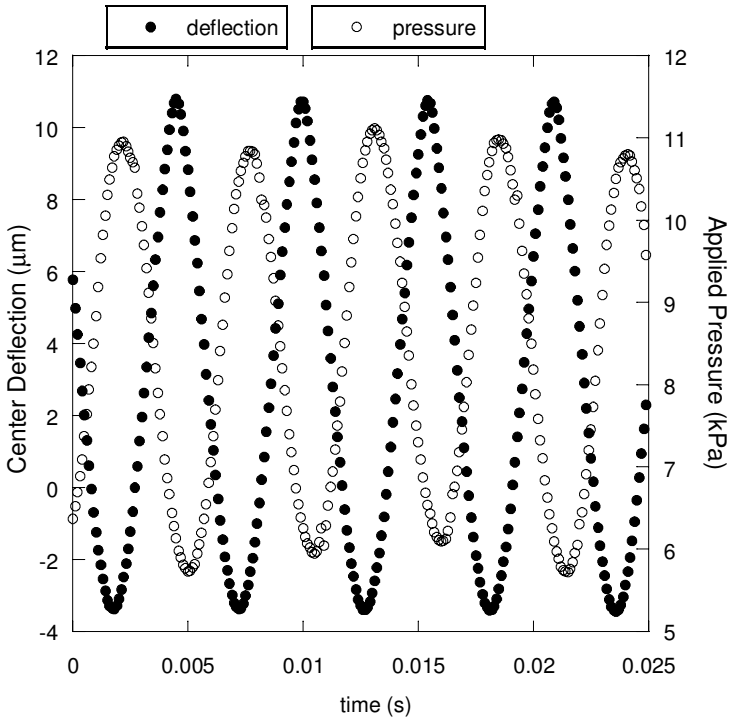

Figure 8.4: Typical data traces for the applied pressure and center deflection.

Table 8.1 provides each mean deflection that corresponds to the peak-to-peak center deflections for the HOAc and 2MOE based PZT membranes. For example, a 53.6 μm mean deflection was utilized for a peak-to-peak center deflection of 104 μm and 96 μm for the HOAc and 2MOE membranes, respectively. Figure 8.5 shows that the HOAc-based PZT chemistry consistently provided a higher peak-to-peak output voltage than the 2MOE-based PZT chemistry. The second experiment that was conducted involved measuring the peak-to-peak output voltage for specific levels of mean pressure. In this experiment the mean deflection was allowed to change, as shown in Table 8.2. Table 8.2 should be read in the same manner as Table 8.1, in which a mean pressure of 3.1 psi corresponds to a mean deflection of 53.6 and 38.4 μm for the HOAc and 2MOE cases.

Table 8.1: Summary of mean deflection and peak-to-peak center deflections used in experiment.

	peak-to-peak center deflection (μm)	
mean deflection (μm)	HOAc	2MOE
53.6	104.0	96.0
45.9	110.4	112.0
52.8	110.4	104.0
52.8	115.2	105.6

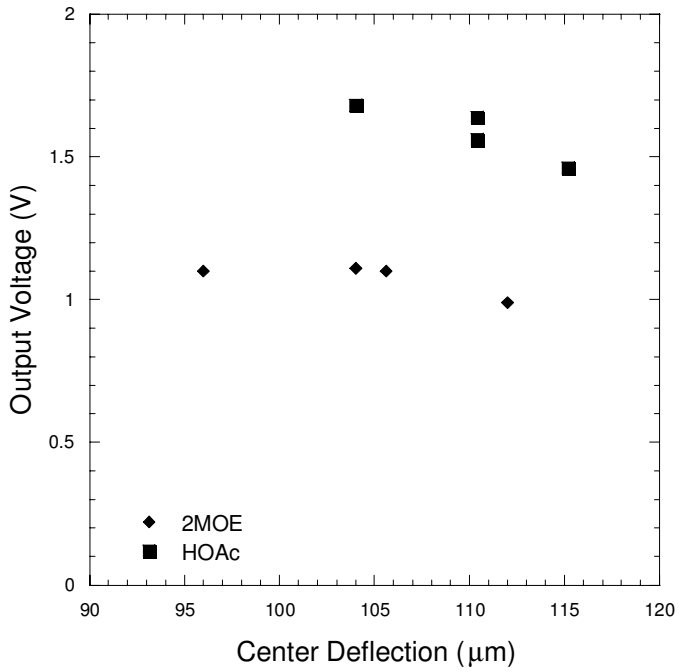

Figure 8.5: Comparison of the peak-to-peak output voltage with respect to peak-to-peak center deflection for HOAc-based and 2MOE-based PZT, at similar mean deflections.

Figure 8.6 shows a comparison of the peak-to-peak output voltage for the case when the mean pressure is the same for each type of membrane. In addition, figure 8.6 shows that the HOAc-based PZT membrane consistently produces more output voltage than the 2MOE-based PZT membrane. This is due to differences in the piezoelectric properties.

Table 8.2: Summary of mean pressures and mean deflections used in experiment.

	mean deflection (μm)	
mean pressure (psi)	HOAc	2MOE
3.1	53.6	38.4
2.6	45.9	48.0
2.2	52.8	56.6
1.6	52.8	56.8

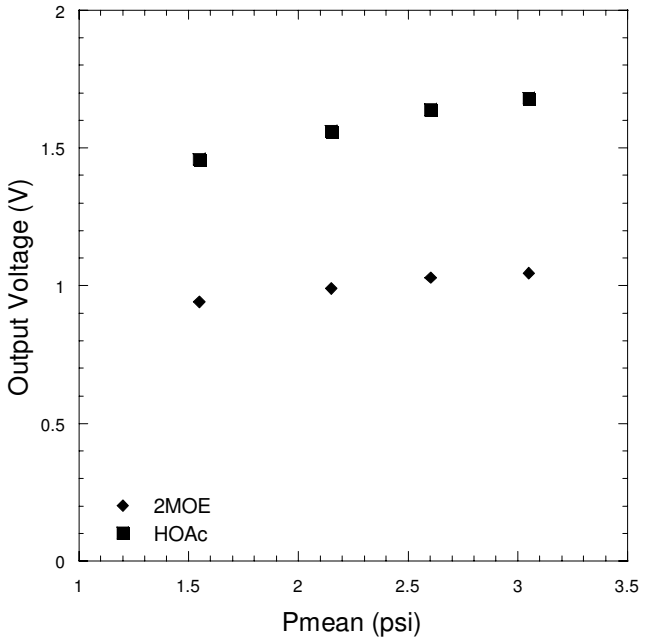

Figure 8.6: Comparison of the peak-to-peak output voltage for the case when the mean pressure is the same for each membrane comparison.

The average transverse piezoelectric constant, e_{31}, for the HOAc-based PZT films is 7.7 C/m^2, while for the 2MOE-based PZT films the average e_{31} is 6.1 C/m^2. The 3 mm membranes had the same PZT thickness, t_{PZT} = 1 μm and electrode area, A_{el} = 0.0026 m. The capacitance, C, for the HOAc membrane was 56.1 nF while the 2MOE sample had a capacitance of 45.5 nF. Therefore, the dielectric constant, ε_r, is

$$\varepsilon_r = \frac{Ct_{PZT}}{8.85 * 10^{-12} A_{el}^2} \quad (4)$$

The dielectric constants for the HOAc and 2MOE PZT films are 937 and 760, respectively. A useful method for comparing the power generation produced by piezoelectric membranes is to calculate the figure of merit (FOM), as defined by Muralt *et al.* [15],

$$FOM = \frac{e_{31}^2}{\varepsilon_r \tan \delta} \quad (5)$$

where $tan\delta$ is the dielectric loss tangent and is assumed to be 0.03. The FOM for the HOAc and 2MOE films are calculated to be 2.11 and 1.63, respectively, a 28% increase for the HOAc films. This is similar to the 50% increases in performance in figures 8.5 and 8.6, suggesting that the FOM is a good first order estimate of dynamic performance.

8.2.4 Resonance vs. Off-Resonance

An investigation of how the frequency of operation affects the output power and overall performance was conducted. The 5 mm membranes that were used for these experiments had a composite structure that consisted of 1.5 µm Si, 1 µm SiO_2, 175 nm Pt, 3 µm HOAc PZT, and 300 nm Au. The PZT was patterned so that the PZT was etched around the entire membrane except for the location where the top electrode tail extends off of the membrane. The result of etching the Si with EDP for 6 hours was finger-like buckling at the edges of the membrane where the PZT had been etched. The partial buckling indicates that the 5 mm membranes had a low residual composite stress. Each of the membranes was poled for 10 minutes with 36 V one day prior to testing.

Initially, five 5 mm membranes, which all had the same composite structure, were tested with the impedance analyzer for comparison to the upcoming experiments. Table 8.3 provides a summary of the results found for the membranes. The coupling coefficient, k^2, resonant frequency, f_r, quality factor, Q, efficiency, η, and load resistance, R_L, were calculated as described in section 4 of chapter 3.

Table 8.3: Summary of experiment impedance data.

5x5 mm, 3 µm HOAc PZT, 1.5 µm Si, 1 µm SiO_2, 175 nm Pt, 300 nm Au									
sample	C_o (nF)	R_m (kΩ)	L_m (H)	C_m (nF)	k^2 ($*10^{-6}$)	f_r (kHz)	Q	η	R_L (Ω)
5-N	27.8	25.9	35.9	0.0181	652	6.23	54.2	1.74	919
8-A	28.4	19.9	24.8	0.0227	801	6.70	52.6	2.06	837
8-J	28.5	21.8	26.3	0.0228	800	6.50	49.2	1.93	860
7-C	29.5	46.0	13.7	0.0454	1540	6.39	11.9	0.91	845
7-J	30.8	28.5	18.8	0.0402	1300	5.79	24.0	1.54	893

The static bulge testing apparatus was utilized to obtain the pressure vs. deflection curves that are presented in figure 8.7. It is evident that the relationship between the applied pressure and center defection of these membranes is very similar because the curves overlay one another. The difference between these pressure deflection curves and the curves shown previously is that the membranes in this case were slightly compressive, since structural changes created low composite residual stressed membranes. The coupling coefficient and capacitance are listed in the legend of figure 8.7, in order to see if the curves track with either property. There is no correlation found between the capacitance or coupling coefficient to the pressure vs. deflection results.

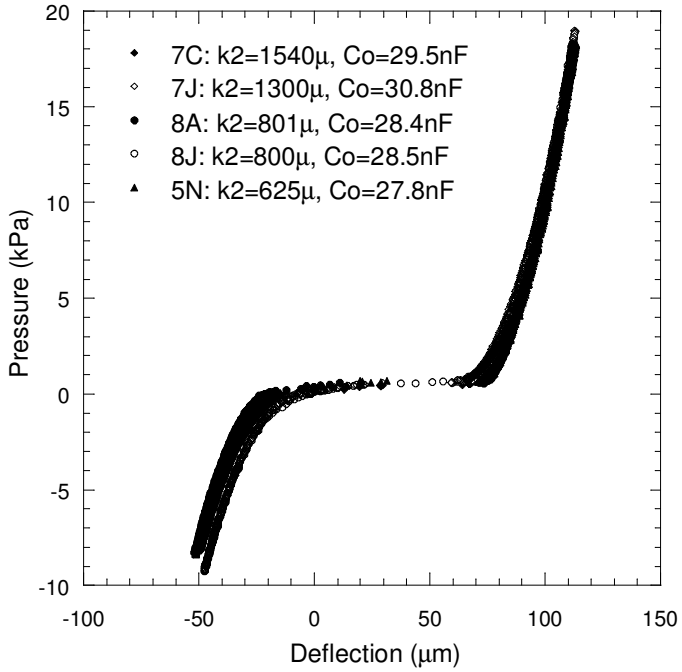

Figure 8.7: Comparison of static pressure deflection results for five 5 mm membranes.

Table 8.4: Summary of experiment data for five membranes.

Sample	System f_r (Hz)	R_L (kΩ)	R_L (kΩ) for 250 Hz
5N	183	30.7	22.5
8A	166	33.0	22.1
8J	154	33.9	20.1
7C	202	25.7	21.2
7J	218	24.0	20.9

In order to determine if the frequency of operation or the properties that were just discussed effect the output power or overall performance of the membrane, the dynamic bulge testing system was utilized. The system resonance is found when the output voltage signal reached a maximum peak-to-peak level, which corresponds to when there is a 90º phase shift between the pressure and the output signal. The system resonant frequencies for these membranes are listed in Table 8.4. With the system resonant

frequencies known, a frequency of 250 Hz was chosen for the off-resonance comparison. The next step in the testing process was to determine the load resistance that was required to match the impedance of the membrane and system. Since the load resistance is dependent on the capacitance and the frequency of operation by,

$$R_L = \frac{1}{2\pi f C_0} \tag{6}$$

the load resistances that were used are provided in Table 8.4 as well. During the experiment the mean pressure was maintained at 9 kPa, while the applied peak-to-peak pressure was increased. Simultaneously, the laser vibrometer measured the center deflection of the membrane. The root-mean-square (rms) power was calculated from the cycle rms output voltage and the corresponding load resistor by

$$P_{RMS} = \frac{V_{RMS}^2}{R_L} \tag{7}$$

Figures 8.8 and 8.9 show the rms power vs. the applied peak-to-peak pressure for the cases of system resonance and off system resonance. In general with an increase in applied peak-to-peak pressure there is an increase in output rms power. Similarly, figures 8.10 and 8.11 show that in general as the applied peak-to-peak pressure increases, the peak-to-peak center deflection increases at both system resonance and at off system resonance.

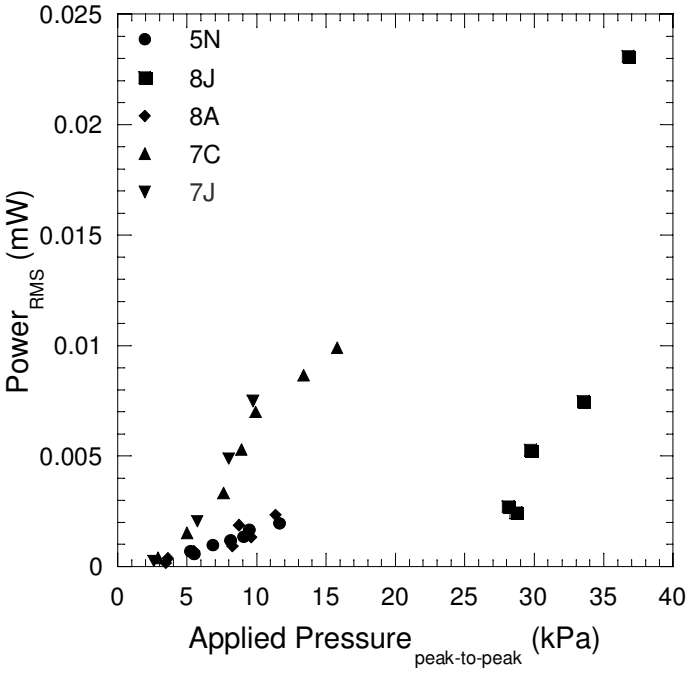

Figure 8.8: The rms power vs. the applied peak-to-peak pressure at system resonance.

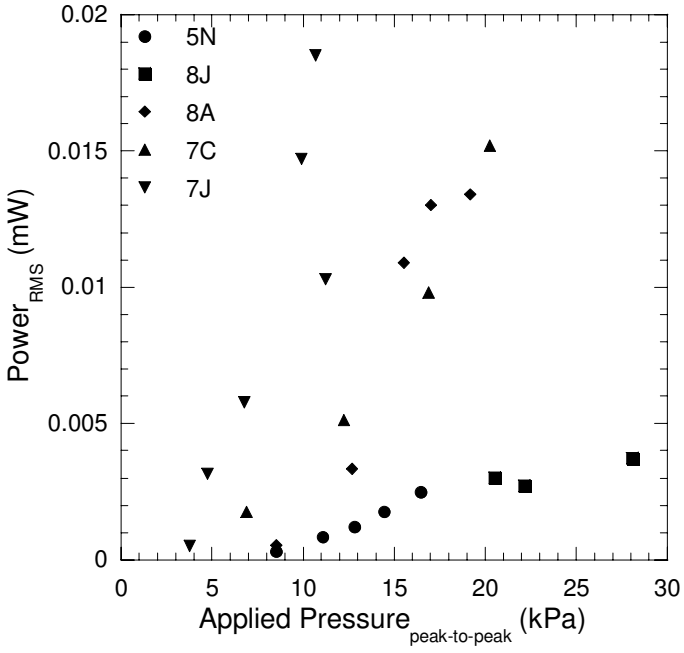

Figure 8.9: The rms power vs. the applied peak-to-peak pressure at off system resonance.

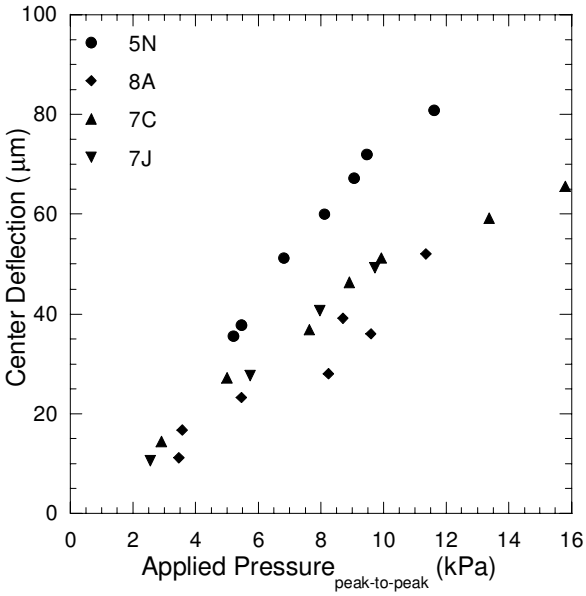

Figure 8.10: Comparison of the results for the center deflection vs. the applied peak-to-peak pressure at system resonance.

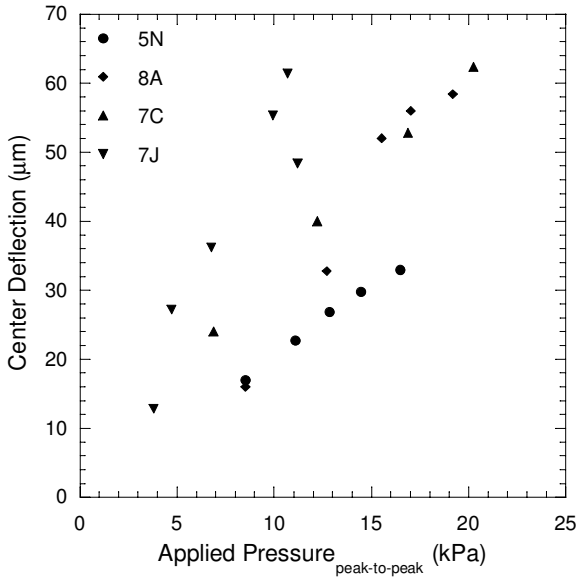

Figure 8.11: Comparison of the results for the center deflection vs. the applied peak-to-peak pressure at off system resonance.

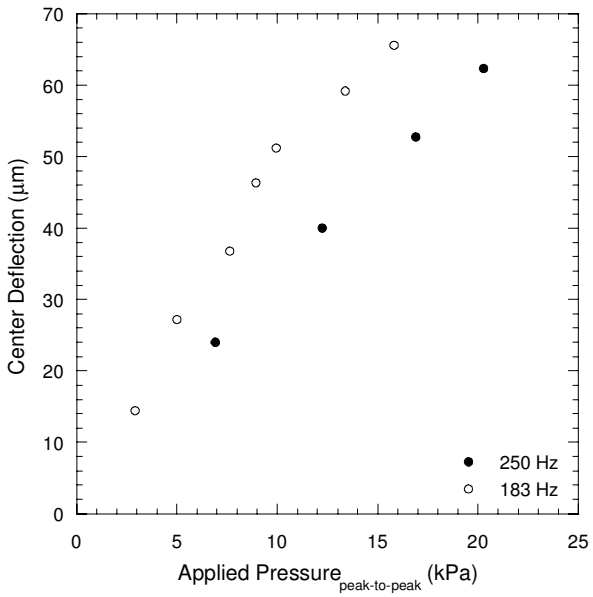

Figure 8.12: Comparison of the center deflection at system resonance to off system resonance for a given applied peak-to-peak pressure for membrane 7C.

Figure 8.12 shows that there is more peak-to-peak center deflection for a given applied peak-to-peak pressure in the case of system resonance compared to off system resonance. This is expected because system resonance provides the maximum output voltage during testing.

The relationship between the rms output power and the center deflection was examined. The strain in a membrane is proportional to the deflection squared,

$$\varepsilon = \frac{2}{3}\frac{\delta^2}{a^2} \tag{8}$$

and output power, P, is proportional to the output voltage squared,

$$P = \frac{V^2}{R} \tag{9}$$

The dynamic bulge test provides an output voltage signal that oscillates with the applied peak-to-peak pressure. This peak-to-peak voltage is translated into a specific voltage with respect to the percent strain, which is given by [16],

$$specific\_voltage = \frac{V}{t_{PZT}\varepsilon} \tag{10}$$

Therefore, the output power should be proportional to the deflection of the membrane, δ, raised to the fourth power,

$$P \propto \delta^4 \tag{11}$$

Figure 8.13 shows a schematic of the cross section of a membrane for two cases of mean deflection level. The oval in the left side of the schematic indicates that the membrane oscillates through the zero deflection state. This occurs when there is a low mean pressure applied to the membrane. The oval in the right side of the schematic indicates that the membrane oscillates at a higher level of mean deflection, in which case the membrane does not pass through the zero deflection state. This occurs with a high applied mean pressure.

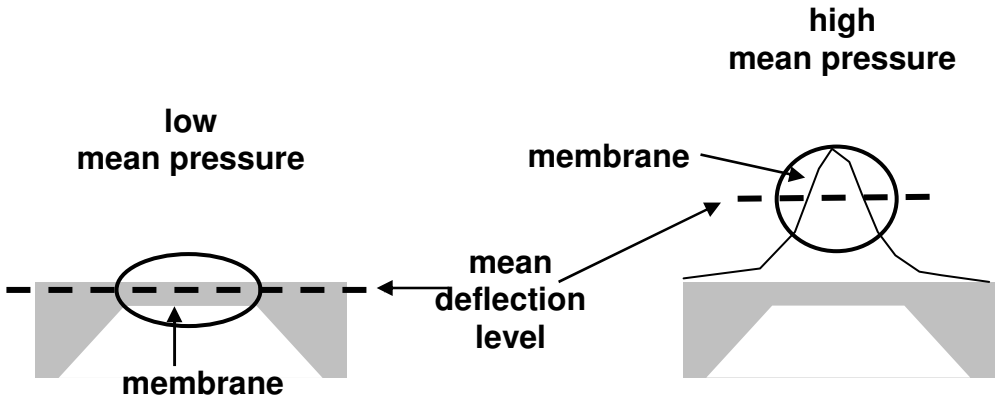

Figure 8.13: Schematic of a membrane in cross section for two cases of mean deflection.

Figures 8.14 and 8.15 reveal that the rms output power is dependent on the deflection amplitude. Figure 8.14 shows the system resonance case and the coupling coefficient for each data set in the legend. Also included in the figure is a power curve fit to each data set. In this case, as the coupling coefficient of the membrane increases, there is more power at a given peak-to-peak deflection. The membranes in this case oscillated through zero deflection with a mean pressure of less than 9 kPa.

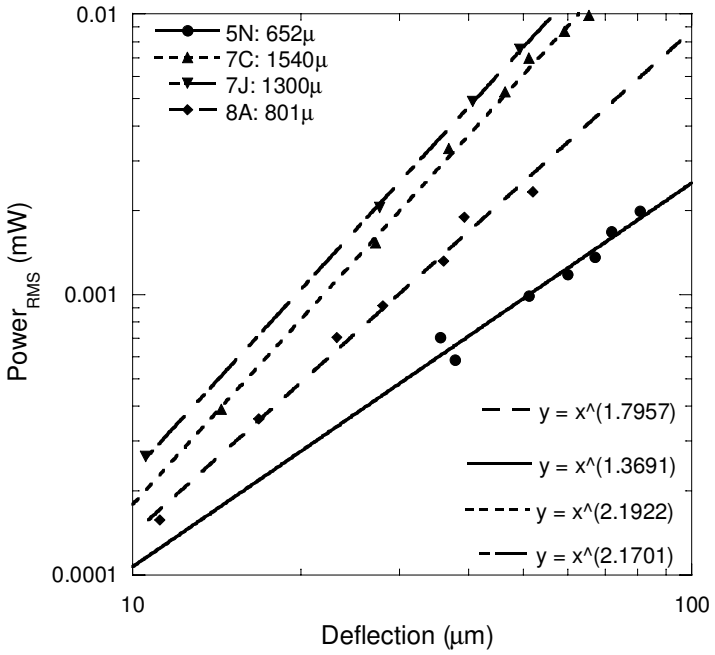

Figure 8.14: The output rms power vs. the deflection amplitude at resonance.

In contrast to this result, in the off system resonance case, figure 8.15 reveals that as the coupling coefficient increases for deflection amplitudes of up to approximately 60 μm, there is more power at a given peak-to-peak deflection. At deflections higher than 60 μm, then the two cases correlate. The most likely reasoning for the difference between the results for these resonant and off resonant cases is that the mean pressure in the off

resonant case reached levels of approximately 21 kPa. The mean pressure acts to stiffen the membrane during oscillation, creating behavior that is more plate-like compared to stretching, even though these were low composite residual stressed membranes. The results of the power curve fit show that the more plate-like the membrane is, the higher the level of the power in the power curve fit.

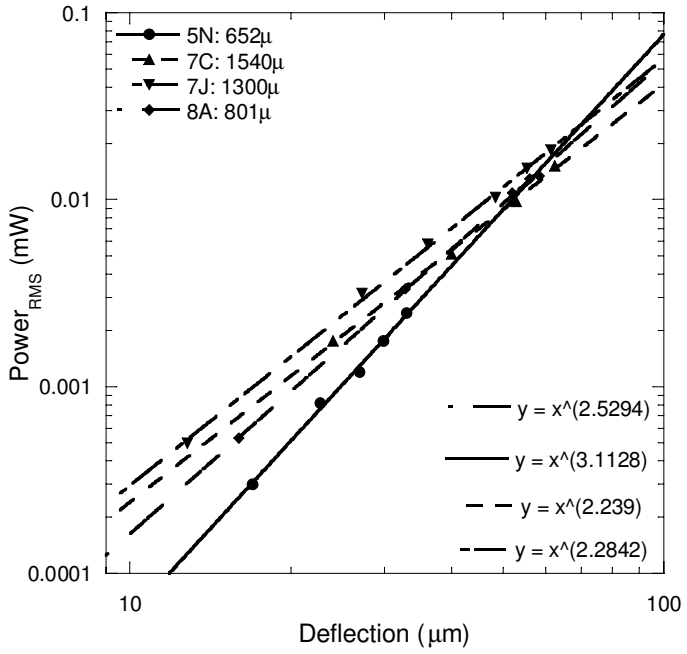

Figure 8.15: The output rms power vs. the deflection amplitude at off resonance.

8.2.5 Mean Pressure

The affect of the applied mean pressure on the amount of deflection and output power was investigated. Two 5 mm membranes were used, which had the same structure as the membranes in the previous section of this chapter. An operating frequency of 250 Hz was chosen because changing the mean pressure and having the system remain stable was not consistent at system resonance conditions. A peak-to-peak applied pressure of

10 kPa was used in each test, while the rms output power and center deflection were measured. Figure 8.16 shows that as the applied mean pressure increases from zero at an operating frequency of 250 Hz, the amount of deflection and rms output power increase. At an operating frequency of 150 Hz, the deflection and the output power slightly decrease as the mean pressure increases. The system resonant frequency for the 5N and 7C membranes was 183 Hz and 202 Hz, respectively. Since the membrane oscillated around zero deflection and was very low at an operating frequency of 150 Hz, the adjustment in the mean pressure decreased the amount of output power and deflection. At this operating frequency and level of oscillation, it is verified that the mean pressure acts to stiffen the membrane as it is increased. However, at an operating frequency of 250 Hz, as the mean pressure increased, both the output power and deflection increased. Even though the mean pressure increased, which stiffens the system, the membrane was oscillating about a level in which the membrane did not pass through the zero deflection point. The deflection of the membrane oscillated only above zero deflection. Therefore, the effect of the mean pressure was combined with the dominant effect of the level of deflection oscillation. The coupling coefficient for the 5N and 7C membranes was 652μ and 1540μ, respectively. Because of this, it was expected that there would be more output power from membrane 7C. This is verified in figure 8.16 for both cases.

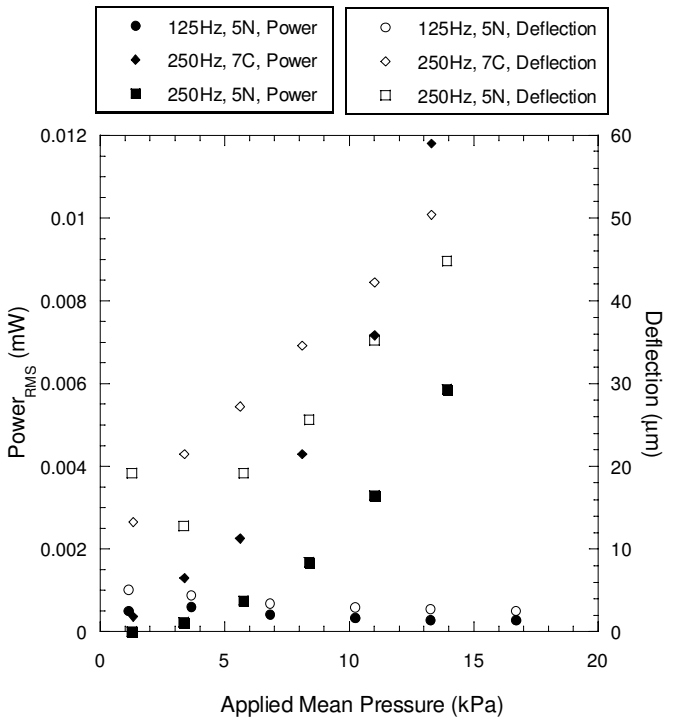

Figure 8.16: Comparison of the output power and deflection amplitude for two 5 mm membranes as the applied mean pressure is increased and the applied pressure amplitude was 10 kPa.

8.2.6 Electrode changes

The effects of the top electrode orientation and coverage on power generation were examined. A study was conducted that investigated the strain field across a 3 mm membrane [17]. This study was adapted to examine the strain field across 4, 5, and 8 mm membranes for the discussion presented here. Figure 8.17 reveals the strain field for the y-axis of a 5 mm membrane. It was found that the strain field along the x-axis provides a symmetric strain field, but for visual clarity only one axis is presented. The strain is at a maximum at approximately 2 mm from the center of the membrane. Therefore, an electrode with a side length of 4 mm centered over a 5 mm membrane just extends to the

high strain region of a deflected membrane. It has been determined that the predicted strains match well with measured strain data for different membrane sizes.

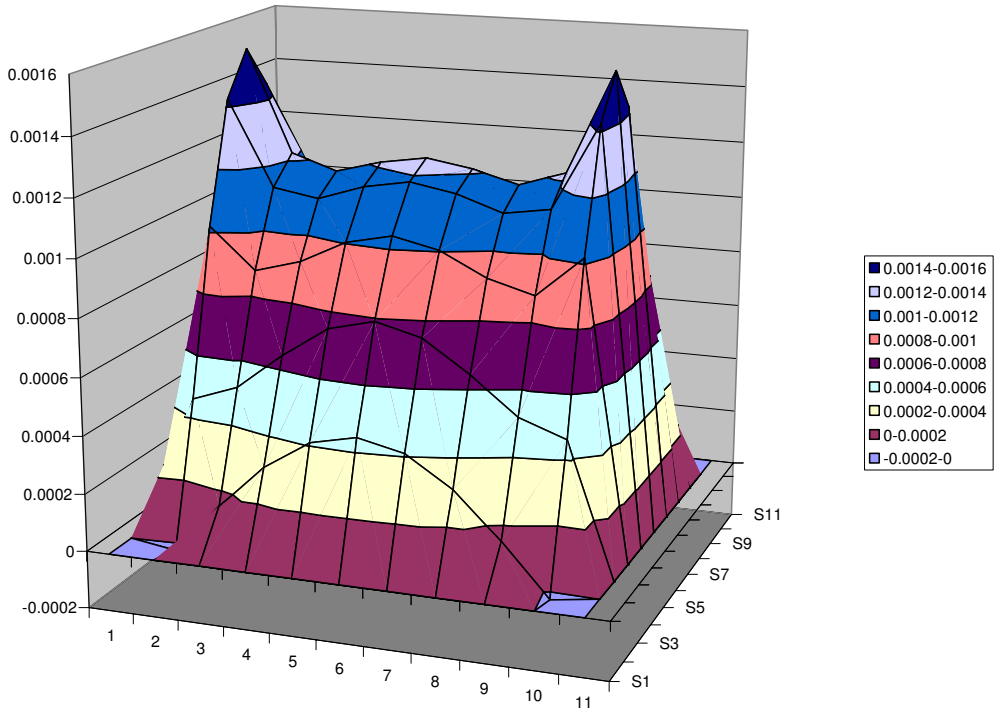

Figure 8.17: Strain field across a 5 mm membrane.

With the electrode coverage of 60% that was described in a study conducted by Demir, the electrode does not cover these high strain regions [16]. Electrode sizes of 6.5, 7, 7.5 mm over an 8 mm membrane were studied and described here, in order to determine if having the electrode cover the high strain region increased the amount of output power. In addition to these electrode sizes, a 7.8 mm electrode that was rotated by 45º was examined.

The 8 mm membranes investigated had a composite structure that consisted of 1.8 µm Si, 0.5 µm SiO_2, 175 nm Pt, 2.7 µm HOAc PZT, and 300 nm Au. Initially, the

membranes were poled with an applied field of 10 V/µm for one minute the day before testing was conducted. Then, with a relatively constant mean pressure of 3.5 kPa, an applied peak-to-peak pressure was increased, while the output rms power and deflection were measured. Figure 8.18 shows the output power vs. applied pressure amplitude results for each membrane, where the legend provides the percent electrode coverage over an 8 mm membrane.

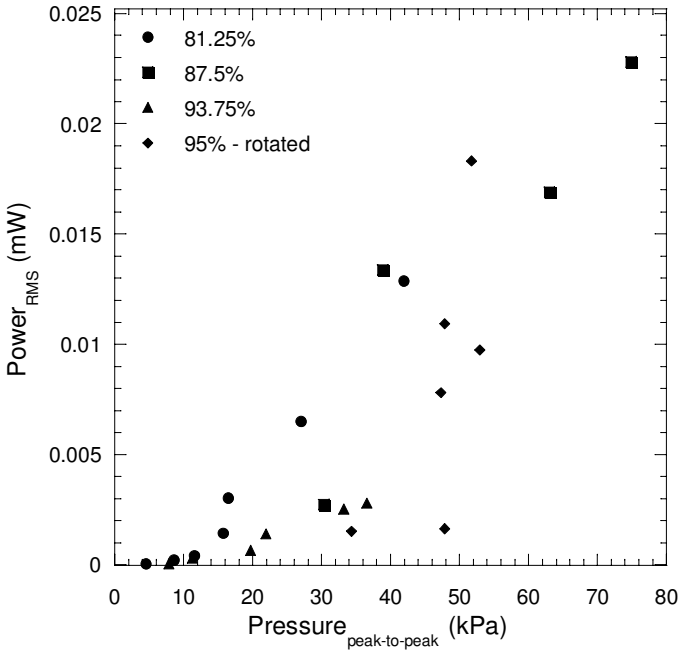

Figure 8.18: Comparison of the output power for different amounts of electrode coverage over an 8 mm membrane.

The capacitances for each percent electrode coverage of 81.25%, 87.5%, 93.75%, and 95% were 70 nF, 146 nF, 172 nF, and 82 nF, respectively. The 3 mm membranes used in Demir's report, which had an electrode coverage of 60%, provided an approximate output rms power of up to 0.015 mW for a 2.5 µm piezoelectric film and applied pressure

amplitudes of up to 50 kPa. Figure 8.18 reveals that even with an electrode that covers up to 95% of the membrane area, there is not a large improvement in the amount of output power measured for a given applied pressure. The rotation of the electrode did not provide an increased amount of output power either.

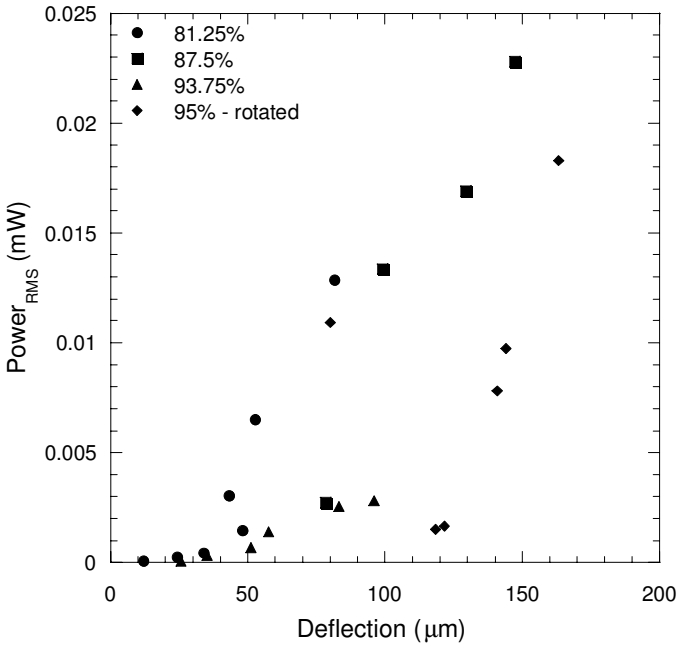

Figure 8.19: Comparison of the output rms power with respect to the center deflection for each of the different amounts of electrode coverage over 8 mm membranes.

Figure 8.19 shows the amount of output rms power with respect to the center deflection for each of the different amounts of electrode coverage over the same 8 mm membranes. As the deflection was increased, the amount of output rms power was approximately the same between each of the types of membrane. Therefore, it is evident that a membrane with an electrode coverage of 81.25% provides a similar amount of micropower compared with a membrane that has 95% electrode coverage.

8.2.7 Predicting Output Power

One of the goals of this research was to design a method of predicting how much output power the piezoelectric membrane could produce under the operating conditions similar to the micro engine operating conditions. Theory was used to define an expression for predicting output power from piezoelectric membranes. Experiments were conducted and are presented in comparison to the theoretical predictions.

8.2.7.1 Theory

During dynamic operation, the membrane is actuated with a sinusoidal signal and subsequently it is assumed that the charge produced by the membrane is sinusoidal. With this assumption, the charge produced by the piezoelectric material, Q_{piezo}, is defined by [18],

$$Q_{piezo} = \mathrm{Re}\{\frac{Q_{pp}}{2} e^{jwt}\} \tag{12}$$

where w is the frequency of operation, t is the time, and Q_{pp} is the peak-to-peak charge that is defined as

$$Q_{pp} = \frac{2Ae_{31}}{3a^2}(\delta_{\max}^2 - \delta_{\min}^2) \tag{13}$$

in which e_{31} is the transverse piezoelectric coefficient, Q is the charge, a is half of the membrane side length, δ_{max} and δ_{min} are the maximum and minimum values of the peak-to-peak deflection, and A is the area of the electrode. The total amount of charge measured by the oscilloscope during dynamic operation is Q_C because the output voltage from the membrane is measured across a resistor placed in parallel with the membrane. Some of the charge goes to the load resistor, Q_R, which is observed in the experiment

when the peak-to-peak voltage drops slightly when the resistor is connected. Thus, the total amount of charge produced by the membrane is given by,

$$Q_C = Q_{piezo} - Q_R \tag{14}$$

In order to predict the output power from the membrane, it is useful to examine an equivalent circuit for this type of experiment. Figure 8.20 shows a current source that is connected in parallel to a capacitor, which is the capacitance of the membrane, and a resistor, which is the load used to measure the output voltage.

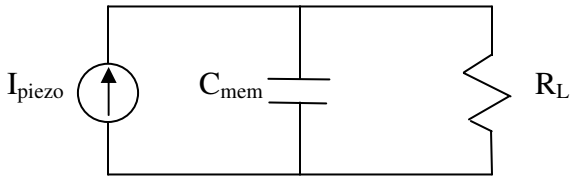

Figure 8.20: Circuit diagram for predicting the output power from the membrane.

The current through the piezoelectric material, I_{piezo}, is given by

$$I_{piezo} = \frac{dQ_{piezo}}{dt} = \mathrm{Re}\{\frac{jwQ_{pp}}{2} e^{jwt}\} \tag{15}$$

For simplicity, (15) can be written in phasor form,

$$\tilde{I}_{piezo} = \frac{jwQ_{pp}}{2} \tag{16}$$

Utilizing the equivalent circuit, the current through the resistor is found with

$$I_{R_L} = \mathrm{Re}\{\frac{1}{1 + jwR_L C} \tilde{I}_{piezo}\} \tag{17}$$

Since the output voltage from the membrane is almost sinusoidal, it is most appropriate to use the cycle rms output voltage when recording oscilloscope values, in which case the

oscilloscope determines the rms output voltage from one cycle of membrane operation. The corresponding predicted rms power is determined by taking the magnitude of the current across the load resistor and then multiplying by $R_L/2$, as shown in (18).

$$Power_{rms} = \frac{\left|\tilde{I}_{R_L}\right|^2}{2} R_L \tag{18}$$

The result of taking the magnitude and inserting Q_{pp} is

$$Power_{rms} = \frac{w^2 R_L}{8} \frac{4A^2 e_{31}^2}{9a^4} (\delta_{\max}^2 - \delta_{\min}^2)^2 (\frac{1}{1 + w^2 R_L^2 C^2}) \tag{19}$$

Experiments provide that the load, R_L, is related to both the frequency of the system, f_r, and the capacitance of the membrane in [19]

$$R = \frac{1}{2\pi f_r C} \tag{20}$$

The maximum power produced by the membrane is determined by measuring the voltage across a load that is impedance matched to the system. For example, a membrane with a capacitance of 29 nF has a system resonant frequency of 250 Hz and the resistance used to obtain the maximum voltage output is 20 kΩ. However, (20) holds for cases in which testing is necessary at frequencies that are much different than resonance. At a system frequency of 150 Hz, the maximum voltage in this example was obtained with a load of 35.4 kΩ. Since (20) holds for each frequency, it can be inserted into (19), which provides the relationship between the output rms power from a piezoelectric membrane and the deflection of the membrane,

$$Power_{rms} = \frac{2\pi f_r e_{31}^2 A t_{PZT}}{36\varepsilon_r a^4} (\delta_{\max}^2 - \delta_{\min}^2)^2 \tag{21}$$

Equation 21 was used to predict the amount of output rms power provided by 4, 5, and 8 mm membranes. Table 8.5 provides the values used for each of the parameters in (21) for each membrane. Each of the parameters listed are measured values for the membranes. Also included in Table 8.5 is the result of inserting each of the parameters into (21) for convenience. Each of the parameters in (21) were changed by 20% individually to see how the prediction changes. For example, it was determined that increasing e_{31} by 20% increased the 'constant' in table 8.5 to $6.72*10^{12}$, in the case of the 4 mm membrane. The largest change in the prediction came from changing a by 20%, in which case the constant is $2.25*10^{12}$.

Table 8.5: Summary of properties used in calculated predictions.

	4mm	**5mm**	**8mm**
$f_{r,system}$ (Hz)	250	200	150
e_{31} (C/m^2)	5.6	3.9	3.9
A (μm^2)	10	17	56
a (m)	.002	.0025	.004
C (nF)	29	40	150
$Power_{RMS}$ = constant * δ^4			
constant	$4.67*10^{12}$	$1.55*10^{12}$	$5.15*10^{11}$

8.2.7.2 Experiment

The next step was to compare experiment results for output rms power provided by these membranes to the predictions. Initially, the applied peak-to-peak pressure was only kept constant in the 4 mm membrane case and the mean pressure was allowed to change, in order to produce the maximum amount of power from each membrane. The results for the 4 mm and 8 mm membranes matched fairly well to the prediction, as shown in figure 8.21. However, the 5 mm data was all shifted to the left of the prediction

curve, as shown by the darkened isosceles triangles in figure 8.21. Another 4 mm membrane was tested to check reproducibility and the results were very similar. The 8 mm membrane with a rotated electrode was also tested and it was found that the output power was approximately the same as that produced by the other 8 mm membrane. The 5 mm membrane was tested again with the mean pressure kept to within 1.4 kPa to 3.5 kPa. The result is indicated in figure 8.21 with the hollow isosceles triangles. A third experiment was conducted with the 5 mm membrane, in which the mean pressure was held at approximately 7 kPa. The result is provided in figure 8.21 with the hollow right triangles.

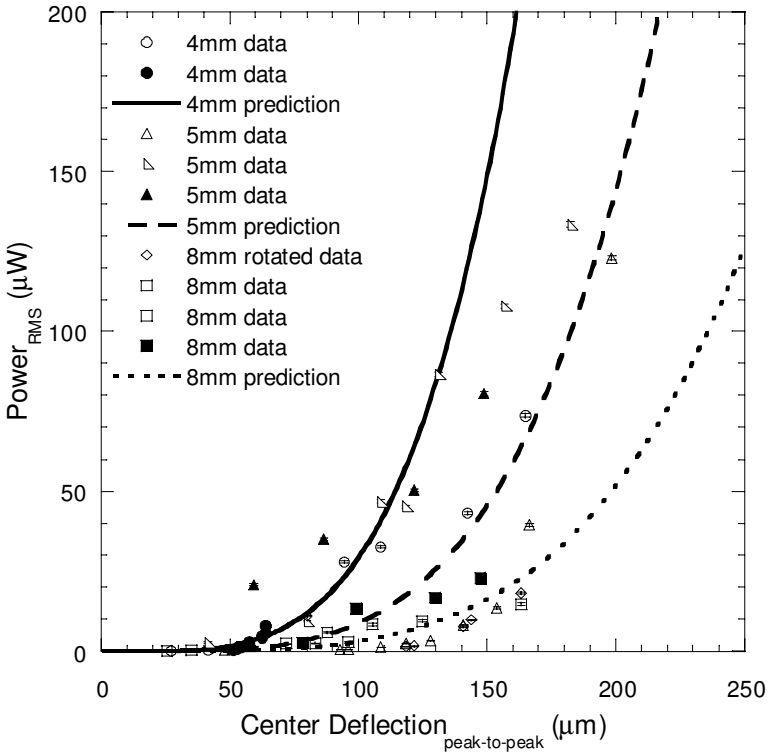

Figure 8.21: Comparison of output rms power with respect to the peak-to-peak center deflection of several 4, 5, and 8 mm membranes.

It seems as though the collection of data for the 5 mm membrane tends to follow the predicted curve, but the reproducibility of the data is not exact because each test had a slightly different mean pressure. According to figure 8.16, doubling the mean pressure increases the rms power by approximately three times when the membrane is oscillating at 250 Hz and in such a way that it does not pass through zero deflection. Therefore, the variation in the results shown in figure 8.21 from the predicted trend is most likely due to the variation in the mean pressure during testing. Thus, the predictions provided by the theory derived in this section align fairly well with experiment data for three different membrane cases.

8.3 Conclusions

The dynamic testing apparatus was utilized to investigate several aspects of piezoelectric membranes during dynamic operation. The material property aspect that improved the overall performance of the membrane was the type of PZT chemistry used. A HOAc-based PZT film provides improved dynamic performance, higher piezoelectric properties, and a higher FOM than the 2MOE-based PZT films. The geometric changes of electrode orientation and percent coverage did not dramatically impact the power output. The investigation of operating conditions determined that the applied poling field of 15 V/μm should be utilized for PZT films for thicknesses of approximately 3 μm to ensure full poling. The mean pressure can stiffen the operating system during dynamic operation. However, if the membrane is oscillating about zero deflection, the mean pressure effect will be apparent. If the membrane does not pass through zero deflection during oscillation, then the stiffening effect will be minimal. Therefore, in order to

increase the amount of micropower produced by the piezoelectric membranes, the membrane should oscillate so that the membrane does not pass through zero deflection. An analytical expression was derived for predicting the amount of output rms power with respect to the deflection of piezoelectric membranes. Experiments were conducted for several membranes and compared to the predictions. The results reveal that the predictions provide a reasonable estimate for the output power from oscillating piezoelectric membranes.

References

[1] M. Dubois, P. Muralt, D.V. Taylor, S. Hiboux, "*Which PZT thin films for piezoelectric microactuator applications?*" Integrated Ferroelectrics **22** (1998) p. 535-543.

[2] H.G. Yu, L. Zou, K. Deng, R. Wolf, S. Tadigadapa, S. Trolier-McKinstry, "*Lead zirconate titanate MEMS accelerometer using interdigitated electrodes*," Sensors and Actuators A **107** (2003) p. 26-35.

[3] P. Ochoa, J.L. Pons, M. Villegas, J.F. Fernandez, "*Effect of bonding layer on the electromechanical response of the cymbal metal-ceramic piezocomposite*," Journal of the European Ceramic Society **27** (2007) p. 1143-1149.

[4] L.W. Weiss, J.H. Cho, K.E. McNeil, C.D. Richards, D.F. Bahr, R.F. Richards, "*Characterization of an External Combustion Dynamic Micro Heat Engine*," Journal of Micromechanics and Microengineering **16** (2006) S262–S269.

[5] A. Safari, B. Jadidian, E.K. Akdogan, "*Piezoelectric composites for transducer applications*," Comprehensive Composite Materials **5** (ISBN: 0-080437230) p. 533-561.

[6] S. Whalen, M. Thompson, D. Bahr, C. Richards, R. Richards, "*Design, fabrication and testing of the P3 micro heat engine*," Sensors and Actuators A **104** (2003) p. 290-298.

[7] J.V. Martinez, "*Fabrication, Materials, and Characterization for Efficient MEMS Power Generation*," Masters Thesis, Washington State University (2004).

[8] S. B. Lang, Source Book of Pyroelectricity: Pyroelectric Coefficient Measurements with the Direct Method, Gordon and Breach Science Publishers, London (1974).

[9] K. Bhattacharya, G. Ravichandran, "*Ferroelectric perovskites for electromechanical actuation*," Acta Materialia **51** (2003) p. 5941–5960.

[10] K-ho. Lam, X. Wang, H. L-wa. Chan, "*Piezoelectric and pyroelectric properties of (Bi0.5Na0.5)0.94Ba0.06TiO3/P(VDF-TrFE) 0–3 composites*," Composites A **36** (2005) p. 1595–1599.

[11] T. Yoshimura, S. Trolier-McKinstry, "*Transverse piezoelectric properties of epitaxial $Pb(Yb_{1/2}Nb_{1/2})O_3$-$PbTiO_3$ (50/50) films*," Journal of Crystal Growth **229** (2001) p. 445-449.

[12] J.C. Raupp, "*Performance characterization of a MEMS based piezoelectric microgenerator*," Masters Thesis, Washington State University (2005).

[13] S.-B. Kim, D.-Y. Kim, J.-J. Kim, S.-H. Cho, "*Effect of grain size and poling on the fracture mode of lead zirconate titanate ceramics*," J. Am. Ceram. Soc. **73** (1990) p. 161.

[14] A.K. Jonscher, Dielectric Relaxation in Solids: Time-dependent dielectric response due to an "inertia" effect of polarization processes, Chelsea Dielectrics, London (1983).

[15] P. Muralt, "*Piezoelectric Thin Films for MEMS*," Integrated Ferroelectrics **17** (1997) p. 297-307.

[16] I. Demir, A.L. Olson, J.L. Skinner, C.D. Richards, R.F. Richards, D.F. Bahr, "*High strain behavior of composite thin film piezoelectric membranes*," Microelectronic Engineering **75** (2004) p. 12-23.

[17] A.L. Olson, "*Processing and properties of a piezoelectric membrane generator*," Masters Thesis, Washington State University (2003).

[18] W.H. Hayt, Engineering Electromagnetics, McGraw-Hill Publishing, New York (1989).

[19] J.H. Cho, "*Electro-mechanical characterization of piezoelectric for MEMS power*," Masters Thesis, Washington State University (2004).

CHAPTER NINE

CONCLUSIONS

The geometry and materials of a piezoelectric membrane have been investigated in order to characterize how to increase the power generation capabilities for MEMS devices. It was found that the initial membrane geometry changes increased the deflection at a pressure of 25 kPa by 18%; a 33% increase in strain. This increase in strain directly increases the amount of output power produced by the membrane, but the geometric changes only increased the strain to approximately 0.06%. The change from a platinum bottom electrode to a gold bottom electrode material reduced processing by five steps. This material change did not change the overall piezoelectric properties of the membrane, which reveals that either type of membrane will produce an equivalent amount of power.

The limitation for all of the piezoelectric thin film membranes tested in this study is the amount of strain that can be induced before membrane failure. The upper limit of strain for the membranes in this research was found to be approximately 0.2%. Depending on the operating conditions and the membrane structure, deflections of up to 200 μm were measured in this study. With this upper limit to the amount of strain that can be achieved, a previously developed prediction expression was utilized to ascertain the coupling coefficient that can be achieved by different types of piezoelectric membranes. Low deflections, with which the membranes operate in the bending regime, obtained coupling coefficient values between 0.015% and 0.037%. At large imposed

strains the membranes operate in the stretching regime, in which case coupling coefficients of up to 3.2% were measured.

The amount of power produced by these membranes is the key focus of many PZT MEMS device applications. This research has determined that the strain capability of these membranes is the limitation to the amount of power produced during dynamic operation. In order to achieve levels of output power that meet design specifications of a certain application, the membranes can be tailored to have specific piezoelectric properties and geometry. However, the operating conditions used to reach specific levels of deflection and therefore strain are the key influences on the amount of power produced. In order to obtain high levels of output power, the membrane must be operated so that the membrane oscillates in such a way as to not pass through the zero deflection level. Typical levels of output RMS power that were produced by 4 mm high tensile stressed and 5 and 8 mm stress balanced square membranes operating under these conditions reached levels of up to 20 μW with peak-to-peak applied pressures of approximately 10 kPa. The RMS power produced by this type of dynamic operation can be reasonably predicted by an expression that was developed and verified by experiment.

APPENDIX I

IMPEDANCE FITTING MATLAB CODE

```
function [Co,R,L,Cm]=freq_impedance()
% This section reads in the file data
[FILENAME, PATHNAME] = uigetfile('*.*', 'Choose impedance-frequency file');
fid=fopen([PATHNAME, FILENAME]);
while ~strcmp(fscanf(fid,'%s',[1,1]),'POINTS:')
end
N=fscanf(fid,'%d"',[1,1]);
while ~strcmp(fscanf(fid,'%s',[1,1]),'"Frequency"')
end
S=fgetl(fid);
A=zeros(N,2);
for r=(1:N)
   A(r,:)=fscanf(fid,'%f',[1,2]);
   fgetl(fid);
end
% This section defines a variable for each column of data (frequency and impedance)
f=A(:,1);
Zm=A(:,2);


% A plot is generated from which the initial guess at the parameters is made.
plot(f,Zm)
```

```
% The user clicks on a place on the graph to begin fit -- provides program with educated
guess of the resonant frequency.
[X,Y]=getpts;
fr=X(length(X));
Zr=Y(length(Y));
% Here the equivalent circuit parameters are defined to help to make the best fit.
R=5e3;
Co=1/(2*pi*fr)*sqrt(1/Zr^2-1/R^2);
Rs=7.5;
w=2*pi*f;
%L=40;
%Cm=1/(4*pi^2*L*fr^2);
%L=value that gives minimum value between Z and Zm
min_diff=inf;
for R=logspace(2,5,20)
  for L=logspace(1,3,10)
        Cm=1/(4*pi^2*L*fr^2);
              Co=1/(2*pi*fr)*sqrt(1/Zr^2-1/R^2);
        Z=abs(1./(1./(R+i*w*L-i./w./Cm)+i*w*Co)+Rs);
        if sum((Z-Zm).^2)<min_diff;
        min_diff=sum((Z-Zm).^2);
      min_R=R;
      min_L=L;
```

```
        end
  end
end
L=min_L;
Cm=1/(4*pi^2*L*fr^2);
R=min_R;
Co=1/(2*pi*fr)*sqrt(1/Zr^2-1/R^2);
Z=abs(1./(1./(R+i*w*L-i./w./Cm)+i*w*Co)+Rs);

% A plot of fit over data curve is generated.
plot(f,abs(Z),f,Zm)
% An internal function “zeros” is called to improve fit
p=zeros(4,5);
p(:,1)=[Co R L Cm]';
p(:,2)=p(:,1)+.01*[Co 0 0 0]';
p(:,3)=p(:,1)+.01*[0 R 0 0]';
p(:,4)=p(:,1)+.01*[0 0 L 0]';
p(:,5)=p(:,1)+.01*[0 0 0 Cm]';

y=zeros(1,5);
y(1)=fun(p(:,1),Rs,Zm,w);
y(2)=fun(p(:,2));
y(3)=fun(p(:,3));
```

```
y(4)=fun(p(:,4));

y(5)=fun(p(:,5));


[pmin,nfunk]=amoeba(p,y,4,1e-10,'fun');

% These commands provide the output variables.

nfunk

Co=pmin(1)

R=pmin(2)

L=pmin(3)

Cm=pmin(4)

k_squared=Cm/(Co+Cm)

fr=1/(2*pi*sqrt(L*Cm))

Qe=2*pi*fr*L/R


Z=1./(1./(R+i*w*L-i./w./Cm)+i*w*Co)+Rs;

% A final plot is generated to show the best fit over the curve.

plot(f,abs(Z),f,Zm)
```

APPENDIX II

STATIC PRESSURE DEFLECTION SETUP AND INSTRUCTIONS

The discussion that follows provides detailed instructions on how to setup the static bulge testing apparatus. This testing apparatus is used to study mechanical properties of thin films by pressurizing them while the deflection can be simultaneously measured.

Setup

If the samples can be separated, then initially this is accomplished by using a scribe to make a small scratch on the edge of the sample. Once the scratch is made, use a glass cutter clamp to lightly squeeze the sample so that the scratch is aligned with the middle of the glass cutter clamp, which is shown in figure 1. Not much pressure is needed to break the silicon sample. The crack in the silicon should propagate in a straight line out from the scratch if done correctly. Watch out for other membranes or other existing cracking in the line of the scratch that may cause the intended crack propagation to curve. It takes some practice to isolate the membrane to be tested. Make sure that there is room around the membrane to seal the sample to the testing puck with glue.

Figure 1: The glass cutter clamp.

The next step is to glue the sample onto a testing puck. This involves turning on the hot plate by turning the right dial to approximately 3.1, as shown in figures 2 and 3. Wait about 5 minutes for the hot plate to heat to approximately 120 ºC, then put the puck on the hot plate. Figure 4 shows a typical puck that has an access hole, in order to pressurize the membrane.

Figure 2: The hot plate.

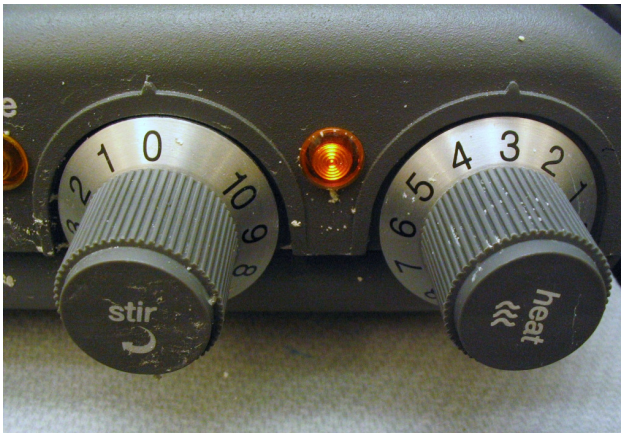

Figure 3: The hot plate temperature knob located at the correct temperature.

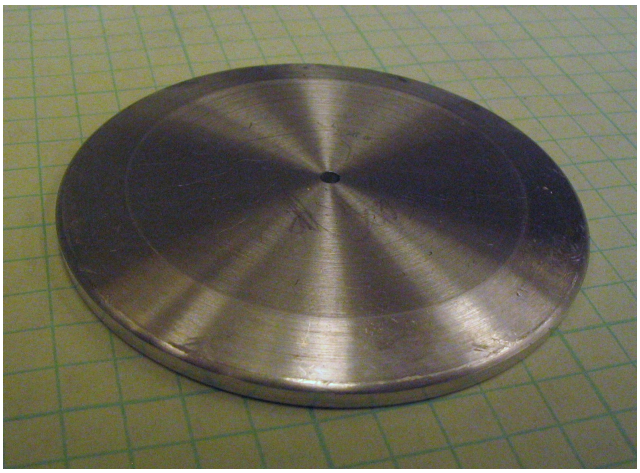

Figure 4: A typical puck that is used for testing a single membrane.

The sample should be glued to the puck with *Crystal bond 555* wax, which has a low melting temperature. When the wax is applied to the puck, make sure to avoid getting wax in the hole in the puck. If wax gets in the hole, then the puck must be cleaned. However, if the wax does not completely surround the hole and seal the sample, the pressure will leak and the test will fail to give accurate results. Figure 5 shows how to apply the wax to the puck. With tweezers grip the sample on the side and tilt it down

slowly onto the melted wax on top of the puck. The membrane in the sample must be centered over the hole in the puck and there must be a layer of wax completely sealing all sides of the sample.

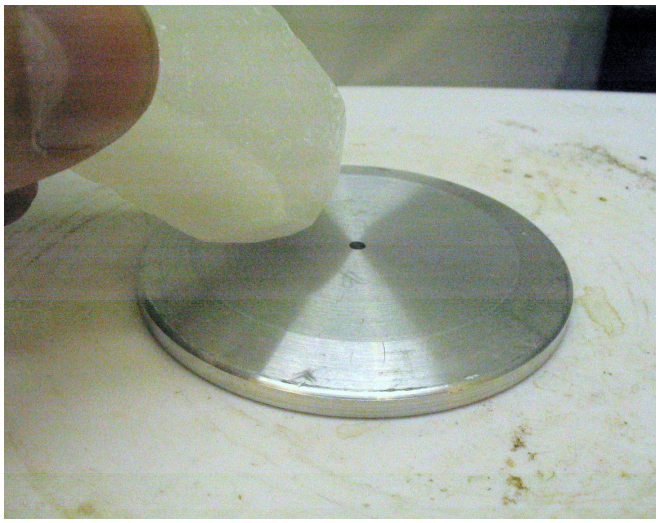

Figure 5: Applying the wax to the puck on the hot plate.

Carefully remove the puck from the hot plate and set it on a surface so that the sample can cool. Immediately use the tweezers to lightly tap all the corners of the sample from the top to ensure that complete sealing has occurred. When the puck is cool enough to handle, visually inspect it from below, holding it up and looking through the hole from the non-sample side. Do not tilt the puck as the wax may not have fully set up yet. Visually, check to see that the membrane is directly above the hole. If it is not an edge of the membrane may be visible through the hole.

Another option for preparing the sample for testing is to seal it between two plexiglass plates, which does not require gluing. Make sure to evenly tighten the screws so that there is even clamping conditions around the seal of the membrane. Figure 6

shows the assembled plexiglass carrier, which is attached to the bulge tester with a center screw that extends through the entire carrier and into the bulge tester.

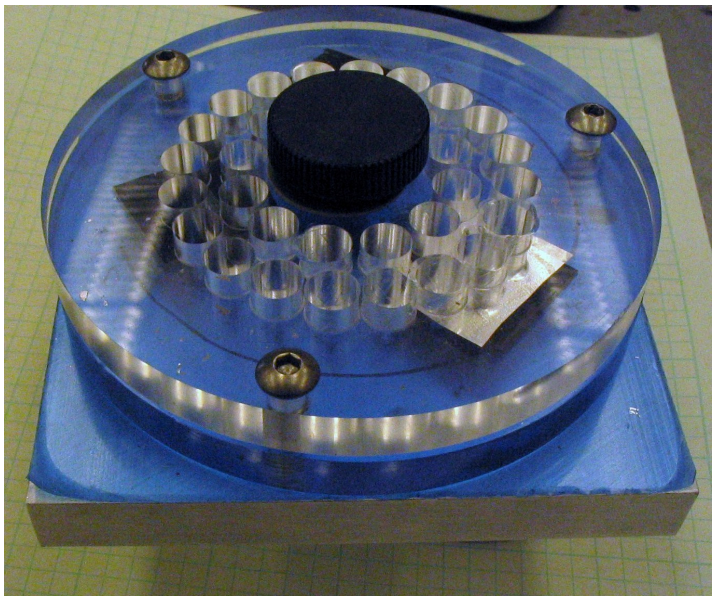

Figure 6: The assembled plexiglass carrier attached to the bulge tester.

The next step in the setup is to turn on the laser vibrometer. Figure 7 shows the main controller of the laser vibrometer. In order to turn the machine on, turn the key to the on position. Make sure that the 'trig in' and 'output' terminals have the correct wires connected to them.

Figure 7: The main controller of the laser vibrometer.

Set the laser vibrometer to displacement, make sure that the conversion range is set to 16 µm/V, and set the tracking filter to 'fast'. Check to see that the cables are connected to the computer adapter, which is shown in figure 8, and that the computer adapter is connected to the computer. Next, on the table by the apparatus, there is a Polytec Fiber Interferometer box, which is shown in figure 9. Hit the laser button to 'standby' or 'on'. Let the system to warm up for approximately 15 minutes.

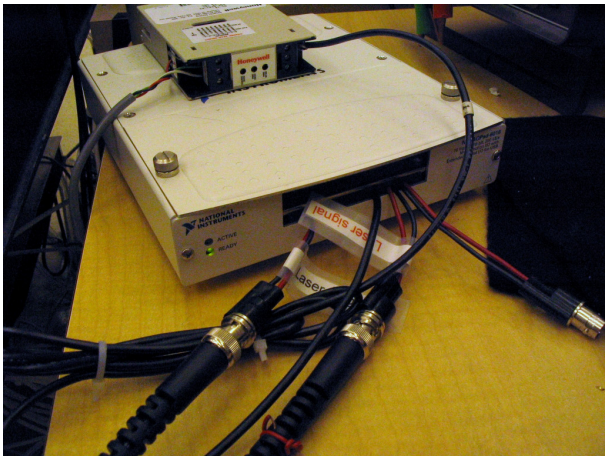

Figure 8: The computer adapter for the laser vibrometer.

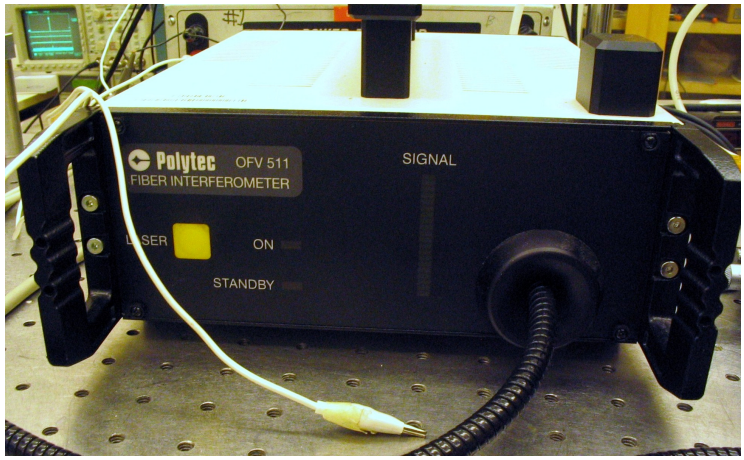

Figure 9: The Polytec Fiber Interferometer.

Next, a bellows that will apply pressure to the membrane should be setup, which is shown in figure 10. Turn the black screw on top of the bellows to the open position. The bellows will apply pressure only when this screw is in the closed position, which is when it is turned all the way clockwise.

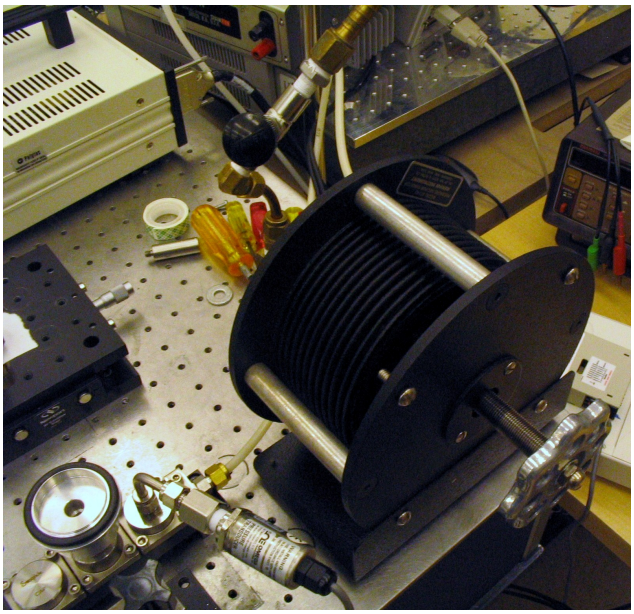

Figure 10: The bellows.

In order to operate the bellows during an experiment, initially close the black screw on top so that it is turned all the way clockwise to the closed position. Then, turn the silver lead screw handle clockwise to apply pressure to the membrane or turn it counterclockwise to pull a vacuum on the membrane.

At this point the laser vibrometer should be aligned to the membrane. Place the puck with the sample on the stand, and clamp it there with the circular clamp, such as the clamp shown in figure 11. Although it is not necessary to completely tighten the circular clamp, a strong seal must be achieved.

Figure 11: A circular clamp.

Adjust the laser that is mounted on a stand to align it with the top of the membrane. Once a maximum reflected signal is achieved, the laser should be incident on the center of the membrane. The laser should be about 4-5 inches above the puck. By carefully turning the laser tip, the focal length of the laser will change so that the focal length equals the

distance between the laser and the membrane. This occurs when the spot size of the laser is the smallest.

To turn off the apparatus, turn the laser to standby and turn the key to the off position on the laser controller. Remove the sample by heating it on the hotplate and then use acetone to remove any residue from the wax. Save the data in the computer and store the samples in a secure location. Make sure that the hot plate and computer are turned off before leaving the lab.

Instructions for Use

Software has been created with a *LabView* program on the computer that records the applied pressure and deflection simultaneously. This testing apparatus can be used to measure the deflection without measuring the applied pressure, but the pressure vs. deflection curve that is generated by the program provides the most information about the membrane. The program is user ready and requires only that the bellows be open initially so that the program can collect the ambient pressure, in order to calibrate the measured applied pressure. Then, with the bellows closed, the applied pressure can be adjusted in either the positive or negative directions repeatedly.

APPENDIX III

DYNAMIC PRESSURE DEFLECTION SETUP AND INSRUCTIONS

The discussion that follows provides detailed instructions on how to setup the dynamic bulge testing apparatus. This testing apparatus is used to study mechanical properties of thin films by dynamically oscillating them at a specific frequency while the deflection can be simultaneously measured. The charge produced by piezoelectric films can be measured and forced through a load resistance, in order to measure the output micropower that is produced.

Setup

In a similar manner to that described for separating samples for static bulge testing, initially each of the samples should be separated and poled. Poling involves placing the sample on a flat surface and attaching probes to the bottom and top electrode access points. The security of the probes needs to be such that the probes will not move during poling. A good method frequency used to do this is to have the probes magnetically attached to another surface so that not too much pressure is applied to the sample with the probe. Figure 1 shows a sample with probes that are secured with magnets to a metal bar. With the probes in place, measure the capacitance of the sample. This also ensures that there is a good electrical contact between the probes and the sample. A voltage should then be applied to the sample with a voltage supply, while a multimeter simultaneously measures the voltage that is being applied. This is a double

check for the voltage supply output, in order to ensure that the correct voltage is being applied to the sample.

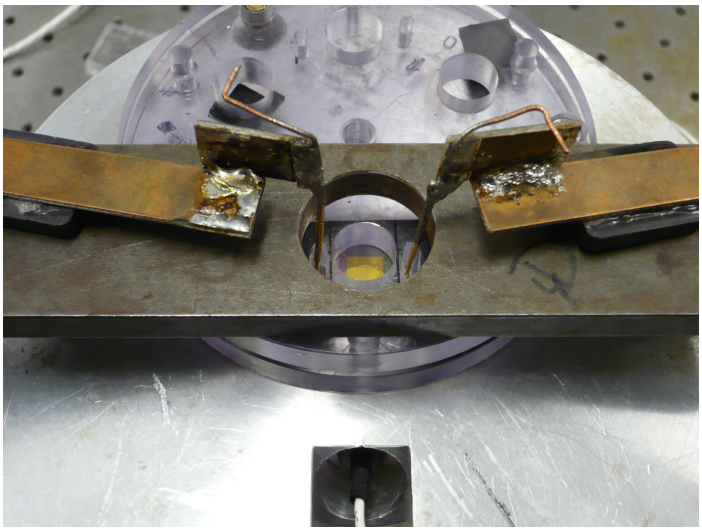

Figure 1: Image of membrane loaded into the plexiglass carrier with probes placed onto electrical access points on sample. Probes are held to metal clamping bar with magnets.

The voltage should be increased consistently and slowly with a suggested ramp rate of approximately 1 V for every 20 seconds. Each sample will be different in that a micron thick film will need a slower ramp rate than a three micron film. The typical peak voltage is 12 V/μm for the piezoelectric films poled in this research. Once the peak voltage is reached, hold for 10 minutes. Then the voltage can be decreased with the same rate that was used for increasing the voltage. Let the sample sit in a safe place for one day prior to testing.

The next step is to load the sample into the plexiglass carrier. This involves having deionized water in a syringe and having the plexiglass plates that make the carrier pre-made. There are two plexiglass plates needed for the carrier. One will have small

holes drilled in it that align to larger holes in the other plate. A small hole behind the membrane will allow DI water to pressurize the membrane from the cavity side of the membrane. The larger hole in the other plate will allow the membrane to bulge without clipping the corners of the membrane. In order to seal the DI water in the cavity behind the membrane, a piece of gasket material should be cut so that there is a hole the shape of the membrane, but slightly larger that the membrane to create a good seal between the sample material that surrounds the membrane and the gasket material. The cut out in the gasket material should have clean edges so that bubbles do not get trapped in the corners or crevasses in the gasket material during clamping. Figure 2 shows a couple example prepared gasket pieces beside the corresponding membranes.

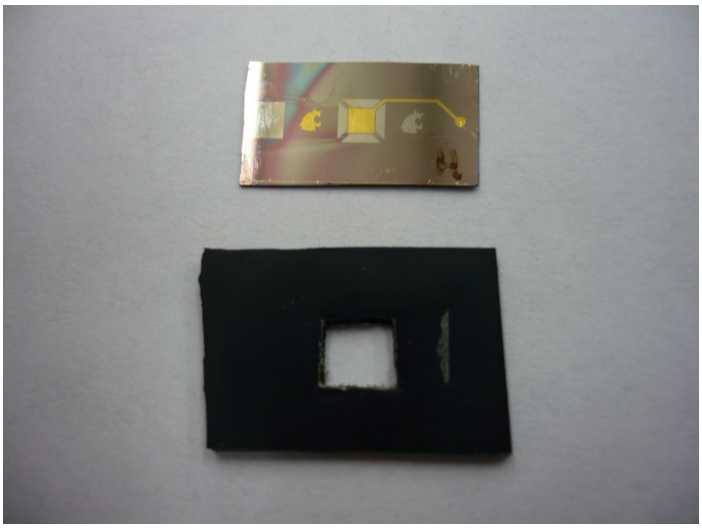

Figure 2: A 3 mm membrane in comparison with a piece of gasket with a cut out that is slightly bigger than the membrane.

In order to assemble the carrier, the plate with the small holes should be placed on a surface that has air below it instead of on a flat table top. The gasket piece should be

centered over the small hole. A bit of vacuum grease can be used to seal the gasket to the plexiglass. Then the cavity in the gasket material should be filled with DI water. If the plate was sitting directly on a flat surface, the DI water would wick through the hole onto the table. Once there is a large droplet of DI water secured in the cavity of the gasket material, the membrane should gently be placed over the droplet and pressed onto the gasket material. Excess DI water will come out around the edges of the membrane, which should be carefully dried off with a tissue. The membrane should stay in place without the extra DI water underneath while the top plate is placed on top. Make sure that there are extra pieces of gasket material located around the bottom plate for even clamping across the carrier. With the top plate in place, press on the center of the entire carrier and examine the back side of the carrier for air bubbles that may be in the cavity underneath the membrane. If there are bubbles, the membrane must be removed and a new droplet of DI applied to the gasket. If there are no bubbles, then the top plate can be attached to the bottom plate with screws. Make sure when tightening the screws to use even clamping to ensure even clamping pressure applied to the sample.

The dynamic bulge tester apparatus must be setup as well. If the apparatus has been sitting for longer than a week, the DI water within the tester has probably evaporated. The entire bulge tester must be disassembled and the cavity beneath the top plate refilled, ensuring that there are no bubbles on the edges of the cavity before sealing it up again. Once the bulge tester is reassembled, DI water should be squirted into the hole in the top of the bulge tester with the syringe so that a large droplet of DI water forms over the hole, as shown in Figure 3.

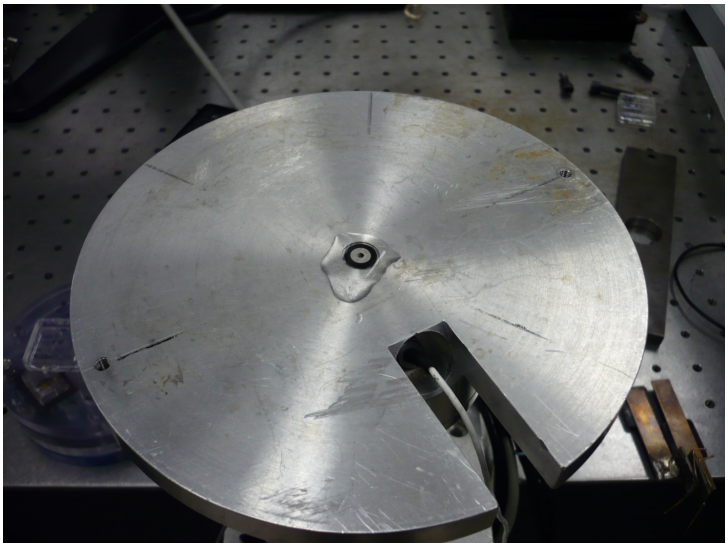

Figure 3: Top of dynamic bulge test apparatus with large DI water droplet.

The carrier can then be placed onto the bulge tester with the small hole in the carrier located just over the hole in the top of the bulge tester. A metal bar should then be placed on top of the carrier and clamped down with two screws on either side of the bar. This will clamp the carrier to the apparatus during testing. When tightening the screws, make sure to also monitor the mean pressure on the oscilloscope so that it stays approximately around 0 mV. This is accomplished by turning the micrometer that is located at the very bottom of the bulge testing apparatus. Figure 4 shows the bulge tester and the location of the micrometer.

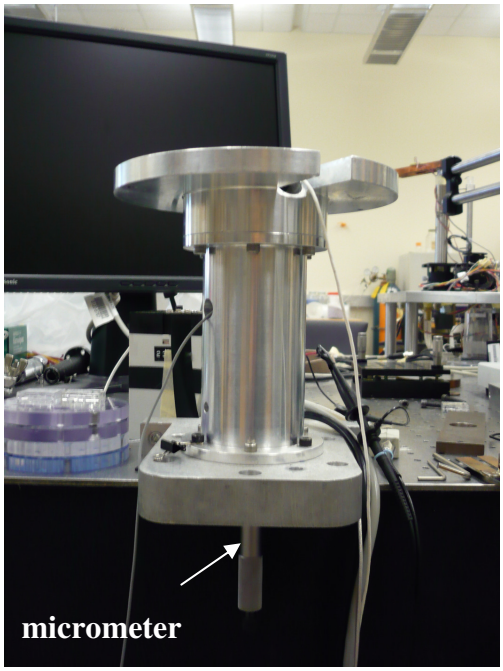

Figure 4: Dynamic bulge test apparatus without the carrier mounted on the top.

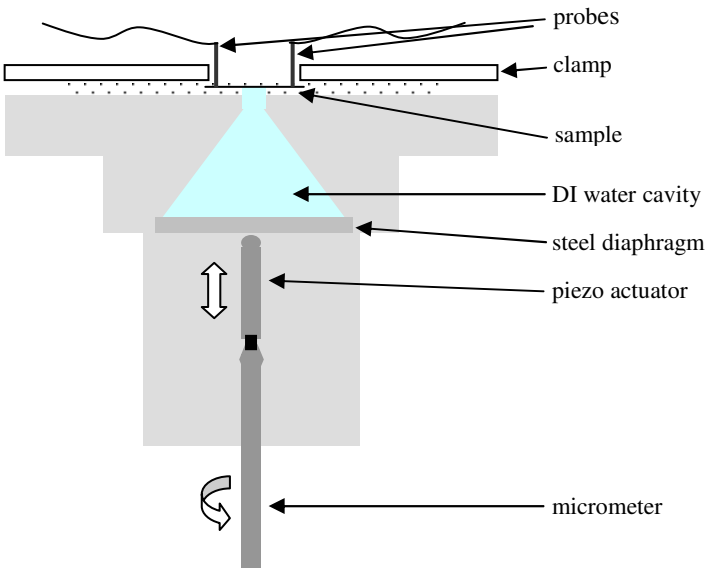

Figure 5: Schematic of the dynamic bulge tester in cross section.

Figure 5 shows a cross section of the interior of the bulge test setup. The interior of the instrument contains a piezoelectric actuator that pushes on a stainless steel diaphragm.

The diaphragm in turn pushes on a column of DI water that forces the membrane to move. The oscillation of the piezoelectric actuator causes the membrane to oscillate. It is important to note that the frequency utilized during the membrane's dynamic operation is the system frequency. Therefore, the resonant frequency found for each experiment is actually the system frequency, which includes the membrane and the entire setup, not the resonant frequency found by any other method for the independent membrane.

The wires that collect the data should be hooked up as shown in Figure 6. The signal generator provides an oscillating voltage to the piezoelectric amplifier, which controls the piezoelectric actuator within the bulge tester. A laser vibrometer is utilized to measure the deflection of the membrane. The charge generated by the membrane as it oscillates is measured directly by an oscilloscope. If this charge is measured across a load resistor, then the output power can be determined.

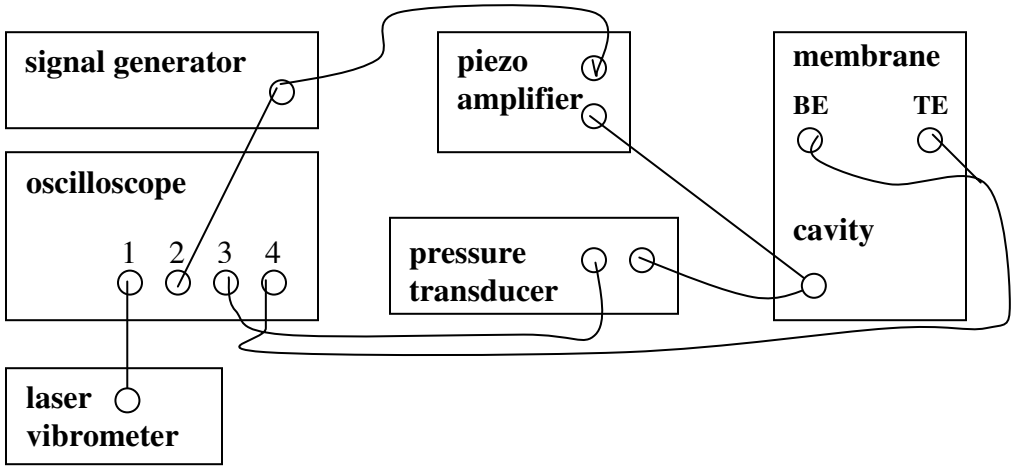

Figure 6: Schematic of wire connections.

The laser vibrometer must be setup by first turning the equipment on and letting it warm up for 15 minutes. Set the laser vibrometer to displacement, make sure that the conversion range is set to 80 μm/V, and set the tracking filter to 'fast'. At this point the laser vibrometer should be aligned to the membrane. This is described in detail in Appendix II. With the laser vibrometer aligned and the carrier mounted onto the apparatus, the equipment is ready for use.

Instructions for Use

Begin with the lowest input voltage and frequency. Turn the piezoelectric amplifier on only after these inputs have been set. The mean pressure will need adjusted with the micrometer under the bulge test instrument. Slowly ramp the frequency. The voltage output from the membrane will oscillate and increase in amplitude. When the amplitude peaks the system resonance has been found. This can be verified by a 90º shift between the pressure and output voltage signals.

A few key aspects to be aware of during testing include the difference between the peak-to-peak pressure and the mean pressure and converting from volts to μm or kPa. The peak-to-peak pressure is the pressure amplitude of the pressure oscillation. The mean pressure is the level of pressure about which the membrane oscillates. The peak-to-peak pressure is changed by the voltage input from the signal generator. The mean pressure is changed by twisting the micrometer that extends from the bottom of the bulge testing instrument. Changing either pressure will cause the system resonance to change slightly because it effectively changes the stiffness of the membrane. Another aspect to know for working with the bulge tester instrument is how to convert units. The setting on

the laser vibrometer indicates the conversion for obtaining the deflection in units of microns. The pressure signal levels are converted from volts to kPa by

$$kPa = \frac{V}{0.098}\left(\frac{6894.7573}{1000}\right). \tag{8}$$

One of the key pieces of information is the amount of output power provided by the oscillating membrane. Other characteristics include the mechanical and electrical work, from which the efficiency of the energy conversion by the membrane to produce the output power can also be determined. These behavioral characteristics are important to applications that involve membrane oscillation at specific frequencies and are discussed in detail in Chapter 3. The conditions under which the membrane operates can be adjusted to follow specifications. Utilizing the dynamic bulge test system enables the user to demonstrate the membrane's capabilities under oscillating conditions.